HIGH FREQUENCY DISCHARGES AND THEIR APPLICATIONS

Charles University in Prague

Faculty of Mathematics and Physics

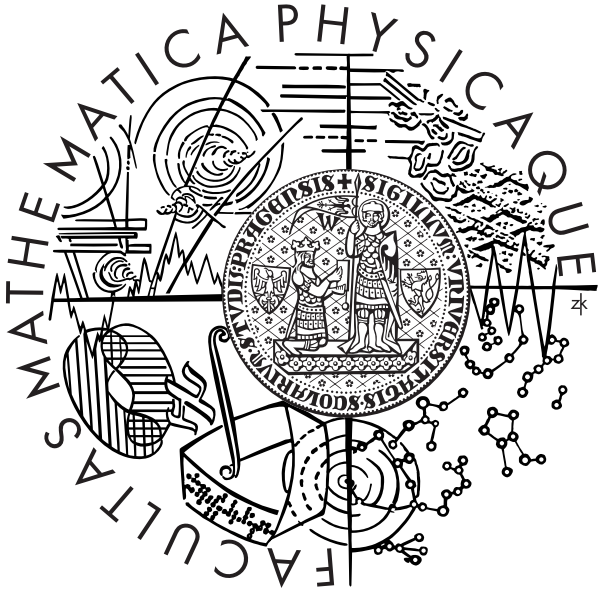

DOCTORAL THESIS

HIGH FREQUENCY DISCHARGES AND THEIR APPLICATIONS

Author: Mariya Chichina

Supervisor: Prof. RNDr. Milan Tichý, DrSc.

Branch: F-2 Physics of Plasma and Ionized Media

Department of Surface and Plasma Science

Prague 2007

Acknowledgments This PhD thesis is a not just my own contribution, but there is a lot of people who have helped me over the years of writing. Without this invaluable support this work would not have been possible. It is worth mentioning that sometimes the help was not directly oriented on the entire project specifics but on the not less important organization and motivation parts giving me a push in the right direction. I am eternally grateful for everyone listed below.

On the first place I must thank my supervisor Milan Tichy for his advice not only in the specifics of plasma physics but in all life sphere. I thank him for his endless support during the evolution my PhD thesis and continuous encouragement during my PhD studies.

Also I wish to thank Olexander Churpita for providing good working facilities and helping in the interpretation of the experimental results.

Next, I would like to extend a big thank-you to Pavel Kudrna for being responsive and subservient resolving problems with PC, general advice, and for being friends.

I also thank Zdenek Hubicka for his important consultations on the subject.

My thanks are going to Stepan Kment, Ales Marek, Alan Maslani, Irena Pickova, Jiri Olejnicek, Petr Virostko, for being helpful colleagues and very good friends.

I am very grateful for cooperation to my colleagues from Department of Macromolecular Physics Andrej Grinevich, Jan Hanus. It was a big pleasure to work at Arndt Moritz University in Greifswald during my PhD studies, and I thank Dr. Hippler and Dr. Benhke for invitation.

I would like to give the most special thanks to my mother Margarita, father Vadim, brother Vitaly for supporting me during the last 26 years. It is through their encouragement and care that I have made it through all the steps to reach

this point in life. My family has always been taking care of me and I love them very much.

I thank my fiance Rudolf Hon for his support. He has been playing a role of careful listener at all my ups-and-downs of the last months and has been very patient to my occupation during all stages of preparation of PhD thesis.

There is also a number of other people who do not work with me directly on the project but have been supportive friends for many years. In particular, I would like to thank Olga Aslanidi, Olena Bilykova, Julia Dimitrienko, Karel Jelinek, Marina Sabaeva (in alphabetic order) who were always next to me and encouraging me.

This work was financially supported by the research plan MSM 1132000002 and MSM 0021620834, financed by the Ministry of Education of the Czech Republic, grants 202/03/0827, 202/03/H162, 202/04/0360, 202/05/2242 and 202/06/0776 of the Czech Science Foundation, DAAD-ASCR project: D-CZ 11/05-06, by GRANT AGENCY of the AS CR, grant S 1010203 and project COST action 527.

I believe that this dissertation has made a real contribution to the field of thin film deposition and atmospheric pressure discharge. I hope that everyone who reads this dissertation will find it useful in his/her future work.

Chichina Mariya, Prague 2007.

Introduction

Interest in the atmospheric plasma systems increases from year to year. These systems do not need expensive vacuum chambers, are not limited by the volume of these chambers, do not use vacuum pumps. The deposition rate in these systems may be higher than that in the vacuum systems [1, 2]. Disadvantages of the atmospheric systems are related with the use of expensive gases, such as usually He, and with some difficulties with ignition of atmospheric pressure discharges. Also, at atmospheric pressure is the analysis of the processes, which occur in the discharge, more complicated than at reduced pressure. In spite of big interest in atmospheric pressure systems, their properties are still not satisfactorily described yet. An example of the atmospheric pressure systems presents the barrier torch discharge.

The present work is dedicated to this discharge, to the processes taking place during burning of this discharge, to its properties and to the thin films that can be created by this discharge. PhD thesis consists of two parts: in the first part the properties of the barrier torch discharge and methods of its diagnostic are described, in the second part the properties of the thin films deposited by this discharge are investigated. In our laboratory ZnO and TiO_2 thin films were deposited and studied.

ZnO is one of the wide band-gap semiconductors for optoelectronic devices, such as a light emitting diode and a laser diode in the ultraviolet (UV) region. In particular, its large exciton binding energy (60 meV) provides a possibility to produce a practical low-threshold excitonic laser diode [3].

ZnO is now gathering great interest for its possible applications in large optoelectronic devices such as flat panel displays (FPD) and solar cells, as a transparent semiconductor and transparent conductive oxide (TCO). The recent remark-

able increase in demand for TCO thin films has stimulated the need to reduce cost of their production. Currently, most TCO thin films in practical use are deposited using d.c. magnetron sputtering; present requirements call for achieving further target cost reductions and higher deposition rates.

TiO_2 (Titania) has been subject of intensive research due to its outstanding physical and chemical characteristics. During last decade, basic and applied research focused on the preparation and characterization of TiO_2 thin films, which feature large energy gap, excellent visible and near-IR transmittance, high refractive index (2.75 at 550 nm) and large dielectric constant ($\epsilon_r \sim 170$).

Titania exists in a number of crystalline forms, the most important of which are Anatase and Rutile.

It was found that TiO_2 is antibacterial, self-cleaning, super-hydrophilic, and able to decompose organic substances. Titanium dioxide has a very high melting point (1840 °C), and is established as an optical coating material [4]; these coatings are widely used in many optical applications and device constructions [5]. Titanium dioxide coatings might be very good candidates for optical temperature sensing applications. Various other applications of TiO_2 thin films are encountered in environment protection and medicine (blood compatible films).

The reported results refer to the studies carried out in the Institute of Physics, Division of Optics, Academy of Sciences of the Czech Republic.

List of symbols

- A - cross section of plasma jet
- AFM - Atomic Force Microscope
- A_{pk} - transition probability
- $APPJ$ - Atmospheric Pressure Plasma Jet
- $\alpha_{1/2}$ - fractional semi-half width
- B - susceptance
- γ_i - adiabatic coefficient
- c - light speed
- CVD - Chemical Vapour Deposition
- c_s - sound speed
- d - length of the plasma column
- DBD - Dielectric Barrier Discharge
- $\Delta\lambda$ - line width
- ΔG_f - free energy
- E - photon energy
- e - charge of electron
- $EEDF$ - Electron Energy Distribution Function ($\mathrm{f}_e(\mathrm{v})$)
- ϵ_{pk} - line emission

- ϵ_r - dielectric constant
- f - factor
- FDP - Flat Panel Display
- FHC - Fused Hollow Cathode
- $FWHM$ - Full Width at Half Maximum
- G - specific conductance
- h - Planck constant
- Θ - solid angle
- i - current density
- I - intensity
- I_m - RF current amplitude
- I_{pi} - ion current
- I_{pe} - electron current
- I_{RF} - RF current
- j - current
- j_{sat}^{ion} - ion saturation current
- j_{sat}^{elec} - electron saturation current
- k_B - Boltzmann constant
- λ - wavelength

- m_i - ion mass
- μ_i - reduced ion mass
- n - order of diffraction
- n_e - electron concentration
- n_i - ion concentration
- OES - Optical Emission Spectroscopy
- $OAUGDP$ - One Atmosphere Uniform Glow Discharge Plasma
- p - power density
- P_λ - line profile
- P_{RF} - RF power
- R - resistance
- $R.I.$ - Refractive Index
- r_p - probe radius
- ρ - thin film resistivity
- t - thin film thickness
- t - time
- TCO - Transparent Conductive Oxide
- T_e - electron temperature
- T_i - ion temperature

- T_n - neutral gas temperature
- T_r - rotational temperature
- T_v - vibrational temperature
- Φ_{sh} - potential drop across the Debye sheath
- Φ_{fl} - floating potential
- Φ_p - probe potential
- Φ_s - plasma (space) potential
- U_{RF} - RF voltage
- U_m - RF voltage amplitude
- ν - collision frequency of electrons with heavy particles
- V_{bias} - voltage applied between two identical electrodes
- v_e - electron velocity
- $VLSI$ - Very Large Scale Integrated
- Y - admittance
- Z - average charge
- Z - impedance
- Z_r - real part of impedance
- Z_{im} - imaginary part of impedance
- ω - frequency

Contents

Chapter 1

Generation of atmospheric pressure dielectric barrier discharge and barrier torch discharge, their properties and applications

1.1 Atmospheric pressure dielectric barrier discharge

1.1.1 Fundamentals of Dielectric-Barrier Discharge

Early investigations

In 1857 Siemens in Germany proposed an electrical discharge for "ozonizing" air [6]. The novel feature of this configuration was that no metallic electrodes were in contact with the discharge plasma. Atmospheric-pressure air or oxygen was passing in the axial direction through a narrow annular space between two coaxially mounted cylindrical glass tubes, Figure 1.1.

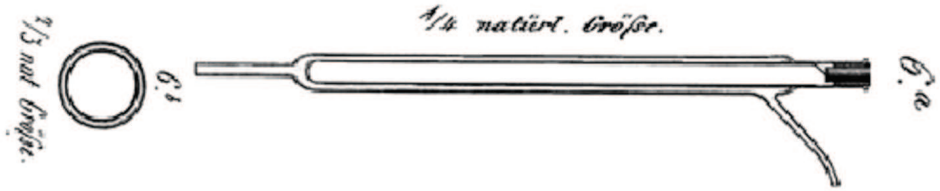

Figure 1.1: Siemens' historical ozone discharge tube of 1857 (Natürl. Grösse means real size [7]).

Cylindrical electrodes inside the inner tube and wrapped around the outer tube were used to apply an alternating radial electric field, high enough to cause electrical breakdown of the gas inside the annular discharge gap. Due to the action of the discharge part of the oxygen in the gas flow was converted to ozone. If air was used as a feed gas also traces of nitrogen oxides were produced. The glass walls, acting as dielectric barriers have a strong influence on the discharge properties, which is therefore often referred to as the Dielectric-Barrier Discharge (DBD) or simply Barrier Discharge (BD). Also the term "silent discharge", introduced by Andrews and Tait in 1860, is frequently used in different languages

(stille Entladung, decharge silentieuse).

It was soon realized that the Siemens tube was an ideal plasmachemical reactor in which many gases could be decomposed without using excessive heat [8, 9]. Investigations on the mechanism of "electrodeless" discharges, and especially on the influence of radiation on breakdown, were carried out by Harries and von Engel [10, 11] and by El-Bakkal and Loeb [12]. An important observation about breakdown of atmospheric-pressure air in a narrow gap between two glass plates was made by the electric engineer Buss in 1932 [13]. He observed that breakdown occurred in many short-lived luminous current filaments, rather than homogeneously in the volume. He also obtained photographic Lichtenberg figures showing the footprints of individual current filaments and recorded oscilloscope traces of the applied high voltage pulse. Buss came up with fairly accurate information about the number of filaments per unit area, the typical duration of a filament and transported charge in a filament. Further contributions to the nature of these current filaments were made by Klemenc, Hintenberger and Hofer in 1937) [14], Suzuki and Naito in 1952 [15], Gobrecht, Mainhardt and Hein in 1964 [16] and Bagirov, Nuraliev and Kurbanov in 1972 [17]. Today these current filaments are often referred to as microdischarges (see 1.1.3.). They play an important role as partial discharges in voids of solid insulation under AC stress and in many DBD applications. The accomplishment of recent years was that microdischarge properties were tailored to suit desired applications and that the development of power electronics resulted in efficient, affordable and reliable power supplies for a wide frequency and voltage range. More recent investigations showed that also homogeneous or diffuse DBDs could be obtained under certain well-defined operating conditions. Also regularly patterned DBDs can be obtained in different gases. The phenomenology and discharge physics of these

different types of DBDs were reviewed by Kogelschatz [18]. Siemens referred to the process as electrolysis of the gas phase. Today we call it a non-equilibrium discharge in which chemical changes are brought by reactions of electrons, ions, and free radicals generated in the discharge. The main advantage of the dielectric barrier discharge is that controlled non-equilibrium plasmas can be generated in a simple and efficient way at atmospheric pressure. In addition to its original use for the generation of ozone many additional applications have evolved: pollution control, surface treatment, generation of ultraviolet radiation in excimer lamps and infrared radiation in CO_2 lasers, mercury-free fluorescent lamps and flat plasma display panels (see reviews by Kogelschatz [19, 20, 7] and Wagner [21]).

Electrode Configurations

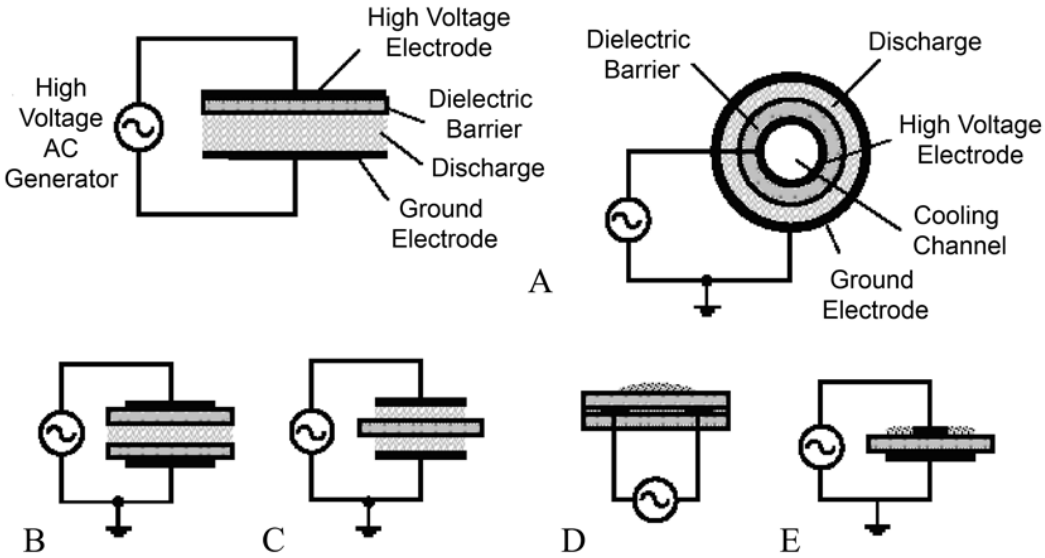

Figure 1.2: Different dielectric-barrier discharge configurations [22].

In addition to the original Siemens ozone discharge tube different electrode

configurations have been proposed, that all have in common, that at least one dielectric barrier (insulator) is used to limit the discharge current between the metal electrode(s). Figure 1.2 shows a number of different dielectric-barrier discharge configurations covering volume discharges (a,b,c) as well as surface discharges (d,e). The presence of the dielectric barrier precludes DC operation because the insulating material cannot pass a DC current. AC or pulsed operation is possible, because any voltage variation dU/dt will result in a displacement current in the dielectric barrier(s).

1.1.2 Barrier Discharge

Based on experience with ozone research it was believed for a long time that DBD always exhibit many discharge filaments or microdischarges. This multifilament discharge with a seemingly random distribution of microdischarges is prevailing in atmospheric-pressure air or oxygen [7, 20, 23, 24]. Work performed in many different gases under various operating conditions revealed that also regularly patterned or diffuse barrier discharges can exist at atmospheric pressure. The formation of regular discharge patterns was observed for example in [25, 26]. The physical mechanism of pattern formation has been investigated in a series of papers of the Purwins group at Münster University [27, 28, 29, 30, 31]. In 1968 Bartnikas reported that AC discharges in helium can also manifest pulseless "glow" and "pseudoglow" regimes, apparently homogeneous diffuse volume discharges, now often referred to as atmospheric pressure glow discharges (APG/APGD)[32]. A few years later this work was extended to discharges in nitrogen and air at atmospheric pressure [33]. Early work on polymer deposition in pulsed homogeneous barrier discharges in an ethylene/helium mixture was reported in [34]. Starting in 1987 the group of Okazaki and Kogoma at Sophia University in Tokyo reported

on intensive investigations in homogeneous dielectric barrier discharges and their applications and proposed the term APG, short for atmospheric pressure glow discharge. The interesting physical processes in these discharges and their large potential for industrial applications have initiated experimental as well as theoretical studies in many additional groups in France [35, 36], in the USA and Canada [37, 38, 39], in Germany [21, 40, 41, 42, 43, 44], in Russia [45, 46, 47, 48], and in the Czech Republic [49, 50], to name only the most important ones. Much of the work on the physics of filamentary, regularly patterned and diffuse barrier discharges was recently reviewed by Kogelschatz [51].

1.1.3 Multifilament Barrier Discharges [7, 52]

The traditional appearance of the barrier discharge used for ozone generation in dry air or oxygen or for surface modification of polymer foils in atmospheric air is characterized by the presence of a large number of current filaments or microdischarges. Figures 1.3 and 1.4 show photographs of microdischarges in atmospheric-pressure dry air (Figure 1.4 is taken through a transparent electrode). During the past decades important additional information was collected on the nature of these filaments. Early image converter recordings of microdischarges in air and oxygen were obtained by Tanaka et al. in [53]. Precise current measurements were performed on individual microdischarges [54, 55, 56]. The transported charge and its dependence on dielectric properties were determined over a wide parameter range [57, 58, 59]. Typically, many microdischarges are observed per square cm of electrode area. Their number density depends on the power dissipated in the discharge. For a moderate power density of 83 mW/cm^2 about 10^6 microdischarges were counted per cm^2 per second [60]. The influence of humidity and that of UV radiation was also investigated [61]. In recent years spectroscopic diagnos-

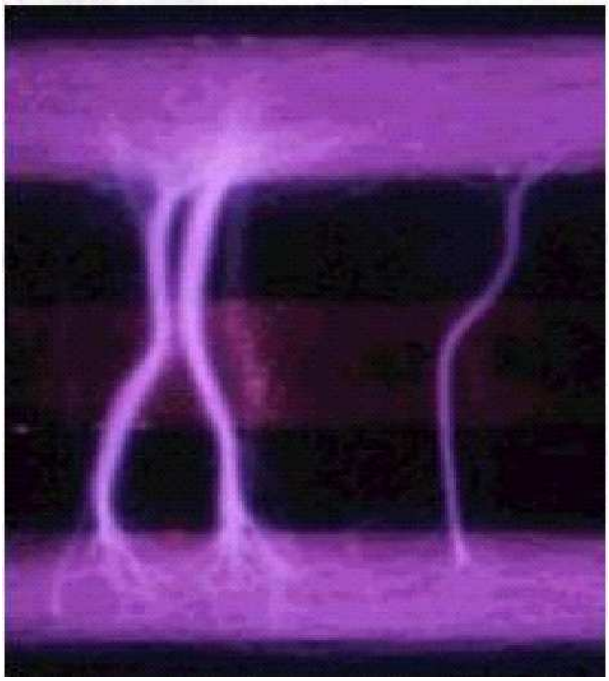

Figure 1.3: Photo of the filaments [63].

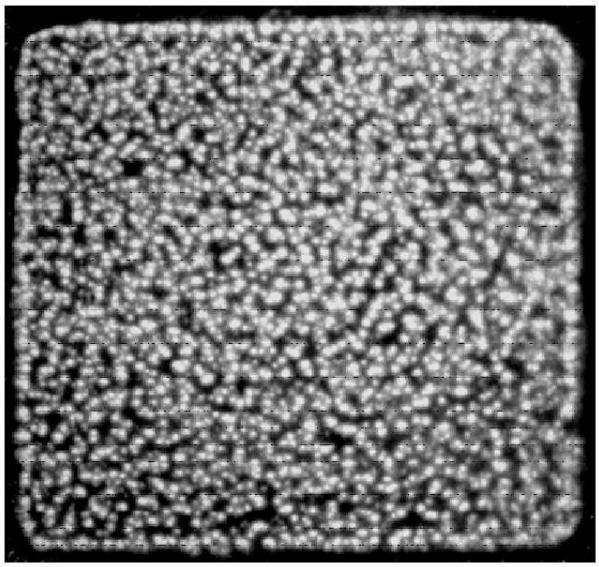

Figure 1.4: End-on view of microdischarges in a 1 mm gap with atmospheric-pressure dry air original size: 6 cm x 6 cm, exposure time: 20 ms [7].

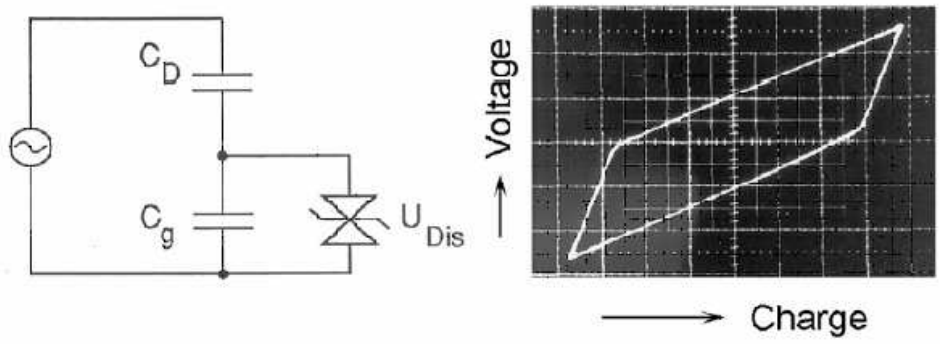

Figure 1.5: Equivalent circuit of a dielectric-barrier discharge and recorded voltagecharge Lissajous figure of an ozone discharge tube [7] .

tics were refined to such a degree that measurements of species concentrations and plasma parameters inside individual microdischarges became feasible [62, 63]. For a given configuration and fixed operating parameters all microdischarges are of similar nature. They are initiated at a well-defined breakdown voltage, and they are terminated after a well-defined current flow or charge transfer. From all these investigations we conclude that each microdischarge consists of a nearly cylindrical filament of high current density and approximately 100 μm radius. At the dielectric surface(s) it spreads into a much wider surface discharge. These are the bright spots shown in Figure 1.4. The duration of a microdischarge is limited to a few ns, because immediately after ignition local charge build up at the dielectric reduces the electric field at that location to such an extent that the current is choked. Each filament can be considered a self-arresting discharge. It is terminated at an early stage of discharge development, long before thermal effects become important and a spark can form. The properties of the dielectric, together with the gas properties, limit the amount of charge or energy that goes into an individual microdischarge. Typical charges transported by individual microdischarges in a 1 mm gap are of the order 100 pC, typical energies are of the order 1 μJ. The plasma filament can be characterized as a transient glow

Lifetime	1-20 ns
Filament Radius	50 - 100 μm
Peak Current	0.1 A
Electron Energy	1 - 10eV
Electron Density	10^{14} - 10^{15} cm^{-3}
Current Density	0.1 - 1 kA cm^{-3}
Total dissipated energy	5 μJ
Gas Temperature	close to average, about 300 K

Table 1.1: Characteristic microdischarge properties in a 1-mm gap in air at atmospheric pressure [64].

discharge with an extremely thin cathode fall region with high electric field and a positive column of quasi-neutral plasma. The degree of ionization in the column is moderately low, typically about 10^{-4}. As a consequence of the minute energy dissipation in a single microdischarge the local transient heating effect of the short current pulse is low, in air typically less than 10 °C in narrow discharge gaps. The average gas temperature in the discharge gap is determined by the accumulated action of many microdischarges, i. e. the dissipated power, and the heat flow to the wall(s) and from there to the cooling circuit. This way the gas temperature can remain low, even close to room temperature, while the electron energy in the microdischarges is a few eV. Major microdischarge properties of a DBD in a 1 mm air gap are summarized in Table 1.1.

In addition to limiting the amount of charge and energy that goes into an individual microdischarge, the dielectric barrier serves another important function in DBDs. It distributes the microdischarges over the entire electrode area.

As a consequence of deposited surface charges the field has collapsed at locations where microdischarges already occurred. As long as the external voltage is rising, additional microdischarges will therefore preferentially ignite in other areas where the field is high. If the peak voltage is high enough, eventually the

complete dielectric surface will be evenly covered with footprints of microdischarges (surface charges). This is the ideal situation which leads to the almost perfect voltage charge parallelogram shown in Figure 1.5. The deposited charges constitute an important memory effect that is an essential feature of all dielectric barrier discharges. As far as applications are concerned each individual microdischarge can be regarded as a miniature non-equilibrium plasma chemical reactor. Recent research activities have focused on tailoring microdischarge characteristics for a given application by making use of special gas properties, by adjusting pressure and temperature, and by optimizing the electrode geometry as well as the properties of the dielectric(s). Such investigations can be carried out in small laboratory experiments equipped with advanced diagnostics. One of the major advantages of DBDs is that, contrary to most other gas discharges, scaling up presents no major problems. Increasing the electrode area or increasing the power density just means that more microdischarges are initiated per unit of time and per unit of electrode area. In principle, individual microdischarge properties are not altered during up-scaling. Efficient and reliable power supplies are available ranging from a few hundred watts in a plasma display panel, close to 100 kW in an apparatus for high speed surface modification of polymer foils to some MW in large ozone generators.

1.1.4 Homogeneous Barrier Discharges

Recently, research on material processing by non-equilibrium atmospheric pressure plasmas witnessed a tremendous growth, both at the experimental and simulation levels. This was motivated by the new technical possibilities in generating relatively large volumes of non-equilibrium plasmas at or near atmospheric pressure, in numerous gases and gas mixtures and at low operating power budgets.

Amongst the modern technologies, the use of DBD has become very prevalent. DBDs use a dielectric material to cover at least one of the electrodes. The electrodes are driven by voltages in the kV range and at frequencies in the audio range (kHz). However, new methods emerged which extended the frequency range down to the DC level. The Resistive Barrier Discharge (RBD) recently developed by Alexeff and Laroussi is such an example [65]. The RBD uses a high resistivity material to cover the surface of at least one of the electrodes. It is capable of generating large volume atmospheric pressure plasma with DC and AC (60 Hz) driving voltages. The limitations of barrier-based discharges have traditionally been their nonhomogeneous nature both in space and time. DBDs for example exhibit a filamentary plasma structure, therefore leading to non-uniform material treatment when used in surface modification applications. This situation led some investigators to search for operating regimes under which diffuse and homogeneous discharges can be produced. In the late 1980s and early 1990's, Okazaki's group published a series of papers where they presented their experimental findings regarding the conditions under which a DBD-based reactor can produce homogenous plasma, at atmospheric pressure [66], [67]. Their work was soon followed by others [35], [68], [69] who validated the fact that non-filamentary plasmas can indeed be produced by DBDs, an outcome not widely accepted by the research community active in this field at that time.

1.1.5 Discharge homogeneity conditions

As mentioned above the idea to use electrodes covered by a dielectric material to generate a stable non-equilibrium plasma at high pressures is actually an old idea dating from the time Siemens used a discharge to generate ozone [6]. However, up until recently the plasma produced by DBDs were filamentary in character, being

made of a large number of streamers or micro-discharges randomly distributed across the dielectric surface [19]. However, Kanazawa [70] showed that under specific conditions, the plasma could be homogeneous. These conditions are:

1. Helium used as a dilution gas.

2. The frequency of the applied voltage must be in the kHz range.

These conclusions were purely empirical, based on more or less experimental trial and error. Similarly, Roth [69] used helium and a low frequency RF source (kHz range) to produce a homogeneous discharge in their device, the One Atmosphere Uniform Glow Discharge Plasma (OAUGDP). The OAUGDP is a DBD-based reactor. They also concluded, based on experimental trials that helium and the frequency range are the critical parameters, which can lead to homogeneous plasma at atmospheric pressure. Roth [71] attempted to explain the frequency range where the homogenous discharge could exist by what he termed as the "ion trapping" mechanism. This idea is based on driving the electrodes by high RF voltages, which induce an electric field that oscillates at a frequency that is high enough to trap the ions but not the electrons in the space between the electrodes. The electrons ultimately reach the electrodes where they recombine or form a space charge. This theory, however, encountered many difficulties, as it is not supported by various modeling results [51]. One of the arguments against it is the fact that in general one cannot trap charged particles by a single axially uniform electric field (the axis normal to the plane of the electrodes in this case), even if it is oscillating. Furthermore, collective effects were not taken into account. For example if the ions were trapped and the electrons drifted towards the electrodes, an ambipolar electric field would be established in a way to repel the electrons away from the electrodes and towards the ions, mechanism not taken into account in the proposed analysis. Massines [36] presented a very different theory, which

seems to be well supported by experimental and modeling works. The main idea behind Massines' theory is that since the plasma generated by a DBD is actually self-pulsed plasma, a breakdown of the gas under low electric field between consecutive pulses is possible due to trapped electrons and metastable atoms. These seed particles allow for a Townsend-type breakdown instead of a streamer-type, leading a to continued discharge conditions even when the electric field is small. A density of seed electrons greater than 10^6 cm^{-3} is sufficient to keep the plasma ignited under low field conditions [68]. The seed electrons are electrons left over from the previous breakdown.

1.1.6 DBD-based discharges at atmospheric pressure

Experimental setup of the Dielectric Barrier Discharge (DBD)

DBD consists basically of two planar electrodes (sometimes co-axial or adjacent cylinders) made of two metallic plates (or tubes) covered by a dielectric material and separated by a variable gap (see Figure 1.6).

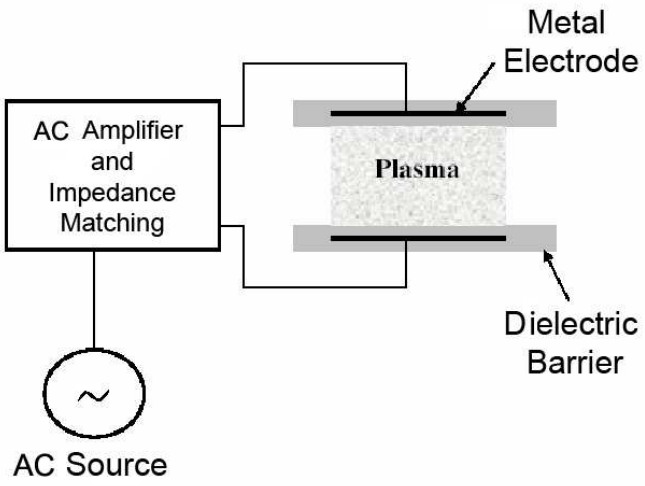

Figure 1.6: Dielectric Barrier Discharge (DBD) configuration with planar electrode.

When operated at atmospheric pressure, the electrodes are energized by a high voltage AC power supply with typical voltages in the 1 to 20 kV range, at frequencies ranging from few hundreds Hz to few kHz. To optimize the amount of power deposited in the plasma, an impedance matching network may be introduced between the AC power supply and the electrodes. The electrode arrangement is generally contained within a vessel or enclosure to allow for the control of the gaseous mixture used. The dielectric material covering the electrodes plays the crucial role in keeping the nonequilibrium nature of the discharge. This is achieved as follows. When a sufficiently high AC voltage is applied between the electrodes, the gas breaks down (i.e. ionization occurs) and an electric current starts flowing in the gas. Immediately, electric charges start accumulating on the surface of the dielectric. These surface charges create an electric potential, which counteracts the externally applied voltage and therefore limits the flow of current. This process inhibits the glow-to-arc transition. Figure 1.7 is a photograph of a diffuse, homogeneous plasma generated by a DBD in an atmosphere of helium with a small admixture of air.

Current-voltage characteristics

Depending on the operating conditions (gas, gap distance, frequency, voltage), the current waveform can exhibit multiple pulses per half cycle or a single wide pulse per half cycle. The presence of multiple current pulses per half cycle is usually taken as an indication that a filamentary discharge is established in the gap between the electrodes.

Figure 1.8 shows the current and voltage waveforms of a filamentary DBD in nitrogen [68]. On the other hand, diffuse and homogeneous discharges exhibit a current waveform with a single pulse per half cycle, as shown in Figure 1.9 [68].

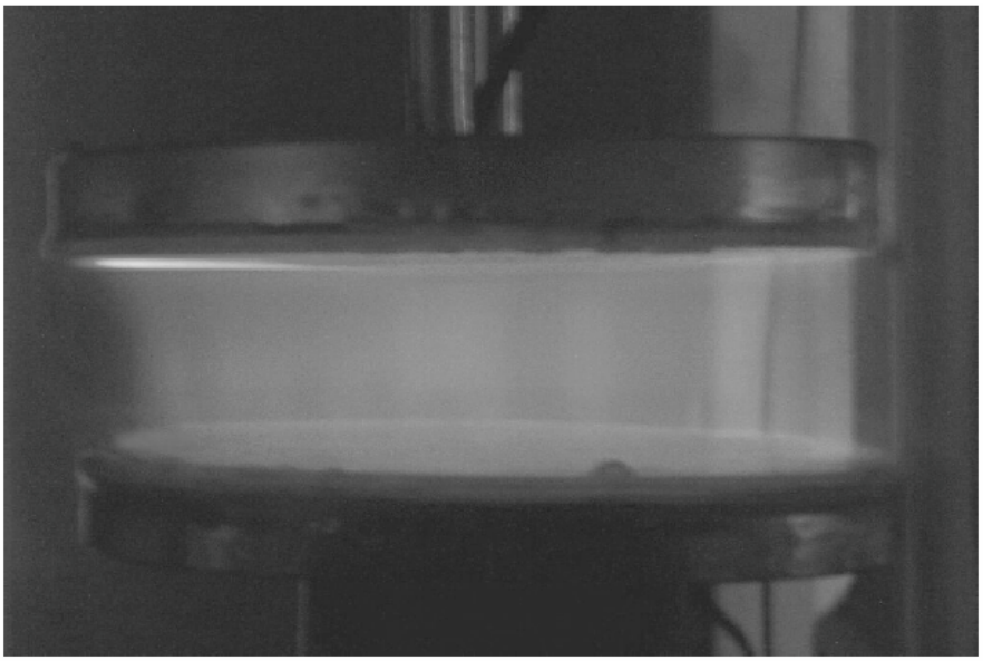

Figure 1.7: Diffuse DBD in a helium/air mixture (helium+1% air, voltage pulse repetition frequency 1kHz, gap distance 2.5 mm)[72].

However, a single pulse is not a sufficient test to indicate the presence of homogeneous plasma. Indeed, if a very large number of streamers are generated in a way that they spatially overlap and if the measuring instrument is not capable of resolving the very narrow current pulses, a wide single pulse can be displayed. Gherardi [68] used fast photography as a second diagnostic method to visually inspect the structure of the discharge channel.

Under conditions leading to homogeneous plasma, photographs taken with exposure times in the order of streamers lifetime (1-10 ns) show a luminous region extending uniformly over the whole electrode surface (see Figure 1.10). In contrast, when the plasma is filamentary, several localized discharges are clearly visible, see Figure 1.11. Important physical differences between the characteristics of the plasma in a streamer (or micro-discharge) and that of diffuse plasma are to be noted. Of practical importance are the electron number density n_e, and

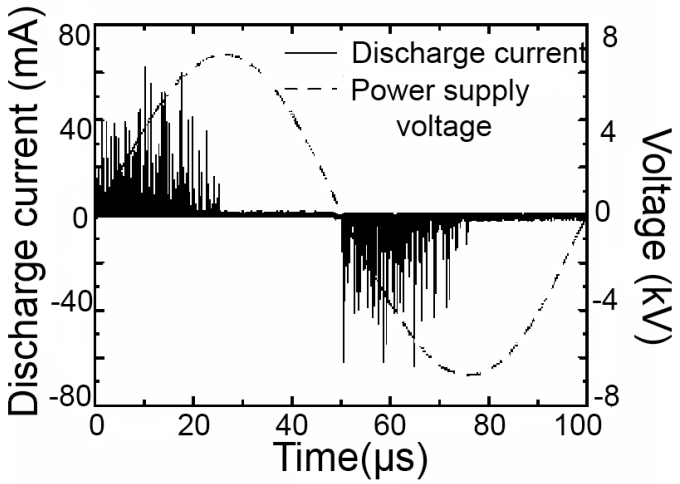

Figure 1.8: Current-voltage characteristics of a DBD in N_2 [68].

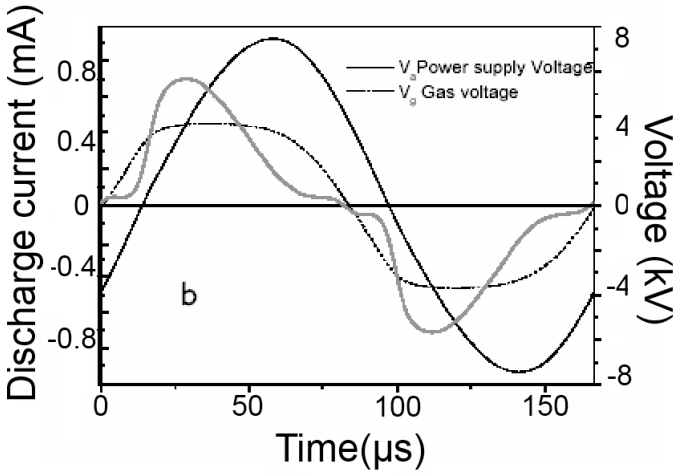

Figure 1.9: Current-voltage characteristics of a homogeneous DBD in N_2 [68].

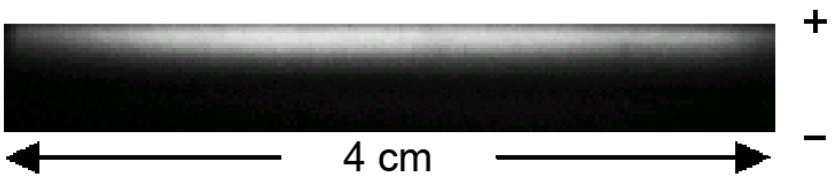

Figure 1.10: Ten nanoseconds (10 ns) exposure time photograph of a diffuse DBD in N_2 [68].

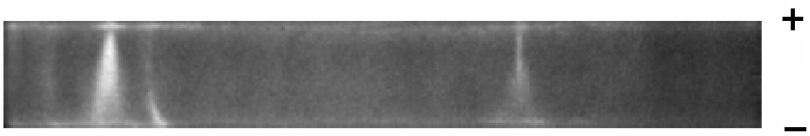

Figure 1.11: Ten nanoseconds (10 ns) exposure time of a filamentary DBD in N_2 [68].

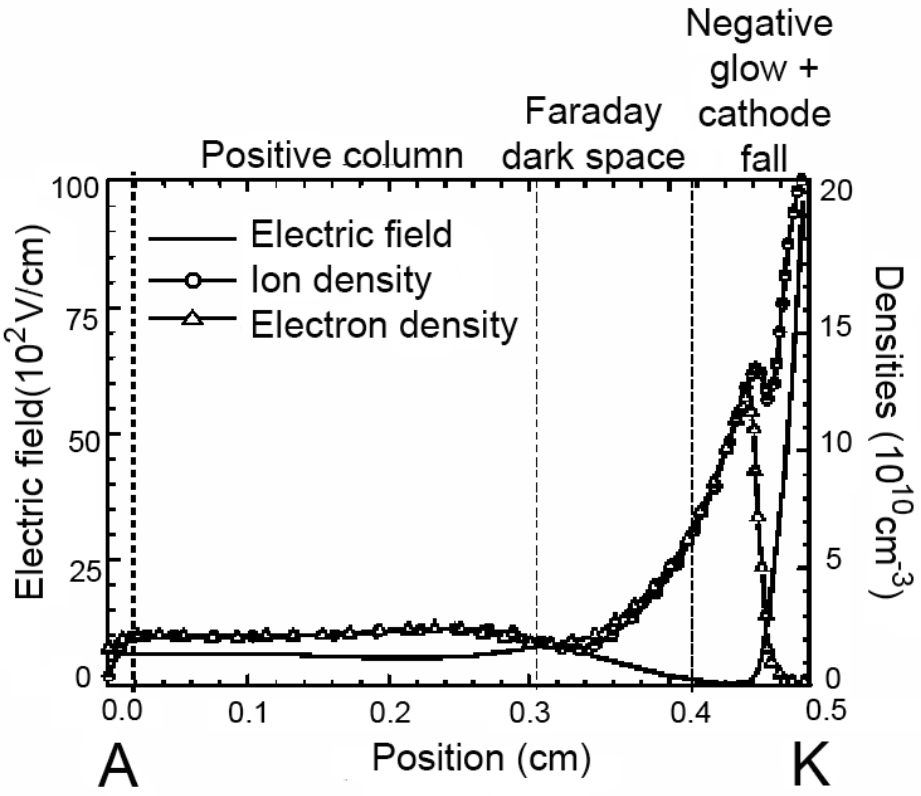

Figure 1.12: Electric field, electron density, and ion density spatial distributions between the anode and the cathode of a diffuse DBD in helium [36].

kinetic temperature, T_e. In a streamer n_e and T_e are in the 10^{14} - 10^{15} cm^{-3} and 1 - 10 eV range, respectively, while in a diffuse discharge n_e and T_e are in the 10^9 - 10^{11} cm^{-3} and 0.2 - 5 eV range, respectively.

Using a 1D fluid model, Massines calculated the distributions of the electric field, the electron density, and the ion density and showed that the homogeneous DBD exhibits a structure identical to the normal glow discharge (positive column, Faraday dark space, negative glow, etc). Figure 1.12 shows such spatial distributions between the anode and the cathode of a homogeneous DBD [36]. In case of AC voltage the anode and the cathode vary places with each other.

1.1.7 Surface treatment by DBD

The dielectric barrier discharge (DBD) seems to be the most promising plasma source for a plasma assisted treatment of large-area both metallic and polymer surfaces at atmospheric pressure. Investigations of the homogeneous DBD commonly known as atmospheric pressure glow discharge (APGD) [32], and of the filamentary or disperse DBD [73, 74, 75] proved the applicability of DBD for surface treatment techniques. Special applications of DBD under atmospheric pressure exist in the modification of large area surfaces for the purpose of the corrosion protection of metals and of an improvement of e.g. the wetting behaviour of polymers. The application of atmospheric pressure discharges has the chance of plasma treatment with cheap gas mixtures, low specific energy consumption and short processing time. Plasma processes in chemically reactive gases are comparatively easy to control. Moreover dry processes with low material insert are usually environmentally-friendly.

This modification process for metallic surfaces usually consists of three steps:

- the cleaning from oil and fat contaminations

	Cleaning	Oxidation	Deposition
Frequency / kHz	10 - 25	10 - 25	6.6
Voltage / kV	< 15 kV	< 15 kV	< 15 kV
Power / W	60 - 80	80	45
Power density / Wcm^{-3}	2.2 - 3.0	3	1 - 1.6
Dosage / J cm^{-3}	5 - 10	5 - 10	50 - 80
Discharge gap / mm	1.3	1.3	0.5
Process gas	Dry air	Dry air	N_2
Reactive gas	O_2 20%	O_2 20%	TEOS 0.1%
Gas flow / slm	1.6	1.6	1
Effect. treatment time / s	< 120	< 600	< 90
Mean residence time / s	0.06	0.06	0.1
Volume power density / Wcm^{-3}	20 - 60	30 - 60	10 - 30

Table 1.2: Typical operation conditions during DBD-plasma treatment [76] .

- the deposition of a stable oxide layer of some tens of nm to the protecting of the metallic bulk material

- the deposition of an anticorrosive and adhesive thin film,several hundred nm thick [76].

The typical operation conditions during plasma treatment are represented in Table 1.2 [76].

1.2 Atmospheric pressure dielectric barrier torch discharge

1.2.1 Introduction

Dense atmospheric-pressure plasma can be produced through dc or low frequency discharge operating in the high current diffused arc mode, such as a plasma torch [77, 78, 79], which introduces a gas flow to carry the plasma out of the discharge

region. Non-transferred DC plasma torches [80, 81] are usually designed for power levels over 10 kW. The volume of a single torch is generally restricted by the gap between the electrodes, which is, in turn, limited by the available voltage of the power supply. A simple way to enlarge the plasma volume is to light up an array of torches simultaneously [78]. The torches in an array can be coupled to each other, for example, through capacitors. In doing so, the number of power sources needed to operate the array can be reduced considerably, so that the size of the power supply can be reduced.

The atmospheric plasma deposition of various thin films is a subject of great interest recently. A large amount of systems for atmospheric Plasma Enhanced Chemical Vapour Deposition (PECVD) has been developed. Low temperature dielectric-barrier discharges [19, 23, 36, 70] are very often applied for PECVD deposition of polymer and other kinds of thin films [34, 81, 82]. Some other types of RF atmospheric plasma sources are now investigated; as example we can quote:

- A new type of RF non-equilibrium ("cold") plasma source operating at atmospheric pressure in an open reactor is Fused Hollow Cathode (FHC) discharge. It was used for surface processing, especially on temperature sensitive substrate. FHC discharge operates in the pressure range from 1 Torr to atmospheric pressure [83].

- Atmospheric Pressure Plasma Jet (APPJ) employs to produce a stable discharge at atmospheric pressure. The gas temperature of the discharge was typically between 50 - 300 °C [84].

- Plasma channel created by means of mentioned RF unipolar plasma discharge is discussed in [85].

- Plasma jet operated by feeding working gases between 2 coaxial electrodes

was presented in [86].

These configurations of cold RF atmospheric plasma jets and RF torch plasma sources were used for thin films deposition as well.

1.2.2 The RF atmospheric torch discharge configuration

The RF torch discharge stabilized by the working gas flow

RF torch discharge [87, 88, 89], stabilized by the working gas flow, is schematically drawn in Figure 1.13. The powered electrode of the torch discharge is made up of the metal cylindrical nozzle with an inner diameter of 1-2 mm and a length of several centimeters. The powered electrode is connected through a matching unit to the RF generator with a frequency of 13.56 MHz. When the applied RF power in the plasma is kept below a certain limit, the unipolar torch discharge is generated at the edge of the nozzle [87, 88, 89]. When the RF power absorbed in the torch discharge is adjusted above this limit, the electrode edge can be locally overheated and, on further increasing of the absorbed RF power, thermionic emission from the nozzle can occur and the torch discharge can go over into a regime of an arc torch discharge. Hence, the metallic nozzle and even substrate could be undesirably overheated and subsequently melted. This is a disadvantage of this system. The advantage of this system is that it is possible to use it up to atmospheric pressure. The torch discharge works even in the liquid environment [91].

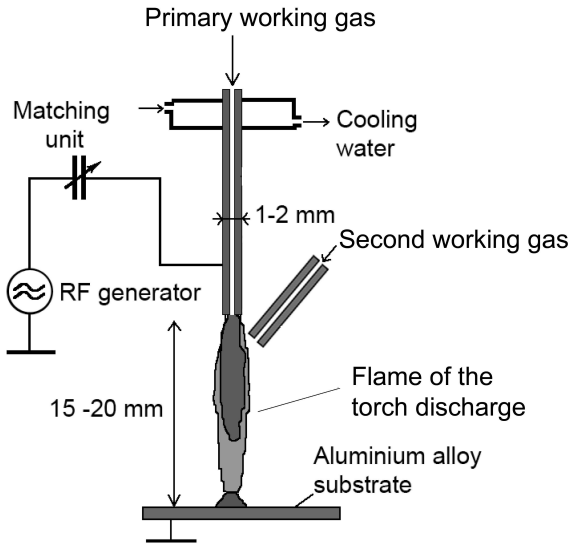

Figure 1.13: Arrangement of the RF torch deposition system [90].

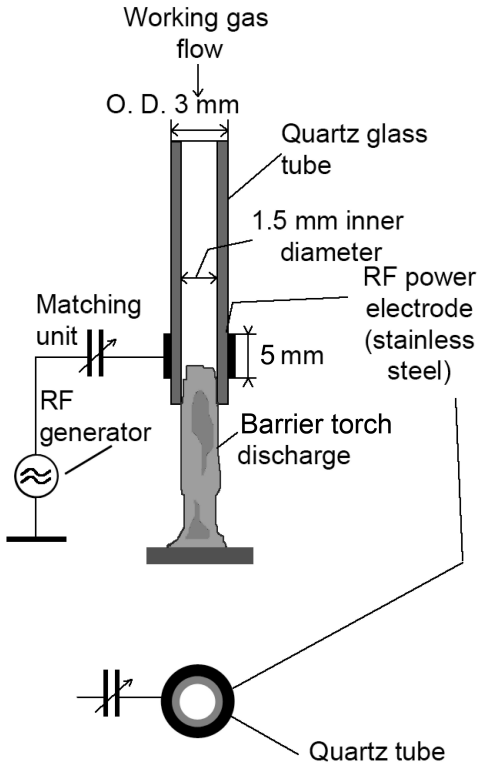

Figure 1.14: The barrier torch discharge configuration [90].

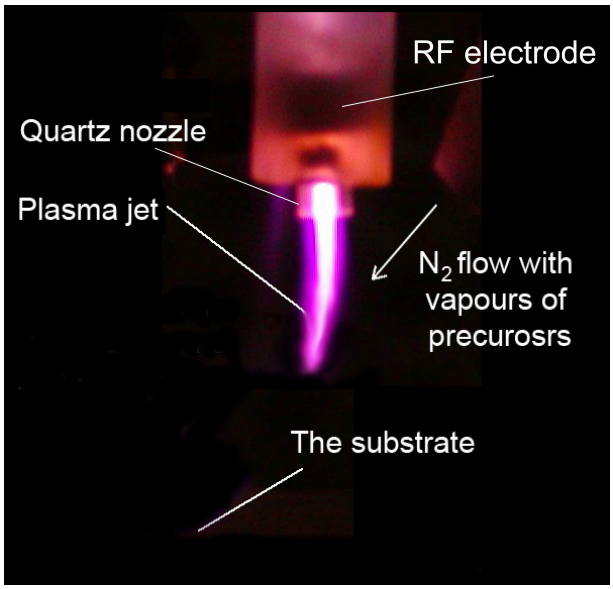

Figure 1.15: Photograph of the atmospheric barrier torch discharge in mode A without interaction of the emitting plasma jet with the substrate [92].

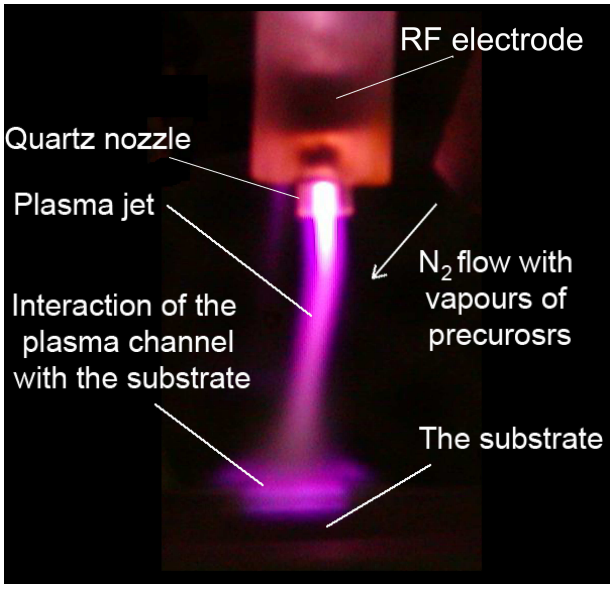

Figure 1.16: Photograph of the atmospheric barrier torch discharge in mode B when the interaction of the emitting plasma jet with the substrate is apparent. Applied RF power was pulse modulated in this case [92].

The RF barrier torch discharge with single plasma jet channel

Due to the mentioned disadvantages of the torch discharge regarding the nozzle and substrate overheating or possible arc transition, a modification of this system on the torch-barrier discharge was performed. Basically, a dielectric layer was placed on the inner walls of the metallic nozzle, as can be seen in Figure 1.14. The RF power absorbed in this system can be adjusted so that the so-called RF barrier torch discharge is generated near the sharp edge of the insulated metallic power electrode. The working gas flowing through the nozzle stabilizes this barrier torch discharge and a well-defined discharge channel is created.

The system can be operated in two basic modes [92]. In the first mode, A, the interaction of the light emitting plasma jet with the substrate does not occur as can be seen in Figure 1.15. This situation takes place when the applied RF power on the system is below ∼180 W.

In the second mode, B, the light emitting plasma jet directly interacts with the substrate surface. The situation can be seen in Figure 1.16. The plasma channel sharply converts into mode B when the applied RF power reachs P_{RF} ∼180 W.

The advantage of this system is that the metal surface of the power electrode is separated from direct interaction with the high-density plasma. Therefore, the chemical processes in the plasma are not affected by the metallic RF electrode surface. The RF barrier torch discharge is a new discharge in which the dielectric layer is added into the current path. For this reason, its property should be different from the original torch discharge with the metallic nozzle electrode. The RF barrier torch discharge with single plasma jet channel can also be generated in pulse regime.

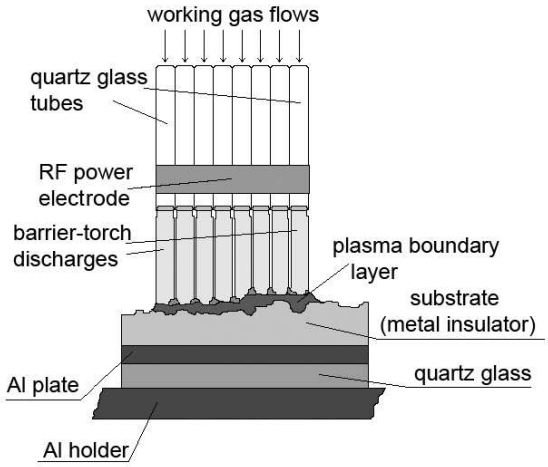

Figure 1.17: Barrier multi torch discharge configuration [90].

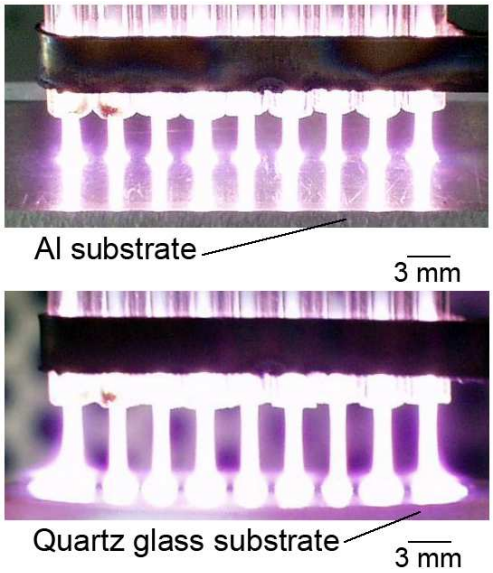

Figure 1.18: Photographs of light emission from barrier multi torch discharge: (a) Al substrate; (b) quartz glass substrate [90].

Barrier multi torch discharge operation

The RF barrier multi torch discharges with nine quartz nozzles is depicted in Figure 1.17. Dimensions of the quartz tubes were analogous with the quartz tube in the single nozzle version depicted in Figure 1.14. Helium flows through each nozzle. Both quartz glass and aluminum substrates could be used.

In order to demonstrate the possibility of the coating and surface treatment of thermally sensitive substrates by using the presented system, an RF pulse-modulated barrier multi torch discharge was used. In this case, the PVC or quartz glass plate substrates were used. The distance between the PVC or quartz substrate and the nozzle outlet was set up to 10 mm. The length of the period was 3.2 ms and the active part of the period was 50 μs when maximum RF power P_{RF}= 600 W was applied on the discharge with matching unit (duty cycle 1,6%).

On the other hand, the mean power absorbed in the discharge over the whole

period was low enough to avoid PVC substrate damage. Photographs of light emission of the multi-torch barrier discharge with quartz and Al substrate are presented in Figure 1.18. The distribution of light emission in each particular discharge channel was qualitatively analogous to the emission from the barrier single torch discharge channel with the quartz nozzle. It can be seen that the discharge channel spreads out at the substrate surface and this effect was stronger in case of the quartz substrate, because Al substrate created the virtual cathode.

It was demonstrated that the stable operation of the multi jet version both with aluminum and quartz substrates is also possible in case of substrates with non-flat surface. Particularly quartz and aluminum plates with holes of diameter 5mm and 3mm depth were used.

The obtained experimental results indicate that the most significant factor affecting the multi-jet stabilization is a sufficient magnitude of the He gas flow in each particular nozzle. This flow stabilizes homogeneity of this multi-jet source even in the case of non-flat substrates. It has been experimentally found that if the He gas flow in each nozzle was decreased below <70 sccm, the barrier torch discharge channels were not stable and the torch plasma shrank to only one single jet randomly generated just inside one of the nozzles.

1.3 The methods used for the plasma diagnostic

1.3.1 Probes

Langmuir probe

Langmuir probe is a device named after Nobel Prize winning physicist Irving Langmuir, used to determine the electron temperature, electron density, plasma

potential and electron energy distribution function. Measurements with Langmuir probes, are the oldest and most often used diagnostic procedures for low-temperature plasmas. The method was developed by Irving Langmuir and his co-workers in the 1920s, and has since been further developed in order to extend its applicability to more general conditions than those presumed by Langmuir. Langmuir probe measurements are based on the estimation of current versus voltage characteristics (Figure 1.21) of a circuit consisting of two metallic electrodes that are both immersed in the plasma under study (Figure 1.19). Two cases are of interest:

- The surface areas of the two electrodes differ by several orders of magnitude. This is known as the single-probe method.
- The surface areas are very small in comparison with the dimensions of the vessel containing the plasma and approximately equal to each other. This is the double-probe method.

The Langmuir probe is usually constructed in simple geometric shapes: spherical probe, cylindrical probe and planar (flat) probe, see Figure 1.20. When constructing the probe we have to take into account that not only the active metallic part, i.e., the collecting surface of the probe, has to be small in comparison with the characteristic dimensions of the plasma vessel. The isolated parts of the probe must fulfill the same condition since often just these passive parts substantially influence the plasma around the probe. Conventional Langmuir probe theory assumes collisionless movement of charge carriers in the space charge sheath around the probe. Further it is assumed that the sheath boundary is well-defined and that beyond this boundary the plasma is completely undisturbed by the presence of the probe. This means that the electric field caused by the difference between

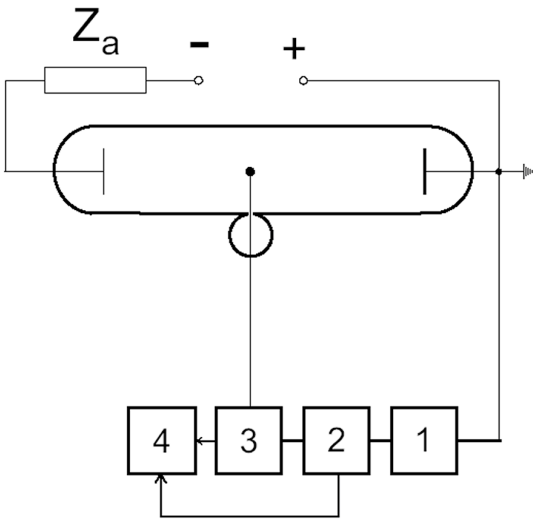

Figure 1.19: Typical probe circuit. 1 DC bias voltage, 2 sawtooth ot staircase U_p generator, 3 current-voltage converter, 4 $I_p - U_p$ data acquisition (computer) [93].

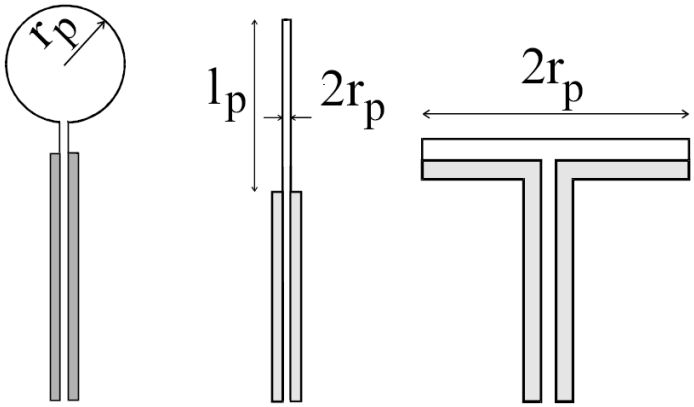

Figure 1.20: Typical shapes of Langmuir probes [93].

the potential of the probe and the plasma potential at the place where the probe is located is limited to the volume inside the probe sheath boundary. The general theoretical description of a Langmuir probe measurement requires the simultaneous solution of the Poisson equation, the collision-free Boltzmann equation and the continuity equation with regard to the boundary condition at the probe sur-

face and requiring that, at large distances from the probe, the solution approaches that expected in an undisturbed plasma.

Voltage-current characteristic

A typical probe voltage-current characteristic taken in low-temperature non-isothermal discharge plasma is shown in Figure 1.21. Let us assume that the probe potential Φ_p differs from the plasma (space) potential Φ_s at the place where the probe is located by $U_p = \Phi_p - \Phi_s \neq 0$

Three regions can be clearly distinguished in the course of the probe characteristics. Assuming that no negative ions exist in the plasma the probe current consists of the electron and the positive ion current. The three regions of the probe characteristics are characterized by [93]:

1. $U_p \leq 2U_{fl} \rightarrow |I_{pi}/I_{pe}| \gg 1$ Positive ion acceleration region
2. $2U_{fl} < U_p < 0 \rightarrow |I_{pi}/I_{pe}| \approx 1$ Transition region
3. $0 \leq U_p \rightarrow |I_{pi}/I_{pe}| \ll 1$ Electron acceleration region

In the ion acceleration region (sometimes called ion saturation region since the ion current is close to saturation) an almost pure positive ion current flows to the probe. At the floating potential the electron and the positive ion current compensate each other and the total probe current equals to zero. For positive probe voltages the electron current dominates the probe current; the probe operates in the electron acceleration region. If the probe immersed into plasma is not connected to the outer circuit, and therefore it cannot carry the current, then the probe is negatively charged with respect to the plasma potential. This takes place since the electrons (even at the same temperature like positive ions) have a much higher thermal velocity due to their much lower mass (typically for argon

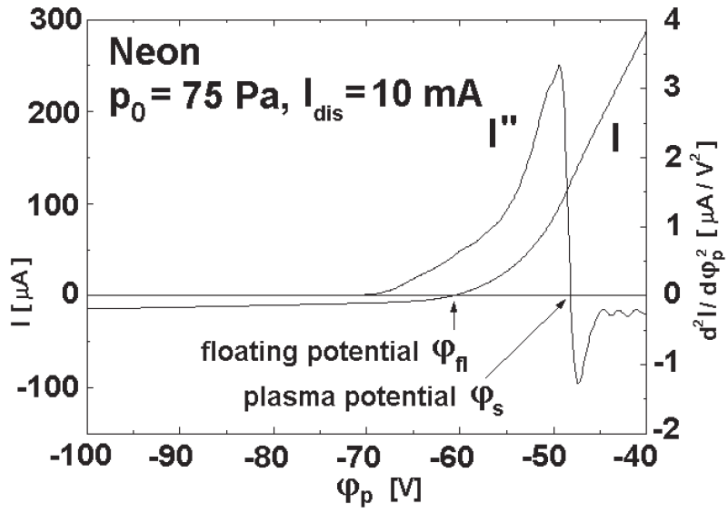

Figure 1.21: Typical course of the probe characteristics (left scale) with its second derivative (right scale)[93].

is the square root of the mass ratio around 300). The more negative potential of the probe, in consequence, attracts more positive ions, and this process continues until the electron and the positive ion current components equal each other; the floating potential is established on the probe.

Double probe

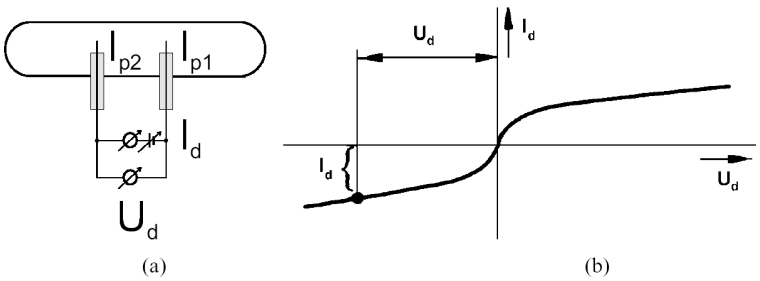

Figure 1.22: (a) Basic double probe circuit. (b) Typical double probe characteristics [93].

When a voltage is applied between two small electrodes immersed in plasma a current flows, and the current-voltage characteristics resemble the ion current

part of the single probe characteristics in both polarities of the applied voltage (see Figure 1.22). In fact the single probe technique obeys the same laws, only one of the electrodes has a much larger surface area than the other one. Therefore we speak of a double probe method only, if the surface areas of both electrodes are small and not very different from each other. The advantage of the double probe method is that it does not need the large reference electrode and therefore can be applied in electrode-less (RF generated) plasma. The double probe technique is usually applied to measure the electric field in a discharge plasma, but it can also be applied to determine the electron temperature and, at certain experimental conditions, the plasma density. A usual arrangement in the double probe technique places both probes close to each other so that it is possible to assume that the plasma parameters are the same at both probe positions. If, moreover, both the probes have the same shape and the same surface collecting area, the resulting current-voltage characteristic is centresymmetrical with respect to the point of zero current.

Since the total current drawn by the double probe system from the plasma is zero (the system is floating) it is evident that the current, carried to one probe by particles of a certain charge must be compensated by the current of the second probe due to carriers of the opposite charge. Denoting the first and second probe by the subscripts 1 and 2, respectively, we can write down the following equations based on Kirchhoffs laws:

$$I_{pe1} + I_{pi1} = -(I_{pe2} + I_{pi2}) = I_d \tag{1.1}$$

1^{st} Kirchoff law

$$U_1 = U_2 + U_d \tag{1.2}$$

2^{nd} Kirchoff law

where

$I_{pe1} = I_{pe1}(U_1)$ and $I_{pi1} = I_{pi1}(U_1)$

$I_{pe2} = I_{pe2}(U_2)$ and $I_{pi2} = I_{pi2}(U_2)$

Here $U_{1,2}$ denotes the probe voltage with respect to the space potential, and U_d is the voltage between the two probes.

In case of a Maxwellian EEDF it is possible to use the following expression for the electron probe current to the first probe:

$$I_{pe1} = I_{pe}(U_1 = 0)\exp(-\frac{q_0 U_1}{k_B T_e}) \tag{1.3}$$

a similar expression is valid for the second probe. The current in the double probe circuit then is given by:

$$I_d(U_d) = I_{pi1}(U_1) + I_{pe1}(U_1 = 0)\exp(-\frac{q_0 U_1}{k_B T_e}) \tag{1.4}$$

$$-I_d(U_d) = I_{pi2}(U_2) + I_{pe2}(U_2 = 0)\exp(-\frac{q_0 U_2}{k_B T_e}) \tag{1.5}$$

If we differentiate this double probe characteristics with respect to U_d and take into account that $(dU_d = dU)_{fl} = 2$, then we obtain the expression for the electron temperature firstly derived by Johnson and Malter [94]:

$$\frac{k_B T_e}{q_o} = [2(x\frac{dI_d}{dU_d})_{fl} - \frac{1}{2}(\frac{dI_{pi1}}{dU} + \frac{dI_{pi2}}{dU})_{fl}]^{-1} \times \frac{2(I_{pi1})_{fl}(I_{pi2})_{fl}}{(I_{pi1})_{fl} + (I_{pi2})_{fl}} \tag{1.6}$$

The great advantage of this method is its insensitivity to the effect of collisions in the space charge sheath around the probe.

The double probe technique can also be used for the plasma density estimation provided that the model of the positive ion collection by the probe which is suitable for the particular experimental conditions can be applied. A fairly general model has been derived in Ref. [95].

The results presented in [96, 81, 82] theoretically show that the double probe method is comparatively insensitive of pressure and allows the determination of the electron temperature in the plasma up to the atmospheric pressure. Electron temperature of RF barrier torch discharge using double probe method was measured by M. Cada et al. [97]. These measurements revealed that the electron temperature in the RF barrier torch discharge was $T_e \approx 6$ eV in the single torch system and $T_e \approx 3$ eV in four torch system and varied depending on the applied power.

1.3.2 Plasma spectroscopy

Plasma spectroscopy is one of the most established and oldest diagnostic tools in astrophysics and plasma physics. Radiating atoms, molecules and their ions provide an insight into plasma processes and plasma parameters and offer the possibility of real-time observation. Emission spectra in Figure 1.23 in the visible spectral range are relatively easy to obtain with a quite simple and robust experimental set-up.

The method of Optical Emission Spectroscopy (OES) is non-invasive, which means that the plasma is not affected. In addition, the presence of RF fields, magnetic fields, high potentials etc. does not disturb the recording of spectra. Also the set-up of the experiment is comparatively simple: only diagnostic viewing ports are necessary which are transparent in the requested wavelength range. Thus plasma spectroscopy is an indispensable diagnostic technique in plasma

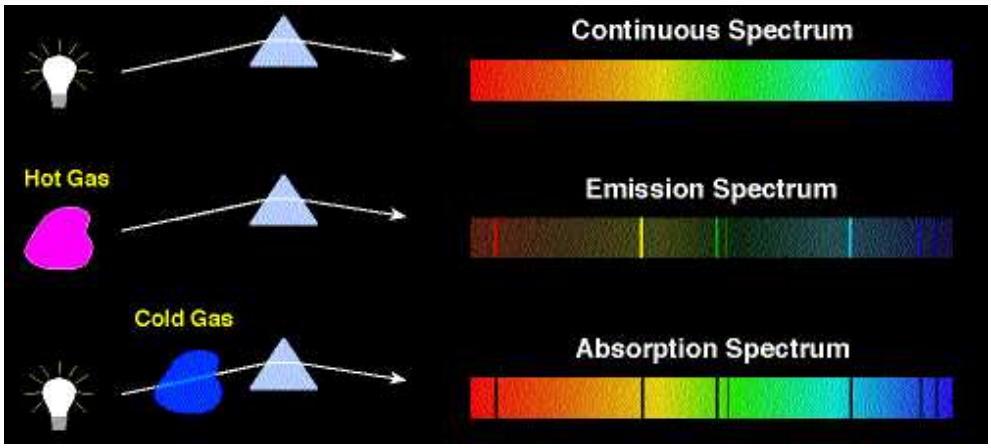

Figure 1.23: Emission and absorption spectra [98].

processing and technology as well as in fundamental research. Although spectra are easily obtained, interpretation can be fairly complex, in particular, in low temperature, low pressure plasmas which are far from thermal equilibrium, i.e. in non-equilibrium plasmas [99].

Radiation in the visible spectral range

Electromagnetic waves extend over a wide wavelength range, from radiowaves (kilometre) down to γ -rays (picometre). The visible range is only a very small part ranging from 380 to 780 nm by definition. However, common extensions are to the ultraviolet and the infrared range resulting approximately in a measurable wavelength range from 200 nm to 1μm. From the experimental point of view this wavelength region is the first choice in plasma spectroscopy: air is transparent, quartz windows can be used and a variety of detectors and light sources are available. Below 200 nm quartz glass is no longer transparent and the oxygen in the air starts to absorb light resulting in the requirement of an evacuated light path. Above 1μm the thermal background noise becomes stronger which can only be compensated for by the use of expensive detection equipment. Radiation in the

visible spectral range originates from atomic and molecular electronic transitions. Thus, the heavy particles of low temperature plasmas, the neutrals and their ions basically characterize the colour of a plasma: typically a helium plasma is pink, neon plasmas are red, nitrogen plasmas are orange and hydrogen are purple-these are the first results of spectroscopic diagnostics using the human eye.

Emission and absorption

In general, plasma spectroscopy is subdivided into two types of measurements: the passive method of emission spectroscopy and the active method of absorption spectroscopy. In the case of emission spectroscopy, light emitted from the plasma itself is recorded. Here, one of the basic underlying processes is the excitation of particles (atoms, molecules, ions) by electron impact from level q to level p and the decay into level k by spontaneous emission with the transition probability A_{pk} resulting in line emission ε_{pk}. In the case of absorption spectroscopy, the excitation from level q to level p takes place by a radiation field (i.e. by absorption with the transition probability B_{qp}) resulting in a weakening of the applied radiation field which is recorded. The intensity of emission is correlated with the particle density in the excited state $n(p)$, whereas the absorption signal correlates with the particle density in the lower state $n(q)$, which is in most cases the ground state. Thus, ground state particle densities are directly accessible by absorption spectroscopy; however, absorption techniques need much more experimental effort than emission spectroscopy. Also, absorption of radiation in a plasma means that the method is no longer non-invasive; however the influence of necessary beam can be mostly neglected.

I will focus on emission spectroscopy because in our work we used this diagnostic tool. Further information on absorption techniques and analysis methods

can be found in [100, 101, 102, 103].

Analysis of a spectral line [99]

The two axes of a spectrum are the wavelength axis and the intensity axis as shown in Figure 1.24. The central wavelength of line emission λ_0 is given by the

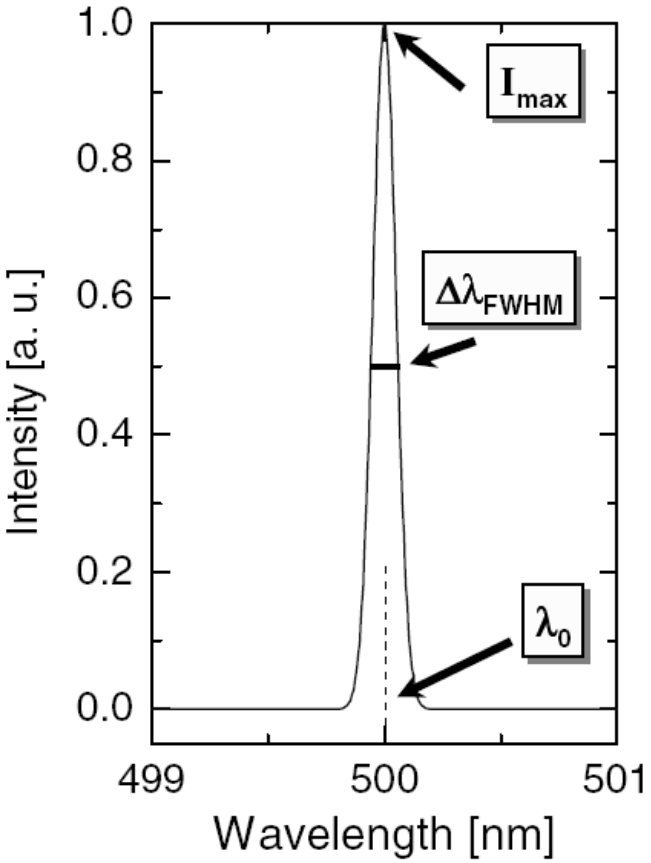

Figure 1.24: Line radiation and its characteristics [99].

photon energy $E = E_p - E_k$ corresponding to the energy gap of the transition from level p with energy E_p to the energetically lower level k (Planck constant h, speed of light c):

$$\lambda_0 = hc/(E_p - E_k) \tag{1.7}$$

Since the energy of a transition is a characteristic of the particle species, the central wavelength is an identifier for the radiating particle, unless the wavelength is shifted by the Doppler effect. Consequently, it is necessary to calibrate the wavelength depending on the used dispersion element of the used monochromator (prisma, grating). The line intensity is quantified by the line emission coefficient:

$$\varepsilon_{pk} = n_p A_{pk} \frac{hc}{4\pi\lambda_0} = \int_{line} \varepsilon_\lambda d\lambda \tag{1.8}$$

in units of W $(\mathrm{m}^2\ \mathrm{sr})^{-1}$ where 4π represents the solid angle. The line profile P_λ correlates the line emission coefficient with the spectral line emission coefficient ε_λ:

$$\varepsilon_\lambda = \varepsilon_{pk} P_\lambda \tag{1.9}$$

with

$$\int_{line} P_\lambda d\lambda = 1 \tag{1.10}$$

A characteristic of the line profile is the full width at half maximum (FWHM) of the intensity, $\Delta\lambda_{FWHM}$, as indicated in Figure 1.24. The line profile depends on the broadening mechanisms (see section Spectroscopic measurements of electron density from the Stark broadening of H_β line.).

Doppler effect The Doppler effect [1] causes the change in frequency and wavelength of a wave that is perceived by an observer moving relative to the source of the waves.

The thermal motion of ions will result in a broadening of emission lines. The

[1]The description in this paragraph has been created using the following web-based sources:
http://en.wikipedia.org/wiki/Doppler_effect
http://en.wikipedia.org/wiki/Plasma_diagnostics

magnitude of the shift is proportional to the velocity along the line of sight. This effect is known as Doppler broadening, from which the ion temperature can be determined.

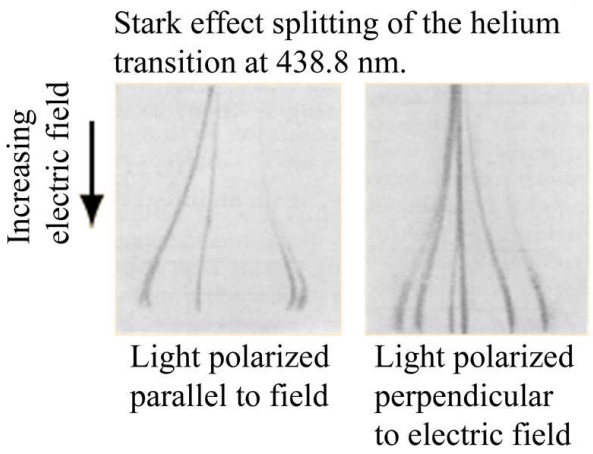

Figure 1.25: Stark effect [104].

Stark effect The splitting of atomic spectral lines as a result of an externally applied electric field was discovered by Stark, and is called the Stark effect (Figure 1.25) [2].

Result of Stark effect which arises due to electrostatic interaction during collisions, is a broadening of some lines that can be used to determine the density of the plasma.

1.3.3 Spectroscopic measurements of electron density from the Stark broadening of H_β line

When the electron density is sufficiently high and consequently the Stark broadening significant it is possible to determine the electron density from the width

[2]The description in this paragraph has been created using the following web-based source: http://hyperphysics.phy-astr.gsu.edu/hbase/atomic/stark.html

of Stark broadened spectral line, usually H_β line is used for this purpose [105].

In order to determine the electron density in an Ar DC torch discharge a small amount (about 0.2 % vol.) of water vapour was added to the Ar flow as a result we obtained a detectable intensity of H_β spectral line emission (486.13 nm) and exploited it for the electron density measurement. The H_β spectral line of the hydrogen Balmer series was observed in the emission spectrum due to dissociation of the water vapour in the Ar plasma column. The electron density in the plasma column was determined using the method based on the Stark broadening of H_β spectral line spontaneously emitted by the plasma.

The profile of an emission line can be, however, affected by different mechanisms of broadening [106]: natural, thermal Doppler, Stark (collisional) broadening, instrumental, etc. Generally, majority of the broadening mechanisms result in the emission lines with the Gaussian profile, except for the Stark broadening, which generates the Lorentzian profile of the emission lines [106]. The convolution of the Lorentzian (Stark) and Gaussian profiles results in the so-called Voigt profile.

In this investigations, following that described in [105], the Voigt function was fitted to the measured H_β line profile in order to estimate the full width at half maximum (FWHM) of the Lorentzian (Stark) profile $\Delta\lambda^{Stark}(H_\beta)$.

The electron density in the Ar plasma column was determined using either GKS theory or Gig- Card theory.

In the GKS theory (disclosed in [107], [108]), the Stark broadening is estimated in a quasi-static approximation using the classic Holtsmark field, resulting in the relation:

$$n_e = [10^9 * \Delta\lambda^{Stark}(H_\beta)/(2.5 * \alpha_{1/2})]^{1.5}[cm^{-3}] \tag{1.11}$$

where $\Delta\lambda^{Stark}(H_\beta)$ is measured in nm, and the electron density n_e is expressed in cm^{-3}. The $\alpha_{1/2}$ parameter (fractional semi-half-width) is tabulated in [108]. The simple relation for n_e obtained by Goktas et al. [109], for the electron temperature in the range of 1-4 eV and electron density between 10^{14} and 10^{18} cm^{-3}, is

$$n_e = 1.09 * 10^{16} * [\Delta\lambda^{Stark}(H_\beta)^{1.458}][cm^{-3}] \tag{1.12}$$

where $\Delta\lambda^{Stark}(H_\beta)$ is expressed in nm.

The more recent Gig-Card theory (disclosed in [110]) incorporates the ion dynamics to evaluate the Stark broadening of lines spontaneously emitted by the plasma [106]. It results in the relation between $\Delta\lambda^{Stark}(H_\beta)$, n_e and T_e as tabulated in [110]. We interpolated the values tabulated in [110], resulting in a simple relation between $\Delta\lambda^{Stark}(H_\beta)$ and n_e in the form of:

$$n_e = 10^{16} * [\Delta\lambda^{Stark}(H_\beta)^{1.55}][cm^{-3}] \tag{1.13}$$

where $\Delta\lambda^{Stark}(H_\beta)$ is in nm.

1.3.4 Electrical impedance measurements

Impedance analysis is a convenient and important diagnostic technique for plasma characterization [111]. By applying an electrical analog for modelling the overall behaviour of plasma, properties such as bulk electron density, sheath thickness and sheath voltage can be calculated from the measured impedance of the plasma. Knowledge of these properties helps to identify the dominant mechanisms in plasma processes. The plasma impedance is typically measured by observing the voltage and current waveform between the matching network and the electrode.

Impedance (Z) is generally defined as the total opposition a device or circuit offers to the flow of an alternating current (AC) at a given frequency, and is represented as a complex quantity which is graphically shown on a vector plane. An impedance vector (phasor) consists of a real part (resistance, Z_r) and an imaginary part (reactance, Z_{im}) as shown in Figure 1.26. Impedance can be expressed in the rectangular-coordinate form $Z_r + jZ_{im}$ or in the polar form as a magnitude and phase angle: $|Z| = \exp(j \cdot \Theta) = |Z|(\cos\Theta + j\sin\Theta)$. Figure 1.26 also shows the mathematical relationship between Z_r, Z_{im}, $|Z|$ and Θ. In some cases, using the reciprocal of impedance is mathematically expedient. In which case:

$$1/Z = 1/(Z_r + jZ_{im}) = Y = G + jB \tag{1.14}$$

where Y represents admittance, G conductance, and B susceptance. The unit of impedance is the ohm (Ω), and that of admittance is the siemens (S).

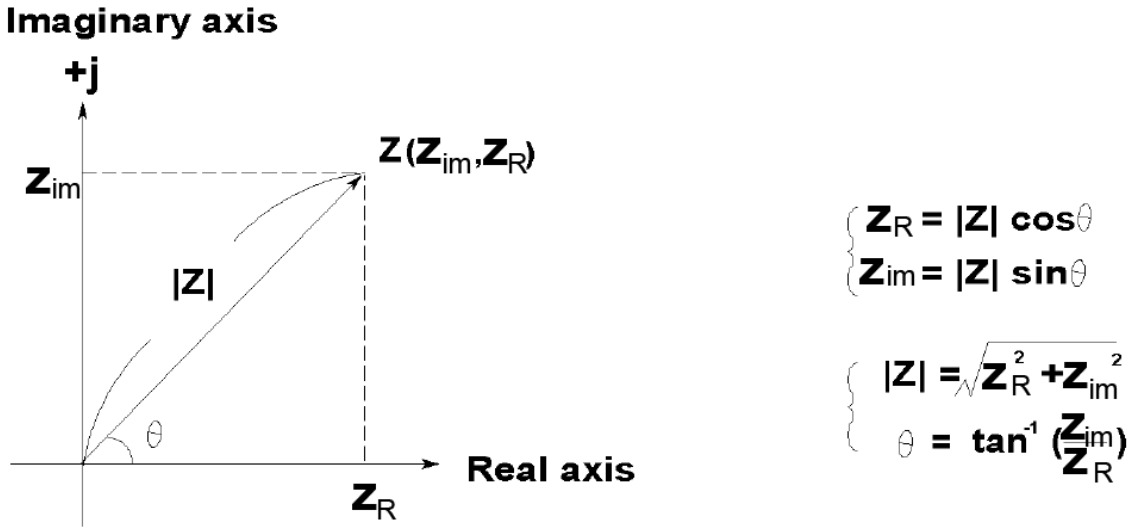

Figure 1.26: Impedance (Z) consists of a real part (Z_r) and an imaginary part (Z_{im}) [111].

Chapter 2

TiO_2 and ZnO thin films-their properties and applications

Chemical formula	TiO_2
Boiling point, °C	3562 [112]
Melting point, °C	1943 [112]
Density (g/cm^3)	4.26 [113]
Crystal structure	Tetragonal [113]
Band gap energy, eV	3.25
Lattice constant, E	a=4.593 c=2.958 [112]
Specific gravity	4.2 [114]
Mohs hardness	6.5 [114]
Refract. index. 550 nm	2.73 [115]

Table 2.1: Properties of Rutile.

2.1 Deposition of thin films

Atmospheric pressure barrier torch discharge was used for low temperature deposition of ZnO and TiO_2 thin films on glass, polymer, Al and quartz glass substrates.

2.1.1 TiO_2 thin films

Properties of titanium dioxide

Titanium dioxide (TiO_2)[1] is a crystalline material, commonly known as TITANIA with seven reported polymorphs, from which four are natural and others synthetic. Amorphous titania, Rutile, Anatase and Brookite are natural polymorphs.

Properties of Rutile

The stable form of titania is Rutile (see Table 2.1), to which the other forms of titania transform at sufficiently high temperatures. Rutile has a tetragonal

[1]This chapter has been prepared using several web-pages sources:
www.azom.com/details.asp?ArticleID=1179
www.specialchem4polymers.com/tc/Titanium-Dioxide/index.aspx?id=benefits_opacity

Chemical formula	TiO_2
Boiling point, °C	2500 - 3000 [117]
Melting point, °C	1855 [117]
Density (g/cm^3)	3.84 [113]
Crystal structure	Tetragonal [113]
Band gap energy, eV	3.23 [118]
Lattice constant, E	a=3.78 c=9.51 [112]
Specific gravity	3.8 - 3.9 [119]
Mohs hardness	5.5 - 6.0 [119]
Refract. index. 550 nm	2.55 [115]

Table 2.2: Properties of Anatase.

crystal structure in which the octahedra share four edges, see Figure 2.1.

This leads to the formation of chains, which are subsequently arranged in a four-fold symmetry, as shown in Figure 2.1.

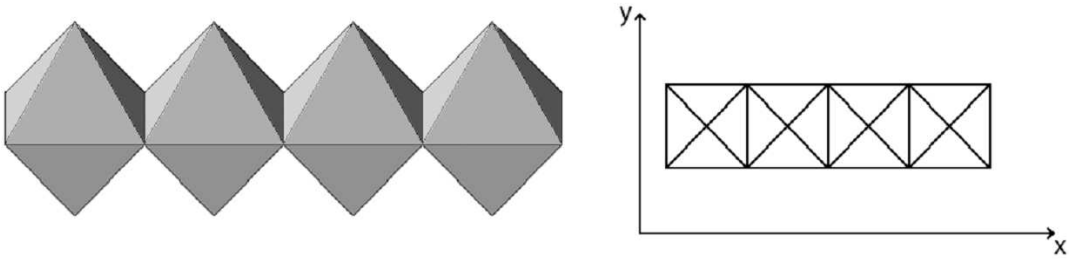

Figure 2.1: Rutile crystal structures [116].

Properties of Anatase

The predominant commercial phase of titanium dioxide is Anatase (see Table 2.2), although it is rarely found in ore form. It is thermodynamically metastable with respect to Rutile. Anatase has a tetragonal crystal structure in which the Ti-O octahedra share four corners, as shown in Figure 2.2. A comparison of Figure 2.1 and Figure 2.2 shows that the Rutile structure is more densely packed than Anatase.

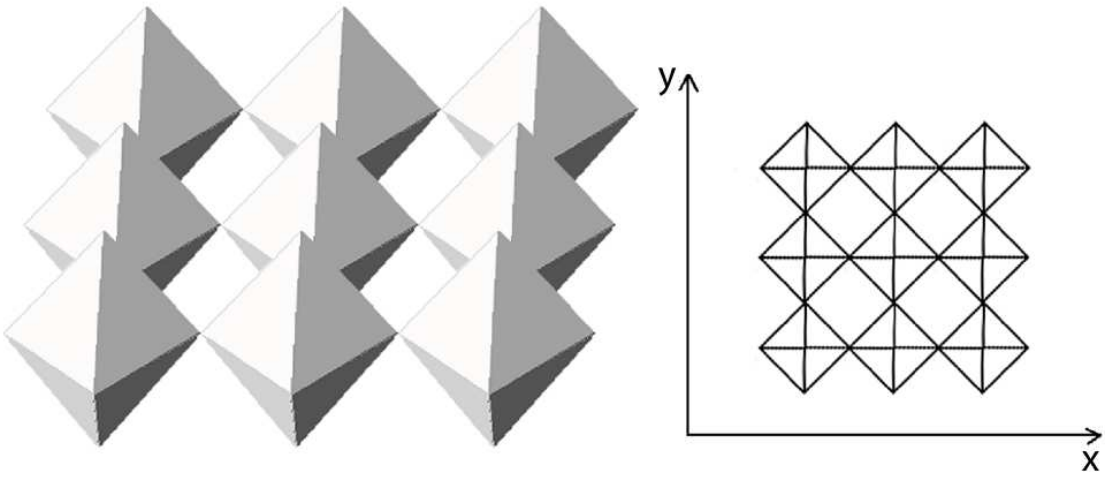

Figure 2.2: Anatase crystal structures [116].

Properties of Brookite

Brookite has an orthorhombic crystal structure and spontaneously transforms to Rutile at around 750 °C [121]. Its mechanical properties are very similar to those of Rutile, but it is the least common of the three phases and is rarely used commercially.

Amorphous-Anatase-Rutile Transformation

As we mentioned earlier, the structural phases possible in a titania layer are: amorphous, the metastable crystalline forms Brookite and Anatase, and the high temperature stable phase Rutile. Figure 2.3 summarizes schematically the precursor droplet transformation to a faceted TiO_2 particle, and the main intermediate stages.

Transformation from amorphous to Anatase form requires temperatures near 300 °C. Rutile exhibits the highest refractive index (and is birefringent) and as it follows from previous studies requires transformation temperatures in excess of 800 °C to form. The crystal-crystal attachment promotes Anatase - to - Rutile

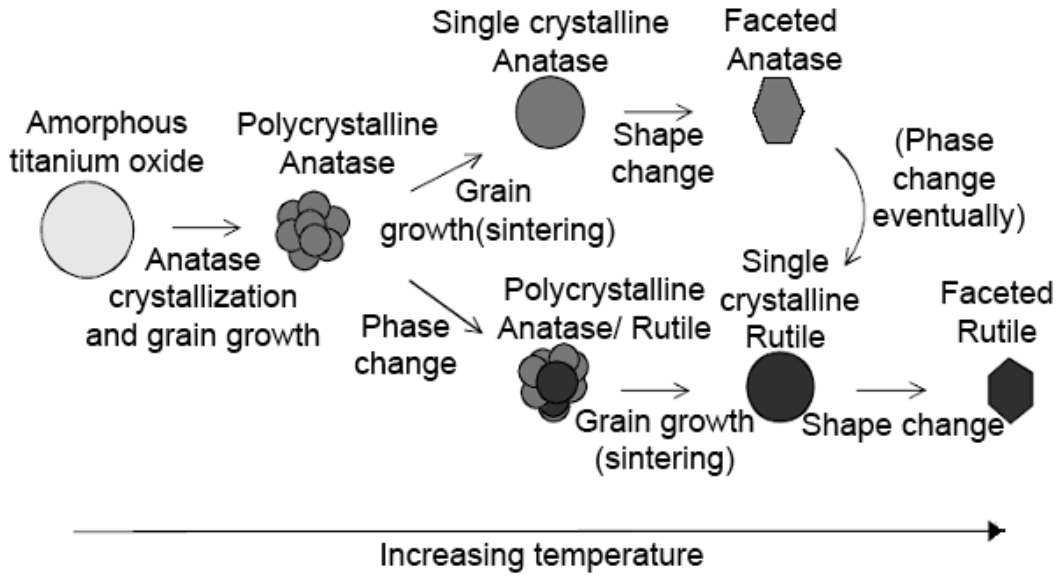

Figure 2.3: Mechanisms of ultrafine titanium dioxide particle crystallization [122].

transformation and therefore it is important to attain single crystalline Anatase at fairly low temperatures (<700-800 °C), if faceted Anatase is targeted. Small particle size is advantageous in forming single crystalline Anatase by sintering (agglomeration) but, in principle, a longer residence time would form single crystalline Anatase similarly at larger particles. The faceted Anatase crystallites showed increased thermal stability up to 1200 °C with regard to the Anatase - to - Rutile transformation [122]. Anatase can be transformed to Rutile at elevated temperatures, the transformation being exothermic.

Anatase-to-Rutile transformation is reinforced by JANAF (Joint Army - Navy - Air - Force - ARPA - NASA thermochemical working group) thermochemical data [123], which is shown in Figure 2.4. The JANAF data shows that the free energy of Rutile is always less than that of Anatase, making Rutile the more stable structure at all examined temperatures.

The generally accepted theory of the phase transformation is that two Ti-O bonds break in the Anatase structure, allowing rearrangement of the Ti-O

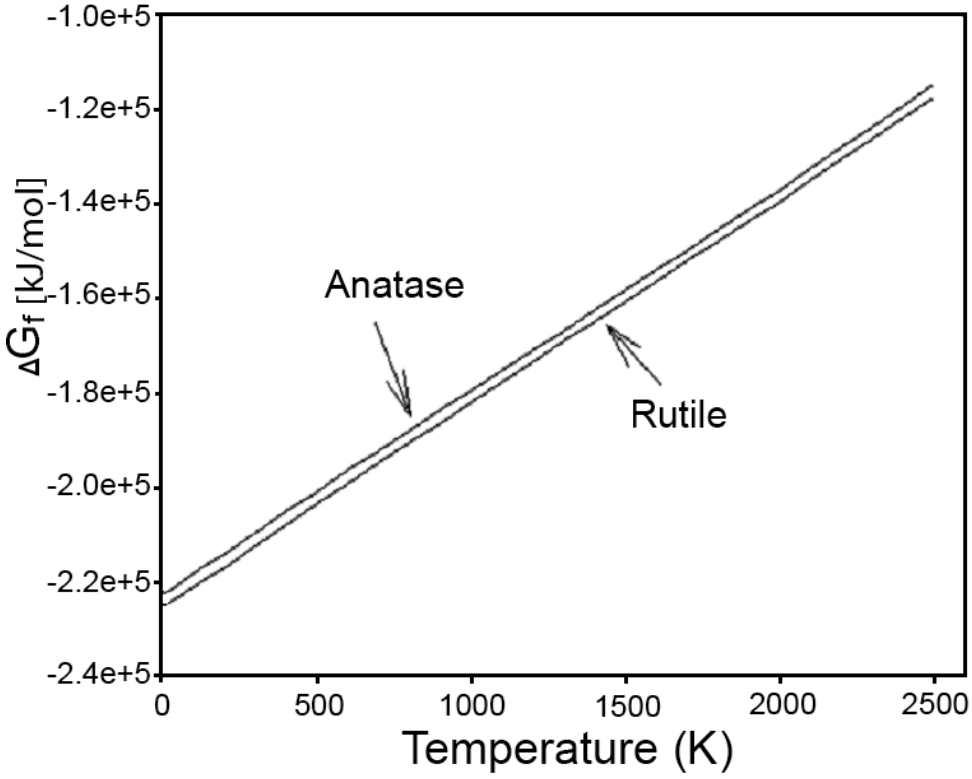

Figure 2.4: Free energy of formation of the Anatase and Rutile phases of TiO_2, as a function of temperature [123].

octahedra, which leads to a smaller volume and the Rutile phase. The breaking of these bonds is accelerated by lattice disruptions, which can be introduced in a number of ways, including the addition of dopants, variation in the atmosphere (oxygen partial pressure), and method of synthesis.

We succeeded to prepare layers of stable Anatase phase of TiO_2 at atmospheric pressure using the barrier torch plasma jet system as described in section 4.2.2.

Applications of titania

TiO_2 has been a subject of intensive research due to its outstanding physical and chemical characteristics. Applications for sintered titania (TiO_2) are limited by

its relatively poor mechanical properties. TiO_2 is a high bandgap semiconductor that is transparent to visible light and has excellent optical transmittance. TiO_2 has high refractive index (2.75 at 550 nm) and good insulating properties, and as a result it is widely used as protective layer for Very Large Scale Integrated (VLSI) circuits and for manufacture of optical elements.

Additionally TiO_2 films have potential uses for a number of electronic device applications such as dye-sensitized photovoltaic cells as well as AntiReflective (AR) coatings, gas sensors, electrochromic displays, and planar waveguides. The high dielectric constant of TiO_2 (ε_r $\sim$170), surpassed only by diamond allows its consideration as an alternative to silicon dioxide for ultrathin gate oxide dielectrics used in memory and logic devices. By far its most widely used application is as a pigment, where it is used in powder form, exploiting its optical properties.

Pigments

The most important function of titanium dioxide is using as a pigment for providing whiteness and opacity. Titanium dioxide is very widely used white pigment. The main advantages of the titanium dioxide is its resistance to discoloration under UV light. Titanium dioxide has very white colour and a high refractive index.

For understanding why titanium dioxide, especially the Rutile, has such great hiding power[2], we can compare the refractive index of Rutile to the refractive indices of Anatase and other commercial white pigments and polymer systems (see Figure 2.5).

Photocatalysis

When photocatalytic TiO_2 surface absorbs UV radiation from sunlight or

[2]Hiding power is an optical property used to describe the light -scattering efficiency of a white pigment. The hiding power of a paint measures its ability to obscure a background of contrasting colour. White pigments scatter incident visible light at all wavelength whereas coloured pigments absorb incident visible light at characteristic wavelength.

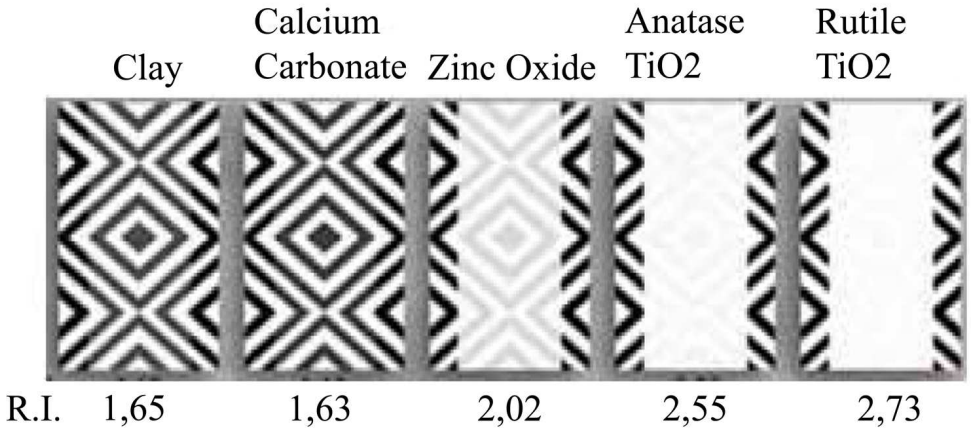

Figure 2.5: Effect of refractive index differences [115].

other source, electron excitation proceeds. The excited electron "jumps" to the conduction band of TiO_2, and electron (e^-) and positive-hole (h^+) pair is created.

This stage is named semiconductor's photo excitation stage. The energy between the valence band and conduction band is known as the "band gap". Wavelength of the light giving rise to photo-excitation is

1240 (Planck constant, h)/3.2 eV (band gap energy) = 388 nm

Water molecule dissociates on the photocatalytic surface to form hydrogen gas (H_2) and hydroxyl radical ($OH^\bullet$). Electron associates with oxygen molecule to form oxide anion (O^{2-})

Photocatalytically activated TiO_2 surfaces can be used for:

- air purification (remove of NO_x, SO_x, CO, formaldehyde, etc.)
- water purification (remove of organic substance, chloride, dyes, etc.)
- sterilization (remove of bacteria, fungal, algal, mold, duckweed, pest infestation)

- soil proof (oil soil, Rain Stain, Soot, self clean, anti-fogging function, etc.)

- deodorization (Tobacco odor, Garbage odor, Aldehyde, Ammonia, Mercaptan, Chloroform, etc.)

If the photocatalytic surface exposed to light for enough time it reaches superhydrophilic properties. On this surface water does not exist in the shape of the drop and spreads flatly on the surface.

Oxygen Sensors

Even small reduction of pressure induces loss of oxygen in titanium dioxide, and TiO_2 becoms substoichiometric (TiO_x[3]). Substoichiometric TiO_x is semiconductor and it is sensitive to the oxygen content of the atmosphere to which it is exposed. Oxygen content sensitivity alows the use of titania as oxygen sensor. This sensor type does not generate voltage but changes its electrical resistivity in response to the oxygen content.

Several methods have been used to prepare titania films, and these include chemical vapour deposition (CVD), pulsed laser deposition, reactive sputtering and sol-gel deposition.

TiO_2 thin films deposition using the barrier torch discharge is discussed below in chapters 4 and 5.

[3] TiO_x, x=decimal fraction

Chemical formula	ZnO
Melting point, °C	1975 [124]
Density (g/cm^3)	5.61 [124]
Crystal structure	Hexagonal [125]
Band gap energy, eV	3.37 [125]
Lattice constant, E	a=3.249 c=5.201 [125]
Specific gravity, g/cm^3	5.6 [126]
Mohs hardness	5 [125]
Refract. index. 550 nm	2.02 [115]

Table 2.3: Properties of ZnO.

2.1.2 ZnO thin films

Properties of ZnO

Zinc oxide (ZnO) [4] occurs naturally as the mineral ZINCITE. Zinc oxide is for the most part insoluble in water, but is soluble in acids and alkalis. It exhibits piezoelectric characteristics in thin film form. Such thin films can be deposited by processes like sputtering. Zinc oxide is also luminescent and light sensitive.

Applications of ZnO

Zinc oxide is a semiconductor with a direct band gap of 3.37 eV

ZnO has been pondered for spintronics applications [5] because of theoretical predictions of room temperature ferromagnetism [127].

ZnO layers are mainly deposited by sputtering and Chemical Vapour Deposition (CVD). CVD allows the growth of a rough layer. This layer enhances the incoming light by scattering, increasing the efficiency of solar cells. The de-

[4]The description in this chapter has been created using the following web-based sources:
www.azom.com/details.asp?ArticleID=2357
www.chemistrydaily.com/chemistry/Zinc_oxide
http://navbharat.co.in/clients.html.

[5]spintronics=spin electronics, the study of active control and manipulation of spin degrees of freedom in solid-state systems

position conditions of ZnO thin films deposited by barrier torch discharge, are described below in paragraph 5.2.1.

Zinc oxide films find applications in:

- Varistors which are used to prevent voltage surges in devices like mobile phones.
- Pigments in paints. Chinese white is a special grade of white pigment based on zinc oxide.
- A flux in ceramic glazes, where it can also help prevent crazing.
- A filler for rubber products.
- Coatings for paper.
- Sunscreens and sunblocks for the prevention of sunburn due to its ability to absorb ultraviolet light.
- Thin-film solar cells.
- LCD and flat panel displays.
- Gas sensors.

and many others [128].

2.2 The methods used for the analysis of the thin films

2.2.1 AFM - Atomic Force Microscopy

The atomic force microscope (AFM)[6] was invented in 1986 by Binnig, Quate and Gerber [129].

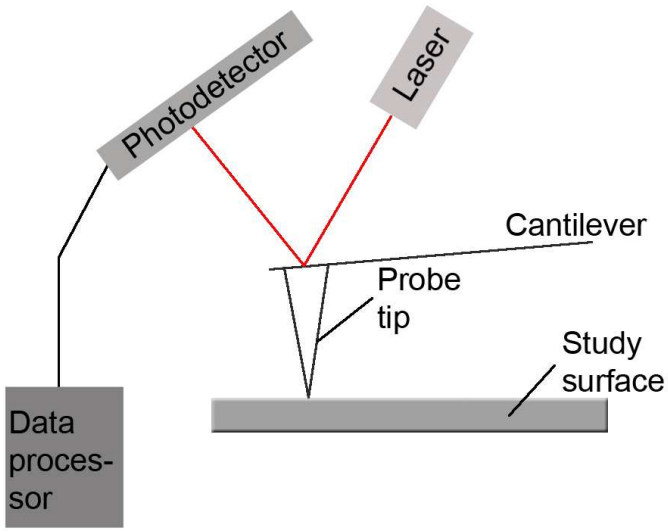

Figure 2.6: AFM principle [130].

As it can be seen in Figure 2.6 the probe is a tip on the cantilever which bends

[6]The description in this chapter has been created using the following web-based sources:
http://www.weizmann.ac.il/Chemical_Research_Support/surflab/peter/afmworks/index.html
http://vpd.ms.northwestern.edu/teaching/AFM_MSc_190_lab.pdf

in response to the force between the tip and the sample. If the tip changes height the light from laser reflected off the backside of cantilever senses this change, the reflected beam is directed on the multi-segmented photodiode. The photodiode can detect changes in movement of the beam and therefore of the tip on the cantilever; in such a way the height changes could be detected. The AFM allows making scan in sub-Angström resolution in x-, y- and z-directions. The z-axis is conventionally perpendicular to the sample.

The most common mode of the AFM operation is contact mode. The tip and sample are in the physical contact. This mode is nondestructive.

The contact mode can be used to collect 3D information in following resolution:

- 1.5 nm laterally
- 0.05 nm vertically

The usual method for displaying the data uses colour mapping for height, for example darker colour for low features and brighter colour for high features. A popular choice of colour scheme is shown below the title of this paragraph.

2.2.2 X-ray crystallography

A crystal is a solid with a regular internal 3D lattice. The periodic arrangement of this lattice can be studied with help of X-rays, because X-rays have a wavelength close to inter-atomic distance. The principle of XRD[7] is depicted in Figure 2.8.

The spacing in the crystal lattice can be determined using Bragg's law

$$n\lambda = 2d \sin\theta \tag{2.1}$$

[7]This chapter has been prepared using several web-pages sources:
http://en.wikipedia.org/wiki/X-ray_crystallography
http://chemistry.library.wisc.edu/instruction/xraycrystallography.htm

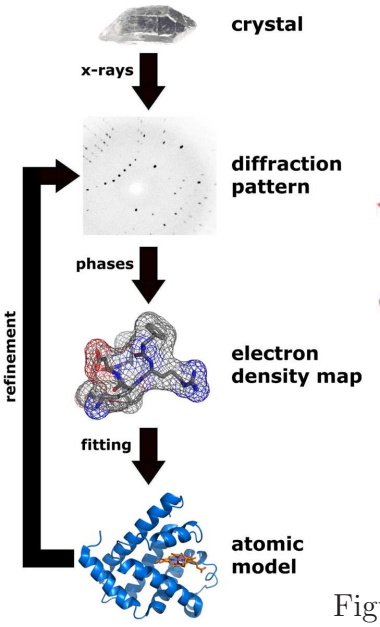

Figure 2.7: Scheme of the X-ray crystallography method [131].

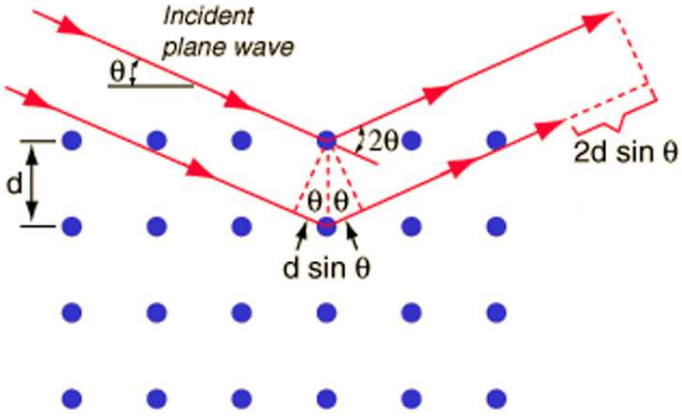

Figure 2.8: Scheme of the Bragg's Law (conductive interference)[132].

where d-distance, λ-wavelength, n-order of diffraction (n=1, 2, 3, ...), θ-angle between the incident rays and the surface of the crystal.

XRD (X-ray diffraction) analysis is widely used in chemistry and biochemistry to determine the structure of molecules.

2.2.3 Van der Pauw Method

The method was first propounded by L.J van der Pauw in 1958 [133].

This method is applicable for the measurements of the resistivity of random shaped film of uniform thickness planar wafer [134]. For our purposes, we assume that the contacts are small with respect to the wafer surface and are placed on the edge of the circled sample (see Figure 2.9). Let us define the resistance the $R_{AB,CD}$ as a ratio of the potential difference U_{CD} between contacts C and D, and

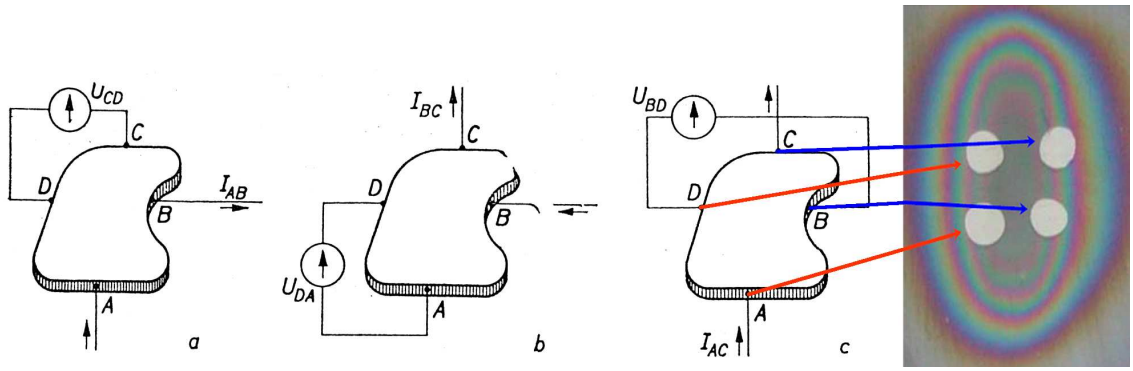

Figure 2.9: Scheme of the van der Pauw method: a) $R_{AB,CD} = U_{CD}/I_{AB}$, b) $R_{BC,DA} = U_{DA}/I_{BC}$, c) $R_{AC,BD} = U_{BD}/I_{AC}$ [134].

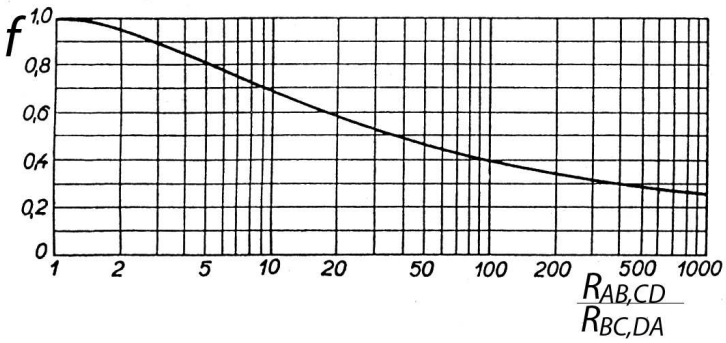

Figure 2.10: Correction factor f [134].

current labeled I_{AB} flowing between the sample contacts A and B (Figure 2.9). Similarly is defined the resistance $R_{BC,DA}$ (Figure 2.9). The equation that links resistivity ρ, sample thickness t and resistances $R_{AB,CD}$ and $R_{BC,DA}$ is as follows:

$$\exp(-\pi R_{AB,CD}t/\rho) + \exp(-\pi R_{BC,DA}t/\rho) = 1 \tag{2.2}$$

We can simplify this equation and get:

$$\rho = \frac{\pi \cdot t}{\ln 2} \cdot \frac{R_{AB,CD} + R_{BC,DA}}{2} \cdot f(\frac{R_{AB,CD}}{R_{BC,DA}}) \tag{2.3}$$

Where ρ - thin film resistivity [Ω cm], t - thin film thickness [nm], R - resistance [Ω], f -correction factor, σ - specific conductance [S/cm].

In this formula f is the function of the ratio $R_{AB,CD}/R_{BC,DA}$ (Figure 2.10). For the homogeneous sample with the circle shape and contacts placed symmetrically against each other, the expression $R_{AB,CD} = R_{BC,DA}$, is valid and, thus, the function f is equal to one.

Chapter 3

Aims of the PhD thesis

From the literature search as well as from the described preliminary experiments it follows that the barrier torch discharge is a system of favorable attributes, which could offer wide area of application in the future. Based on that the aims of the thesis were formulated as follows:

- study of the barrier torch discharge properties
- optimization of the deposition conditions
- study of the thin films properties

For these tasks the experimental equipment described in the following chapter was used.

Chapter 4

Experiment

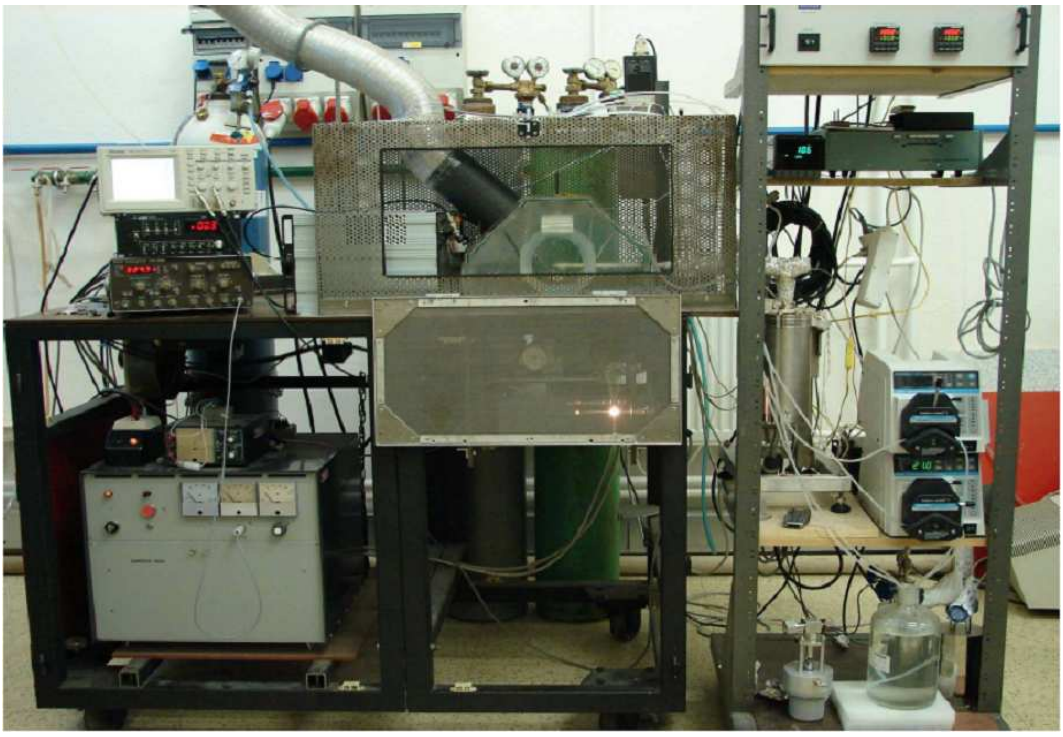

4.1 Single jet system

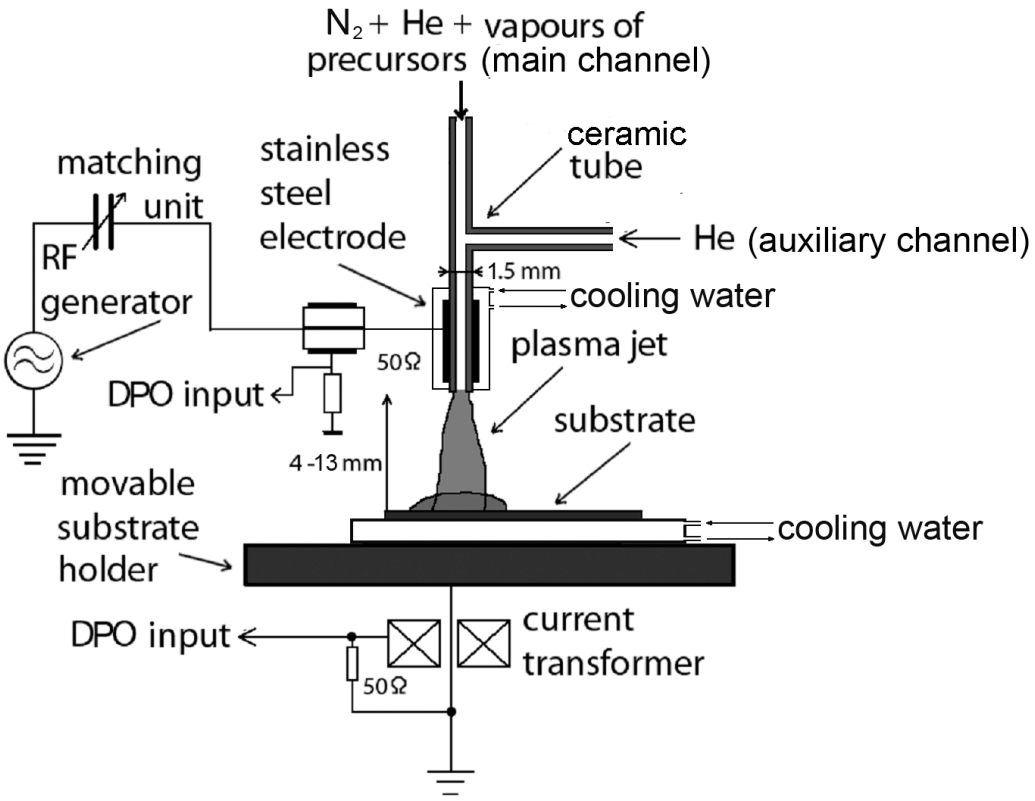

Figure 4.1: Barrier single torch discharge.

Schematic diagram of the newest configuration of the atmospheric pressure barrier single torch discharge can be seen in Figure 4.1. The system (Figure 4.1) works at the atmospheric pressure; it is just encased in acrylic glass box, which is provided by a pipe leading the used working gases out of the building. Precursors (Zn-acetylacetonate, Ti-thd and Ti-izopropoxide, see below the paragraph 4.3) can be treated at the atmospheric pressure, and their toxicity is moderately low.

The ceramic tube with internal diameter 1.5 mm is surrounded by the stainless steel RF powered electrode. This tube was cooled by water cooling system.

The photograph of the typical ignited atmospheric single plasma jet stream can be seen in Figure 4.2. Plasma system excited by RF source worked in pulse

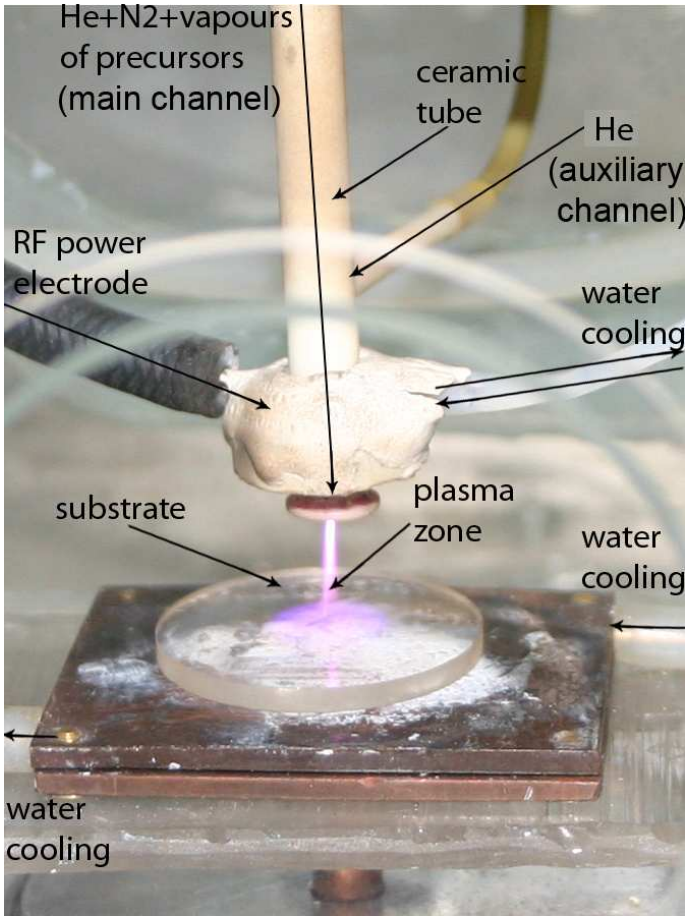

Figure 4.2: Typical ignited atmospheric single plasma jet stream (dielectric quartz glass substrate).

modulated mode in this case. This modulation allowed exciting of the high density plasma in the active part of the repetition period and simultaneously keeping the neutral gas in the plasma jet near the substrate reasonably cold thus protecting dielectric/polymer substrate from thermal damages. The repetition frequency was 20-40 Hz. Length of the active part of the cycle was 5 ms when full RF power (600W) was applied on the electrode (duty cycle 1:9 at frequency 20 Hz). The RF electrode was connected with the 13.56 MHz RF power generator via the matching unit.

4.2 Barrier multi torch discharge

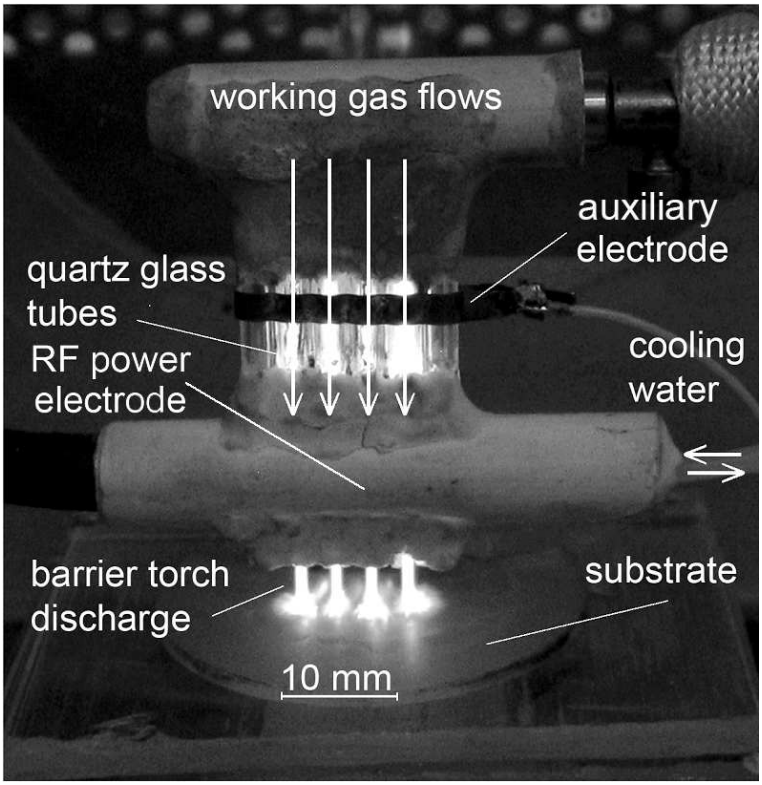

Figure 4.3: Barrier multi torch discharge.

In the barrier multi torch plasma jet system the RF electrode surrounds several pipes, which are arranged in line. This barrier multi torch discharge (photo in Figure 4.3) treats wider substrate area at once and hence relatively large substrate surface can be processed by simple linear movement of the substrate holder. In comparison with the single plasma jet system the multi jet needs, apart from the main RF electrode, a supplementary, auxiliary RF electrode, which is also depicted in Figure 4.3. This electrode helps to ignite the discharge and prevents the discharge from burning in the upstream direction. Our experience shows that combination of the main and auxiliary electrodes results in proper driving the discharge towards the dielectric substrate. Auxiliary electrode is connected with

Substance	State	Purity	Supplier
Titanium Tetraisopropoxide $Ti[(CH_3)_2CHO]_4$	liquid	96 %	Sigma Aldrich
Titanium(IV) diisopropoxidebis (2,2,6,6-tetramethyl-3,5-heptanedionate) $Ti[(CH_3)_6O_2]_2(CH_3)_4O_2$	solid	99.99 %	Sigma Aldrich
Zn-acetylacetonate $Zn[C_5H_7O_2]_2$	solid	95 %	Merck
Al-acetylacetonate $Al[C_5H_7O_2]_3$	solid	98 %	Merck

Table 4.1: Used precursors.

the main RF electrode via 737 Ω resistor. Glass pipes and the main RF electrode are cooled down by the (closed circuit) flow of distilled water. The RF electrode is connected with the RF power generator with a frequency 13.56 MHz via the matching unit. The RF power was square-wave modulated by pulses from pulse generator with the repetition frequency 10 - 20 Hz (repetition period 50 - 100ms). The length t_a of the active part of the cycle was 5 ms (duty cycle 1:19 at 10 Hz). The absorbed power in the discharge in the burning phase of the cycle was 37 W.

4.3 Gases, precursors, substrates

Precursors used for the thin film deposition are shown in Table 4.1. They were placed in the heated containers and transferred into the plasma zone with help of working gases. The mixture of He+N_2 was used to transfer precursor through the main channel and if higher amount of He was needed the mixture was flown through the auxiliary channel.

Mixture of helium and nitrogen gases was fed into the nozzle (for simplicity we describe the single torch case; in the four torch system the arrangement was similar). The distance between nozzles outlet and the substrate was 4-13 mm.

Kind of the film	Precursor	Temperature of the container [°C]	Deposition time [min]	Modulation Frequency [Hz]
TiO_2	$Ti[(CH_3)_6O_2]_2(CH_3)_4O_2$	130-140	5 - 60	30 - 40
TiO_2	$Ti[(CH3)_2CHO]_4$	28 - 30	30 - 60	190
ZnO	$Zn[C_5H_7O_2]_2$	105 - 110	5 - 30	25
$ZnO + Al$	$Zn[C_5H_7O_2]_2$ $Al[C_5H_7O_2]_3$	105 - 110 80 - 84	5 - 30 5 - 30	50 50

Table 4.2: Conditions of the thin films deposition.

The RF barrier torch discharge was generated in the mixture of He + N_2 gases. Precursor was placed in the separate container, kept at electronically stabilized temperature (Table 4.2). In case of doping, the 2nd precursor was placed in the 2nd container. The containers were made by Cova. The stable precursor temperature resulted in stable precursor flow rate (stable He-N_2-precursor flow rate) even if we could not directly measure the precursor flow rate. With increasing the ratio of N_2/He the degree of ionization was also increased. The flow rates were measured and controlled by digital flow controller MKS Instruments type 247. Quartz glass, silicon, Ni, polymer and glass were used as substrates. The temperature on the surface of the substrate during deposition by barrier torch discharge was around 250 °C [135]. Coating of the larger substrate area was provided by motor-driven x-y movement of the grounded Al substrate holder with a water-cooling system.

4.4 Study of barrier torch discharge micro - parameters with help of optical emission spectroscopy during CeO_2 film deposition [90]

The spectra of OH radicals and N_2 molecules were used for characterization of barrier torch discharge micro-parameters (rotational temperature T_r and vibrational temperature T_v). Since all the system has worked at open air and has not been closed in any chamber, nitrogen diffused into the discharge channel. The method is described in detail in chapter 4.1.3.

Water vapour always present in the atmosphere diffused to the discharge channel as well. Just at that region, H_2O molecules were dissociated and excited emitting OH radicals appeared in the discharge channel. In such manner, OH excited emitting radicals and excited emitting N_2 molecules carried information about micro-parameters in the discharge channel. Rotational lines of OH radicals (308 nm, Q branch) were used for calculation of rotational temperature T_r of these molecules. This temperature is usually very close to the temperature of neutral gas in the discharge channel since emitting levels of the fine rotational structure are very close together (307.8 - 308.7 nm) as reported in [136]. The neutral gas temperature is an important parameter in understanding the energy balance in plasma processing.

Vibrational temperature T_v was calculated by using the second positive system of N_2 molecule bands (0,3) and (0,2).

Table 4.3 presents rotational and vibrational temperatures calculated by using emission spectra scanned at the RF barrier single torch discharge configuration with a dielectric quartz glass nozzle and the aluminum substrate. This was done during deposition of CeO_2 films. The situation at the substrate surface with

	T_v band (0,2)(K)	T_v band (0,3) (K)	T_r (Q branch) OH (K)
At the outlet of the nozzle	3240	3202	816
At the surface of the substance with aerosol delivery	3089	3286	732
At the surface of the substance without aerosol	3449	3390	698

Table 4.3: Vibrational and rotational temperatures in the barrier single torch plasma during CeO_2 film deposition. Estimated experimental error is ≈12%.

T_r (Q branch) OH (K)	T_v band (0,3) (K)	T_v band (0,2) (K)
423	3865	3821

Table 4.4: Vibrational and rotational temperatures in the barrier multi torch discharge.

and without aerosol precursors is resolved in Table 4.3. Experimental error of rotational and vibrational temperatures was estimated to ≈12 % .

Vibrational temperature T_v can be usually considered close to electron temperature T_e in that kind of atmospheric plasma [88]. It can be seen from Table 4.3 that vibrational temperature is $T_v \approx 3300$ K, independently of the position in the jet and aerosol precursors. This is a relatively high value as compared with rotational temperature and consequently with the temperature of neutral gas, which was around $T_r \approx 800$K at the nozzle outlet and $T_r \approx 700$K at the substrate. It means that the atmospheric discharge channel interacting with the substrate can be considered as low temperature and strongly non-isothermal. This result corresponds to that in [88] where the ratio of the electron and the gas temperatures has been found 4:1 and did not vary significantly with the distance from the electrode.

The gas neutral temperature in the jet in front of the aluminum substrate was

$T_n = 700$ K. It was relatively far from the melting point of aluminum $T_{Al} = 932$ K. Table 4.4 gives rotational and vibrational temperatures calculated from spectra scanned at the nozzle outlet of the barrier multi torch discharge configuration with the quartz glass substrate. Similar to the single jet system, the plasma in the multi jet system is strongly non-isothermal with relatively low neutral gas temperature $T_n \approx 400$ K.

Chapter 5

Results and discussion

5.1 Discharge diagnostic

With evolution of digital technologies a new method for plasma diagnostic has been designed in order to complement the old ones. In the 1992 Laroussi tried to make a photo of the discharge to differentiate between filament and homogeneous discharges (Figure 1.7 [69]). During 15 years the resolution of digital technologies has increased and exposition time has decreased, therefore digital technique for RF plasma with a repetition frequency 20 -40 Hz can be used now.

5.1.1 Video camera optical diagnostic

In the attached paper [A 1.1.] an easy and relatively cheap method of the plasma diagnostic is presented[1]. We have recorded the light intensity of the discharge using the digital video camera Panasonic NV-DS65EG monitor the light intensity of the barrier torch discharge during the active period of the cycle. Evolution of the discharge brightness can give some information about evolution of the discharge. Light emission of barrier torch discharge recorded by a video camera was analyzed on a PC. We have observed the whole visible range without any filters. When the repetition frequency of the discharge was adjusted close to the frame frequency, the video camera has yielded stroboscopic effect. The video camera used has a frame rate 30 frames per second (or 30 Hz). The repetition frequency of BTD was set to 29.975 Hz. Consequently, using stroboscopic effect we could observe the evolution of the discharge brightness during active part of the cycle t_a on the several frames. Because of the difference between the frame rate f_1 and the discharge repetition frequency f_2, every frame taken by the camera is time-shifted by the delay $\tau = 1/f_1 - 1/f_2$ with respect to the start of

[1]This experiment was made by myself from start to finish (idea, preparation of diagnostic equipment, measurements and evaluation of the experimental results.)

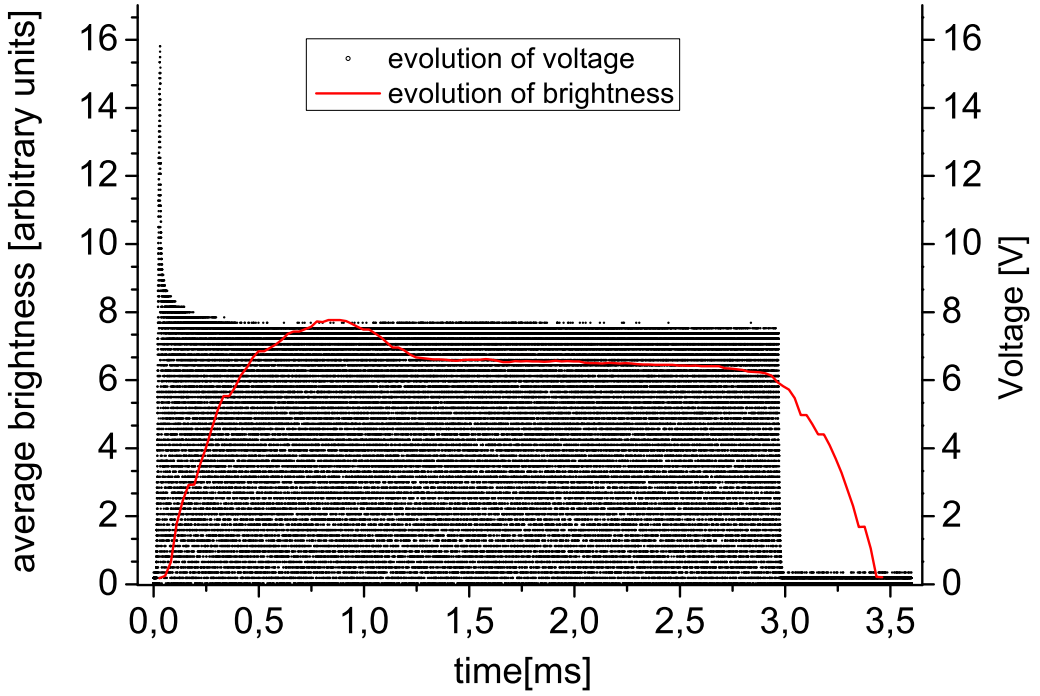

Figure 5.1: Time evolution of the barrier torch discharge brightness and voltage during active impulse.

the discharge impulse. For given frequencies this delay amounts to approximately 28 μs. It means that we can obtain approximately $t_a/\tau \approx 107$ frames during the active part of the discharge period (t_a=3ms). The used exposure times range between 1 - 4 ms (1/250 - 1/1000 s).

In this manner we obtained time evolution of the light intensity from the discharge during the active impulse with fairly good time resolution. A video tape from video camera was edited with help of program Ulead Video Studio. In particular, individual frames from the video tape could be recorded. The background in the recorded frames is sufficiently dark and, hence, we could assume that the vast majority of bright pixels in each digital frame record are produced by

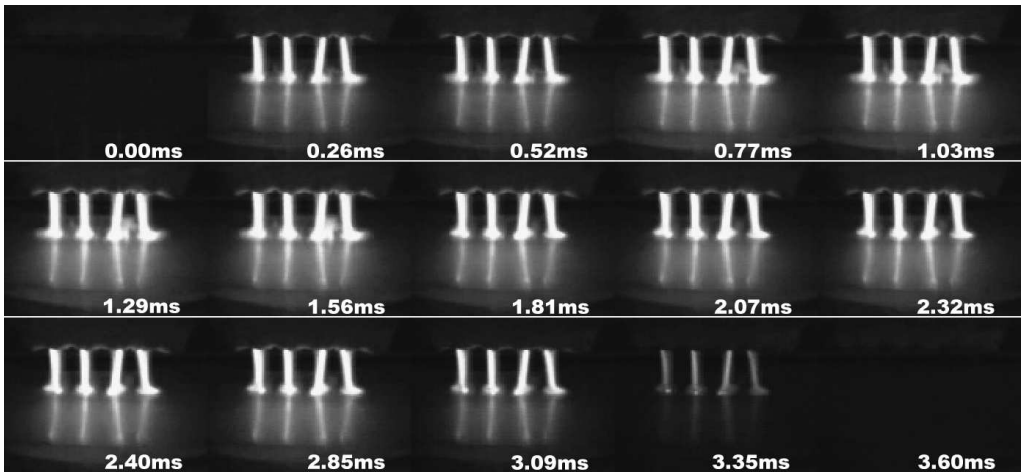

Figure 5.2: Time evolution of barrier torch discharge(quartz glass substrate). Time is counted from the beginning of the RF impulse.

light emitted by burning discharge. In such manner we could study the brightness of the plasma channel(s) on each frame the resulting course of the discharge brightness together with the dependence of the discharge voltage is shown in Figure 5.1.

The analysis of this curve leads to several conclusions:

- The curve reaches maximum approximately one ms after discharge ignition. The ignition happens at the point of the voltage peak (shadowed part of the graph depict the voltage), because the ignition of the discharge needs the elevated voltage.

- The rest of the curve after the voltage has been switched off gives us information about afterglow plasma. The power was switched off after 3 ms and discharge was still visible 0.5 ms afterwards. This fact can be explained by slower diffusion at atmospheric pressure and by the effects of long-lived helium metastables He (2^3S_1) and He (2^1S_0) with lifetimes $6 \cdot 10^{-5}s$ and $2 \cdot 10^{-2}s$ respectively.

- For drawing of Figure 5.1 we have used approximately 125 different impulses. The "sleek " curve shows good reproducibility of the experiment.

In Figure 5.2 we see 15 frames recorded over the discharge active period and some time prior switch-on and after switch-off. In these measurements, the duration of the discharge impulse is 3 ms and the time length of the records depicted in Figure 5.2 is 3.6 ms. The discharge impulse repetition frequency is 29.79 Hz in this case.

5.1.2 Digital photo diagnostic

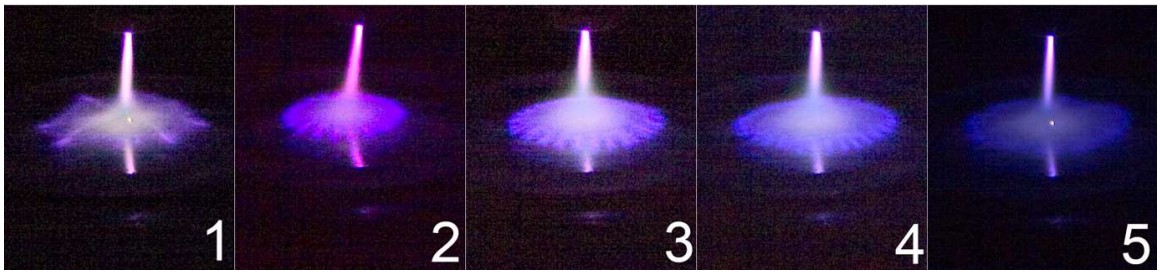

Figure 5.3: Dielectric barrier single torch discharge during deposition on the dielectric substrate (SiO_2), Q_{He}=700sccm, Q_{N2}=15sccm, frequency of the discharge 30 Hz, exposure time 1/800 (1.25 ms).

As it can be seen in paragraph 5.2.2. there are differences in the deposition on the dielectric and conductive substrates.

The digital camera Canon EOS 300D was used to take photos of the barrier torch discharge interacting with the 2 kinds of substrates[2]. The camera was not synchronized with periodic discharge ignition, i.e. the pictures were taken at arbitrary times during active pulse. In Figure 5.3 one can see the shape of the discharge how it forms in interaction with the dielectric substrate. The shape of

[2]This experiment was made by myself from start to finish (idea, preparation of diagnostic equipment, measurements and evaluation of the experimental results.)

the discharge is symmetric. In the photos 1-5 one can observe different numbers of "feet" (more intensive traces within the area of interaction with the substrate). I suppose that the number of "feet", increased during burning evolution, tending to make discharge homogenous. In Figure 5.4 photos of the barrier single torch discharge during deposition on the conductive substrate are presented.

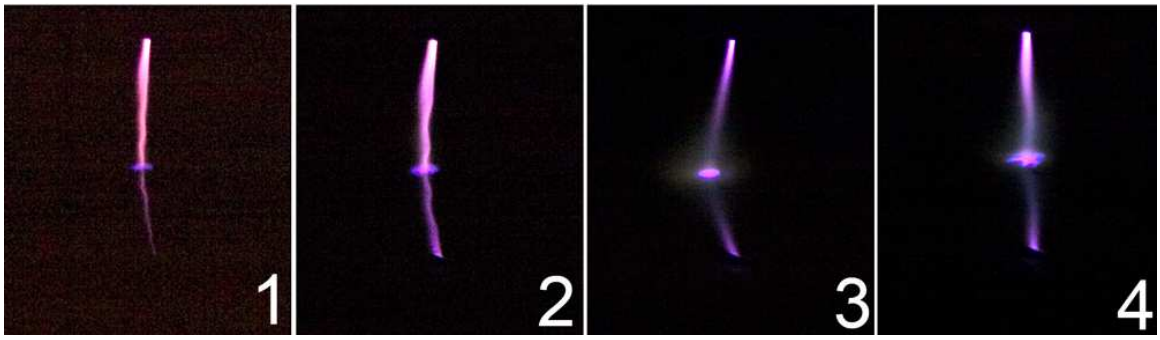

Figure 5.4: Dielectric barrier single torch discharge during deposition on the conductive substrate (Si), Q_{He}=700sccm, Q_{N_2}=15sccm, frequency of the discharge 30 Hz, exposure time 1/800 (1.25 ms).

I suppose that the light patch in the photos 1-4 corresponds to the "stagnation point", i.e. the point at which the stream of plasma interacts with the substrate [137].

5.1.3 Impedance measurement

Method of plasma impedance measurement is described in the attached paper [A 1.2.]. We have used this method for diagnostic of the barrier single and four torch discharge[3] (see paragraph 4.1. and 4.2.). We have used following deposition conditions for single nozzle barrier torch discharge:

- Helium with mass flow Q_{He} = 900 sccm (Q_{He} = 1.5 Pam^3s^{-1}).

[3]In this experiment I collaborated on modification of the experimental system for the impedance measurements, made the measurements and evaluated the results.

As a barrier multi torch system we used arrangement with four nozzles in a row separated by the distance of 4 mm. Experimental conditions were as follow:

- He gas flow with mass flow rate Q_{He}=8000 sccm (Q_{He} = 13.3 Pa·m^3·s^{-1}) was fed into all four nozzles. This optimum magnitude of the He flow rate as well as of other deposition parameters (duty cycle, repetition frequency, precursor temperature, speed of movement of the substrate table) have resulted from many preliminary trial tests.

The following conditions were used for both single and four jet systems:

- The distance between nozzle outlets and the substrate (length of the plasma jet) is 5 mm. That is the largest distance for which we have achieved stable burning of the discharge that is necessary for long-time operation during layer deposition.

- As the growth precursors, vapours of Zn-acetylacetonate $Zn(C_5H_7O_2)_2$ are used for the deposition of ZnO thin films. Temperature of the precursor is 70 °C.

- Bare kapton foil with thickness 0.02 mm, silicon and quartz glass with thickness 1 mm are used as substrates.

- The rectangular-pulse-modulated RF power is used for plasma excitation.

- The length of the whole period is 50 ms (20 Hz repetition frequency). Length of the active part of the period is 5 ms when the RF power is applied on the electrode (duty cycle 1:9).

In the pulse-modulated regime of the RF generator it is impossible to determine the power deposited in the discharge in usual manner. The difference of

readings on the incident and reflected power indicators on the generator cannot be used as the indicators are designed to function with CW mode of generator operation. In order to measure the instant RF power P_{RF} absorbed in the plasma jet during active part of the cycle (average power along the RF period), we attempted to directly measure the instantaneous values of the RF voltage and current by means of digital oscilloscope. In order to do it we attached RF capacitive voltage probe to the metallic RF electrode placed around the nozzles and inserted Rogowski coil as an RF current sensor in current path between the substrate and the grounded holder. This configuration is experimentally beneficial since we measured RF current on the conductor one terminal of which is grounded and consequently the error due to capacitive coupling of RF voltage to sensed current signal is relatively low. Voltage and current sensors are calibrated prior to their installation. RF signals from these calibrated sensors are fed to digital oscilloscope which is able to directly process sampled data. We can then calculate the instant RF power P_{RF} absorbed in the plasma over one RF cycle in active part of the period and the real Z_R and the imaginary Z_{im} parts of the plasma impedance from voltage and current waveforms, see Figure 1.26. A typical example of RF voltage and current waveforms obtained in our system is given in Figure 5.5. In this measurement, the power deposited in the discharge during the active impulse was 37 W. All the results of plasma impedance measurement and electron concentration n_e estimation presented below, are obtained for quartz glass substrate.

Model of the plasma jet impedance and electron density calculation

We have used the described RF voltage and current monitoring for determination of discharge current density, absorbed RF power and volume power density, real and imaginary part of the plasma impedance and rough estimation of aver-

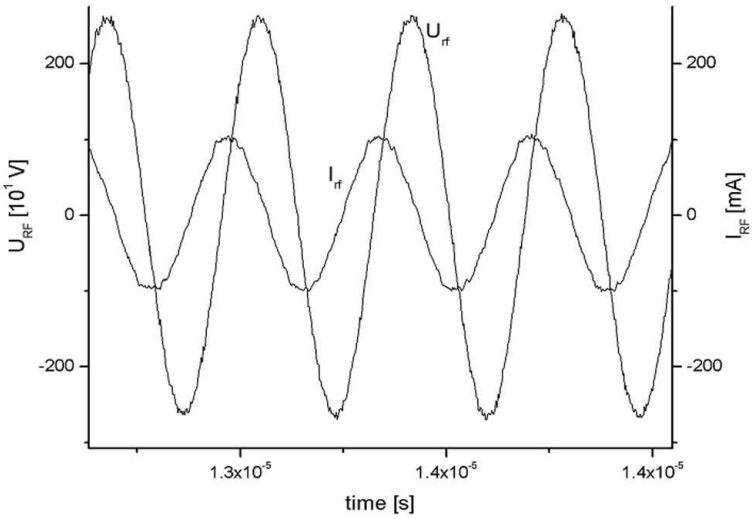

Figure 5.5: Example of RF current and voltage waveform in barrier torch discharge at 37 W Q_{He}= 900 sccm = 1.5 Pa·m^3·s^{-1})
.

age electron concentration in the plasma jet. Similar measurements were done also before in different RF atmospheric- and moderate-pressure plasma systems as presented, for example, in [138] and [139]. We considered our single and multi jet systems as series connection of two capacitors and ohmic resistor similarly as it was considered for different RF high-pressure plasma systems with planar electrodes [138, 139]. Capacitors included dielectric wall of quartz nozzles, dielectric substrate and thin plasma sheaths at the walls. More correctly, parasitic capacitance between the nozzle and the substrate should have been considered as well. It could have certain influence on obtained Z_R from our measurement (and hence on the plasma density value). For the sake of simplicity, however, we neglected this parasitic capacitance. Consequently, it could be considered that the real part of obtained impedance Z_R exhibits ohmic resistance of the plasma jet column. Since the excitation frequency of RF generator $\omega = 2\pi f << \nu$, where ν is the collision frequency of electrons with heavy particles, we can write

for electron concentration n_e [139]:

$$n_e = \frac{d}{eAZ_R\mu_e} \tag{5.1}$$

In Equation (5.1) d is the length of the resistive plasma jet column (distance between nozzle end and substrate), e electron charge, A cross section of plasma jet, Z_R the real part of the single plasma jet column impedance and $\mu_e = 1.1310^{-1}m^2/(Vs)$ is electron mobility in He at atmospheric pressure 10^5 Pa. It was reported in [138] that the thickness of electrode sheath in He atmospheric RF discharges is in the range $\sim 2-20\mu m$. It is negligible in comparison with our distance between nozzle outlet and the substrate. For this reason, the distance $d = 5$ mm can be considered in Equation (5.1) for both cases of barrier single and multi torch discharges. For calculation of current density, volume power density and n_e in our system, we assume that the plasma jets are always cylinders with diameter D=2 mm and height d=5 mm.

Voltage amplitude U_m, power P_{RF} and real and imaginary parts of plasma column impedance Z_R, Z_{IM} are plotted in dependence on RF discharge current amplitude I_m for barrier single and four torch discharges in Figures 5.6 and 5.7, respectively. In the results presented in Figures 5.6 and 5.7 we varied the power deposited in the discharge in the active part of the period by "tuning"/"distuning" of the matching unit. It can be seen that in both plasma jet systems P_{RF} increases with I_m in similar manner as the RF voltage amplitude U_m on the driving electrode. Z_R seems to be practically independent on I_m in single plasma jet system. Z_R in multi-jet system has maximum for $I_m = 250$ mA but for all investigated I_m remains in the interval 1000-1400 Ω. It can be seen that Z_R in multi-jet is approximately four times lower than in the single jet system. If we consider the multi-jet as a parallel connection of four single jets, we can see that

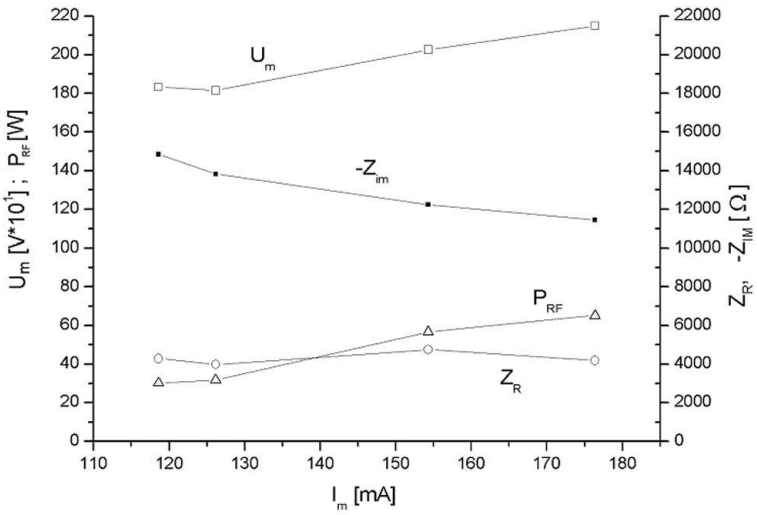

Figure 5.6: Dependence of electrical parameters on discharge RF current amplitude I_m in barrier single torch discharge (Q_{He}= 900 sccm = 1.5 Pa·m^3·s^{-1}).

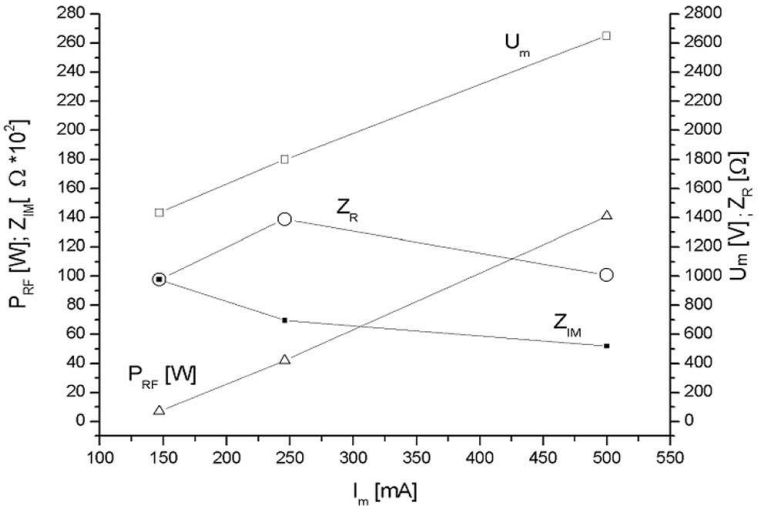

Figure 5.7: Dependence of electrical parameters on discharge RF current amplitude I_m in barrier four torch discharge (Q_{He}= 900 sccm = 1.5 Pa·m^3·s^{-1}).

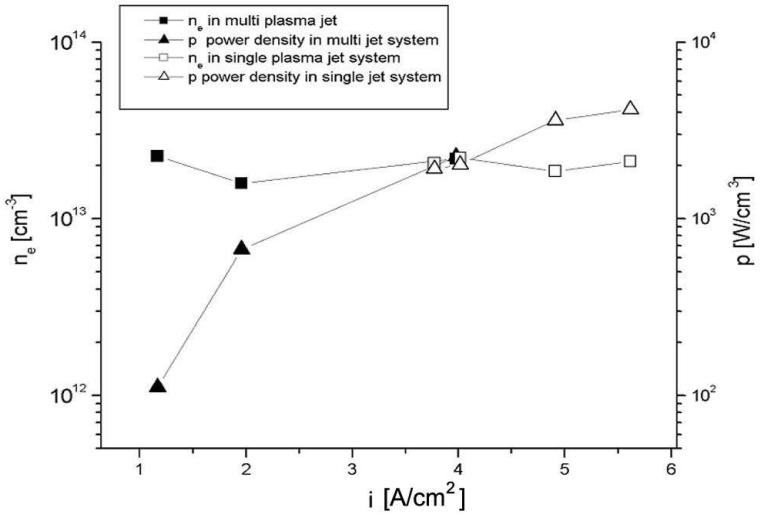

Figure 5.8: Dependence of measured electron concentration n_e and RF power density p on RF current density i both barrier single and four torch discharges.

Z_R recalculated on single channel was always in the interval 4000-5200 Ω for both cases of multi and single jet system. The consequences of this phenomenon can be seen from the Figure 5.8. Electron concentration n_e is calculated according formula (5.1) and is depicted in Figure 5.8 in dependence on the RF discharge current density i. The figure shows that n_e is relatively stable in magnitude $n_e \approx 2 * 10^{13} cm^{-3}$. We suppose that n_e calculated here is only a rough estimate of some average value in the plasma jet. Our presumptions used for n_e calculation were based on approximation and simplification of the real situation. Also, we can see in Figure 5.8 the dependence of volume RF power density p on RF discharge current density i for both single and multi-jet system. It is seen that n_e seems to be relatively independent on current density. On the other hand, the volume power density p grows rapidly with i. Despite that our obtained discharge current density, volume power density and n_e seem to be very high, similar values of these parameters were obtained in the planar RF atmospheric discharges in He gas as it was reported by different authors [138]. It appeared from these measurements

that it is beneficial to use pulse modulation during deposition of the films on kapton substrate in order to avoid the substrate being overloaded by deposited RF power and, thus, overheated.

5.1.4 Optical emission spectroscopy

Measurement of electron concentration with help of H_β line broadening

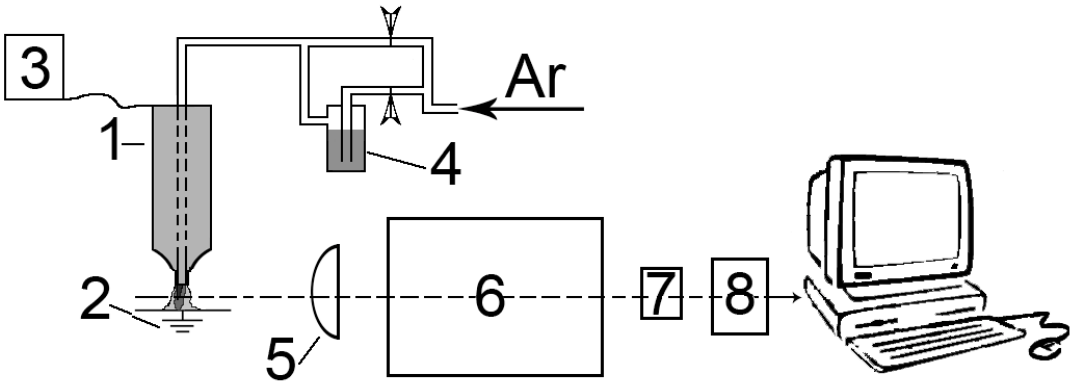

Figure 5.9: Scheme of the spectroscopic measurements of the electron concentration in the plasma jet at atmospheric pressure. (1) metal nozzle, (2) grounded electrode, (3) power generator, (4) humidifier, (5) lens system, (6) spectrograph, (7) multiplier, (8) amplifier.

Theoretical description of the measurement of electron concentration with a help of H_β spectral line is presented in the paragraph 1.3.3. In the papers [A 1.3.] and [A 2.5.] the first results of the electron density estimation by means of the spectroscopic measurements at atmospheric pressure in Ar are presented[4]. The electron concentration as an important parameter of the plasma is estimated from the H_β line broadening. For the n_e calculation we adopted the simple relation between the Stark broadening of the H_β line $\triangle\lambda^{Stark}(H_\beta)$ and n_e exploited already in [105]:

[4]In this experiment I collaborated on modification of the experimental system for the electron concentration measurements, made the measurements and evaluated the results.

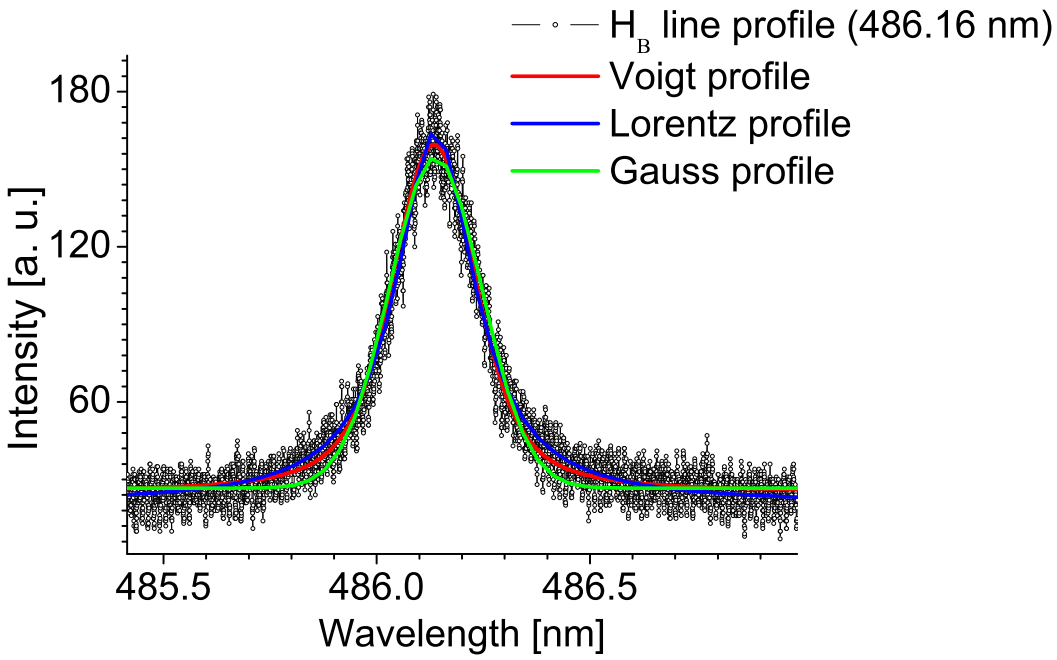

Figure 5.10: Experimental H_β line profile (486.13 nm) and its approximation by the Voigt, Gauss and Lorentz profiles.

$$n_e = 10^{16} \cdot [\triangle\lambda^{Stark}(H_\beta)]^{1.55} \tag{5.2}$$

where $\triangle\lambda^{Stark}(H_\beta)$ is in nm and n_e in cm^{-3}.

In our case the profile of an emission line can be mostly affected by two broadening mechanisms: Stark (collisional) and instrumental (paragraph 1.3.3.). In Figure 5.9, the main parts of the experimental setup used are depicted. These are power generator (3), Ar gas supply, humidifier (4), lens system (5), spectrograph (6) and PC computer.

In the preliminary experiments described here, we have powered the discharge by a DC source using the power range 125-200 W. Small amount of water vapour is admixed to the Ar working gas by means of humidifier. Ar gas mass flow rate is

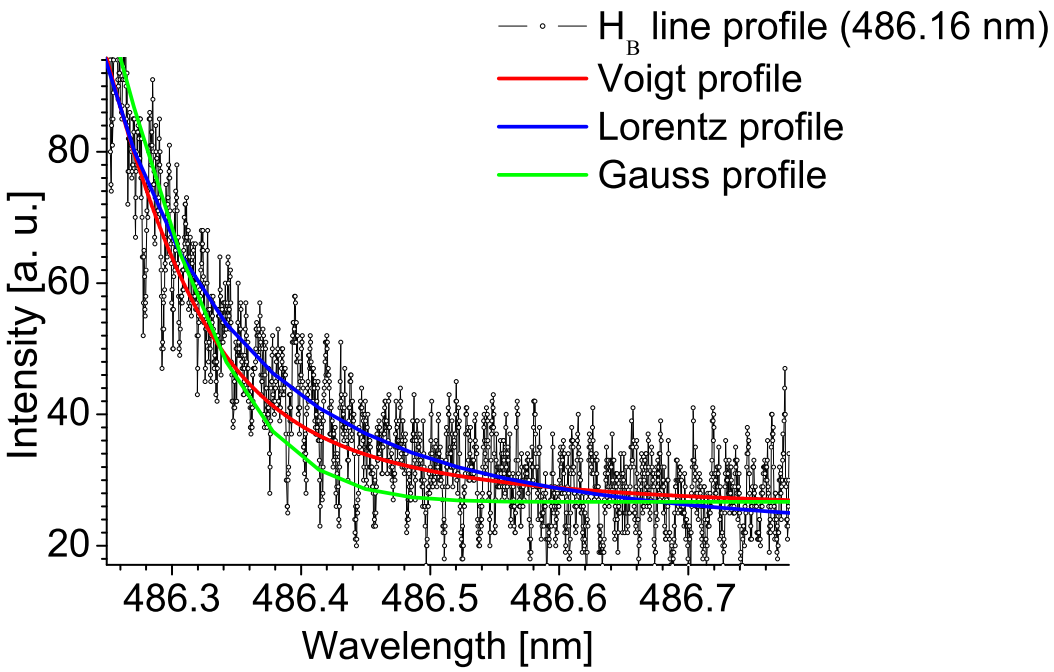

Figure 5.11: Comparison of the three different profiles in wing of measured H_β spectral line (Gauss profile - instrumental function, Lorentz profile - Stark collision broadening and Voigt profile - convolution of Lorentz and Gauss profile)

Q_{Ar} = 700 sccm = 1.2 $Pa{\cdot}m^3{\cdot}s^{-1}$ and that of mixture of Ar+H_2O Q_{Ar+H_2O} = 300 sccm = 0.5 $Pa \cdot m^3 \cdot s^{-1}$. It is the optimal flow rate (Ar+H_2O). Using lower flow rate results in low signal-to-noise the barrier torch discharge spectrum. For higher flow rate the discharge does not burn.

Metal nozzle (1) with inner diameter 1.4 mm and outer diameter 6 mm and grounded metal plate were used as electrodes. Distance between the metal nozzle and the grounded electrode (2) varied in the range 3-6 mm. To measure the H_β spectral line profile (Figure 5.10), the light emitted by plasma jet is focused onto entrance slit of the spectrograph (SPM2, 1200 grooves/mm) by means of a lens system (5).

The width of the entrance slit of the spectrograph was 10 μm. The H_β spectral

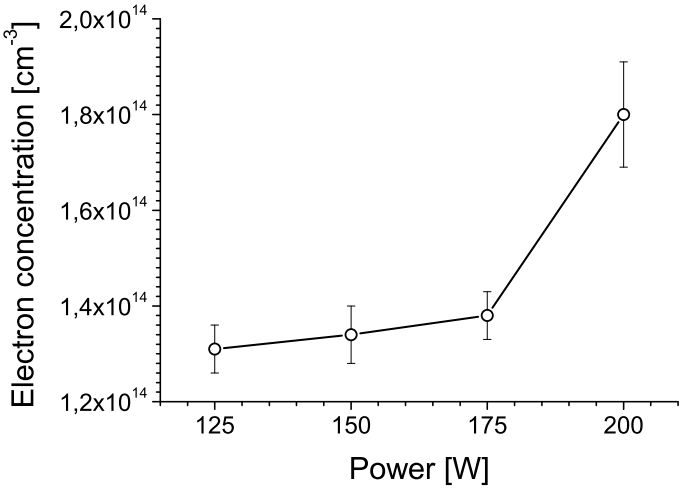

Figure 5.12: Dependence of the electron concentration in Ar plasma jet at atmospheric pressure on the power supplied into the plasma.

line was fitted by Voigt profile. To eliminate the instrumental broadening we used the profile of Hg spectral line (435.8 nm) as an instrumental function. This spectral line is fitted by Gauss profile. For comparison of the accuracy, how all these there profiles (Lorentz, Gauss and Voigt) approximate the measured H_β line profile, we have depicted them together with the experimental data in Figures 5.10 and 5.11. As we have noted (paragraph 1.3.3.), the convolution of Lorentz and Gauss profiles is Voigt profile. By using the de-convolution method we can obtain the Lorentz profile and estimate the Stark broadening. Equation (5.2) is used for calculation of electron concentration n_e.

The measurements are reproducible within approximately 6 % error limit. The measured electron densities range around 10^{14}cm^{-3}. It is observed that the plasma density increases with increasing of the power supplied into the plasma (see Figure 5.12).

Measurements of the H_β spectral profile in atmospheric plasma jet with He as working gas did not give satisfactory results so far. The most probable reason

lies in smaller electrons density in comparison to Ar at similar deposited power [140] and consequently in too low H_β line Stark broadening. This method has the low limit of sensibility n_e around $10^{13} cm^{-3}$. The electron concentration estimated with the help of impedance measurement (paragraph 5.1.3.) is $2*10^{13} cm^{-3}$.

Qualitative analysis of the emission spectra

Using the equipment of Figure 5.9 with He and N_2 as working gases and ceramic tube, we observe emission spectra from barrier torch discharge with very similar conditions to the ones used for deposition. All spectra were recorded perpendicularly to the plasma channel, at different experimental conditions like at different working gas flow, kind of substrate and temperature of the precursor.

Typical spectrum emitted by the plasma channel without precursor with He and N_2 as working gases is shown in Figures 5.13 - 5.15. In these spectra, we observe the N_2 second positive system ($C^3\Pi_u - B^3\Pi_g$) and N_2^+ first negative system ($B^3\Pi_g - A^3\Sigma_u^+$). The He I lines (501.567 nm and 587.562 nm) can be observed as well.

N_2 - emission molecular lines

The nitrogen bands are used to estimate the rotational and vibrational temperatures. The rotational temperature is determined by fitting the spectrum with program LIFBASE in the range 386 nm - 392 nm. This spectral range corresponds to the N_2^+ (0,0) and (1,1) vibrational bands. The best-fit of the spectrum using LIFBASE program yields a rotational temperature of $\sim$ 1200 K. The rotational temperature is close to the gas temperature because rotational relaxation is fast at atmospheric pressure.

Vibrational temperature is usually assumed to be very close to the electron temperature in the discharge plasma. For measurement of this temperature we

λ_h[nm]	$v^{'} - v^{''}$	$p(v^{'} - v^{''})$	$B_{v^{'}} * 10^2$	$B_{v^{''}} * 10^2$	J_h	$E_v[eV]$	$E_r * 10^{-2}$
380.49	0-2	0.1792	1.8149	1.5922	8	0.126	1.261
375.54	1-3	0.2378	1.7933	1.5737	8	0.373	1.245
371.05	2-4	0.1871	1,7964	1.5551	8	0.610	1.228
367.19	3-5	0.1042	1.7404	1.5368	8	0.849	1.208

Table 5.1: Parameters needed for vibrational temperature estimation [141].

Dielectric substrate	Si substrate	stainless steel substrate
3000 ± 300 K	4400 ± 400 K	4300 ± 400 K

Table 5.2: Vibrational temperature of the barrier torch discharge without precursor (different types of the substrates).

used 4 rotational lines of N_2 molecule close to band heads (N_2 380.49 nm (0,2), 375.54 nm (1,3), 371.05 nm (2,4), 367.19nm (3,5)). Calculation of T_v is performed according to the equation [141]:

$$I^{v^{'}}_{J,J+1} = Av_h^4 p(v^{'}, v^{''}) J_h \Delta J exp[-\frac{E^{'}_v + hcB_{v^{'}} J_h(J_h - 1)}{k_B T_v}] \tag{5.3}$$

where A is constant that is the same for all lines in selected band, $I^{v^{'}}_{J,J+1}$ is intensity of rotational line, v_h^4 wave number, E_v is vibrational excitation energy, E_r is rotational excitation energy ($E_r = hcB_{v^{'}} J_h(J_h - 1)$) , $p(v^{'}, v^{''})$ is vibrational transition probability, J_h is head of vibrational belt, ΔJ is number of the non-resolved spectral lines and k_B is a Boltzmann constant. Parameters needed for estimation of vibrational temperature via N_2 molecular lines are listed in the Table 5.1. Using the above equation the vibrational temperature can be calculated from the slope of a Boltzmann plot of $ln(I^{v^{'}}_{J,J+1}/Av_h^4 p(v^{'}, v^{''}) J_h \Delta J)$ versus $-\frac{E^{'}_v + hcB_{v^{'}} J_h(J_h - 1)}{k_B T_v}$.

Vibrational temperatures of the barrier torch discharge without precursor for different deposition conditions are presented in Table 5.2.

As it can been seen in the Table 5.2 the type of the substrate influences the

vibrational temperature: $T_v \sim 3000$ K on the dielectric (quartz glass) substrate, $T_v \sim 4400$ K on the conductive substrate (Si) and $T_v \sim 4300$ K on the stainless steel substrate.

In Figures 5.16 - 5.18 emission spectra of the barrier torch discharge spectra in working gases He and N_2 with precursor Ti-thd are presented. N_2 (second positive system), N_2^+ (first negative system) and He spectral lines can be observed as well. Note that new spectral lines appear in the spectrum.

CN - molecular lines emission

In the emission spectra of barrier torch discharge with Ti-thd precursor the CN **violet** system ($B^2\Sigma^+ - X^2\Sigma^+$) is observed. The violet system of CN is strongly excited by carbon arcs in air, by the reaction of active nitrogen with variety of organic vapours, and by combustion processes [142]. The violet systems are also prominent in emission in the spectra of comets and in absorption in the spectra of R - and N - type stars [5]. The strong bands of the CN violet system lie on a narrow and diagonally oriented Condon locus [6] in well defined sequences.

CN molecule was created in the barrier torch discharge from precursor molecule Ti-thd ($Ti[(CH_3)_6O_2]_2(CH_3)_4$) and nitrogen molecule (N_2).

CN molecular lines were used to calculate rotational temperature. This calculation was performed with help of program LIFBASE. The best fit of the experimental spectrum of CN spectral lines is presented in Figure 5.19. We see that even the best-fit does not approximate the measured lines fully. This is probably caused by the fact that CN arises due to chemical reaction in plasma

[5] R - and N - type stars - these are also known as 'carbon stars'. These are red giants, near the end of their lives, in which there is an excess of carbon in the atmosphere.

[6] Condon [143] predicted the expected locus of strong bands on the v', v" plane by classical mechanics and the correspondence principle. For simple harmonic oscillator potentials he predicted a quadratic relationship between v' and v" which can be compared with the position of observed strong bands on the Deslandres diagram. The well-known primary Condon 'parabola' which often pass through (0,0) and are roughly symmetric about v' = v" were thus confirmed.

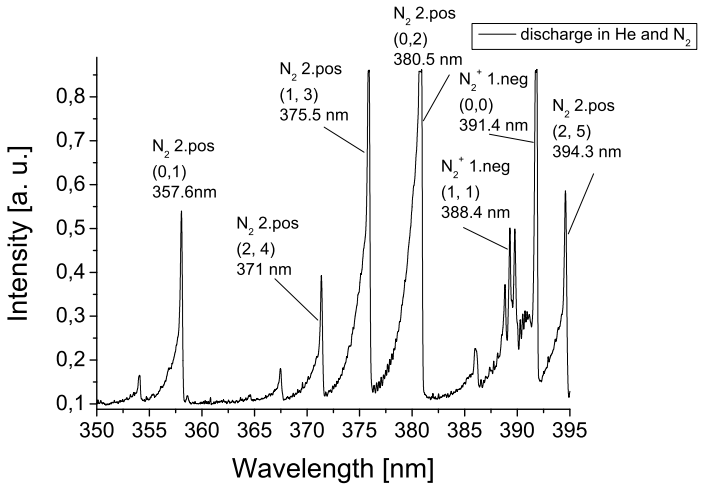

Figure 5.13: Emission spectra of the barrier torch discharge without precursor, within 350-395nm wavelength range. He and N_2 were used as working gases.

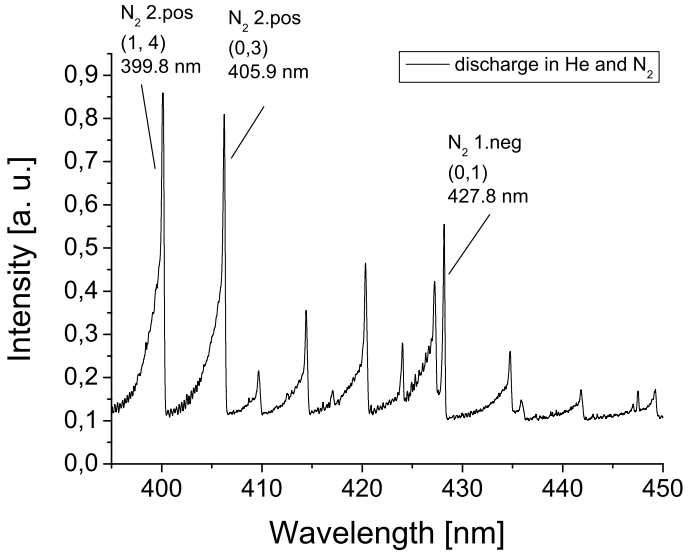

Figure 5.14: Emission spectra of the barrier torch discharge without precursor, within 395-459nm wavelength range. He and N_2 were used as working gases.

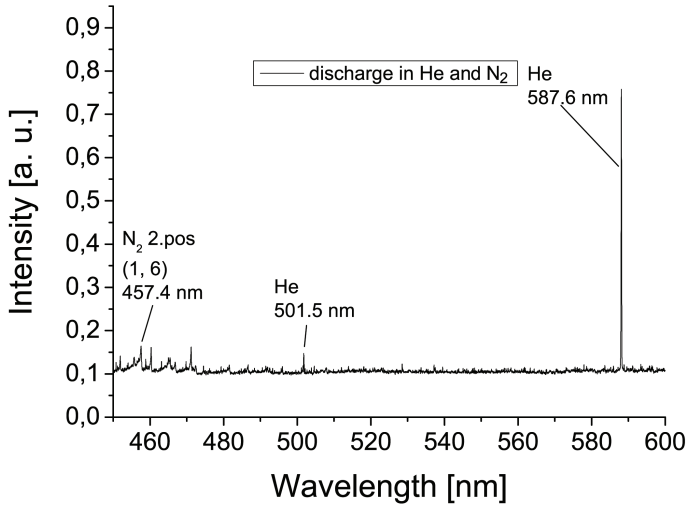

Figure 5.15: Emission spectra of the barrier torch discharge without precursor, within 450-600nm wavelength range. He and N_2 were used as working gases.

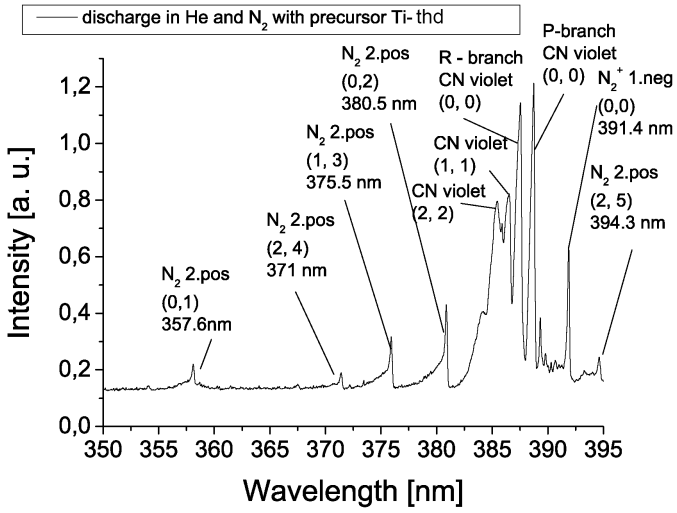

Figure 5.16: Emission spectra of the barrier torch discharge with Ti-thd precursor, within 350-395nm wavelength range. He and N_2 were used as working gases.

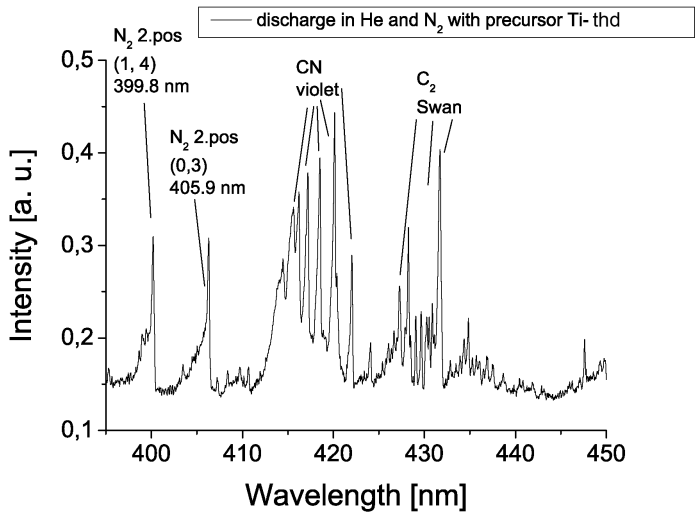

Figure 5.17: Emission spectra of the barrier torch discharge with Ti-thd precursor, within 395-450nm wavelength range. He and N_2 were used as working gases.

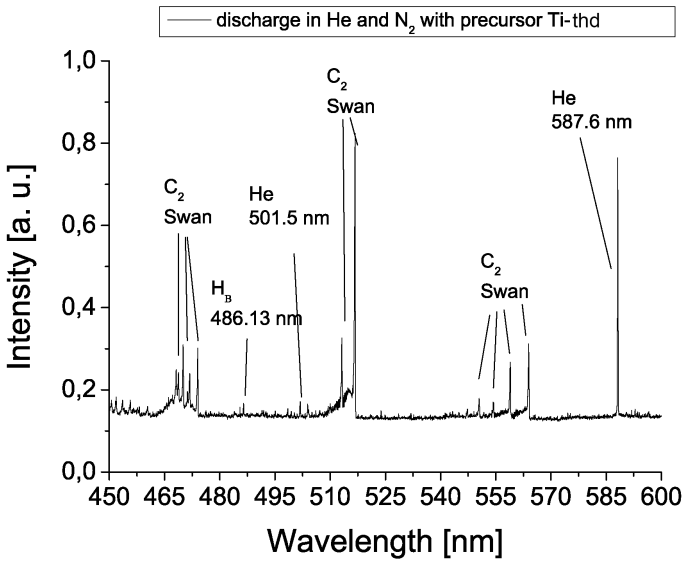

Figure 5.18: Emission spectra of the barrier torch discharge with Ti-thd precursor, within 450-600nm wavelength range. He and N_2 were used as working gases.

volume. That causes deviation for thermal equilibrium among the heavy particles in plasma and consequently the presumption on which the LIFBASE program operates is not fulfilled. The rotational temperature for all samples was $\sim 950\ K$. Differences in the results of calculations of the rotational temperature N_2^+ and CN lines can be explained by the error of rotational temperature estimation, especially in the case of N_2^+ spectral lines.

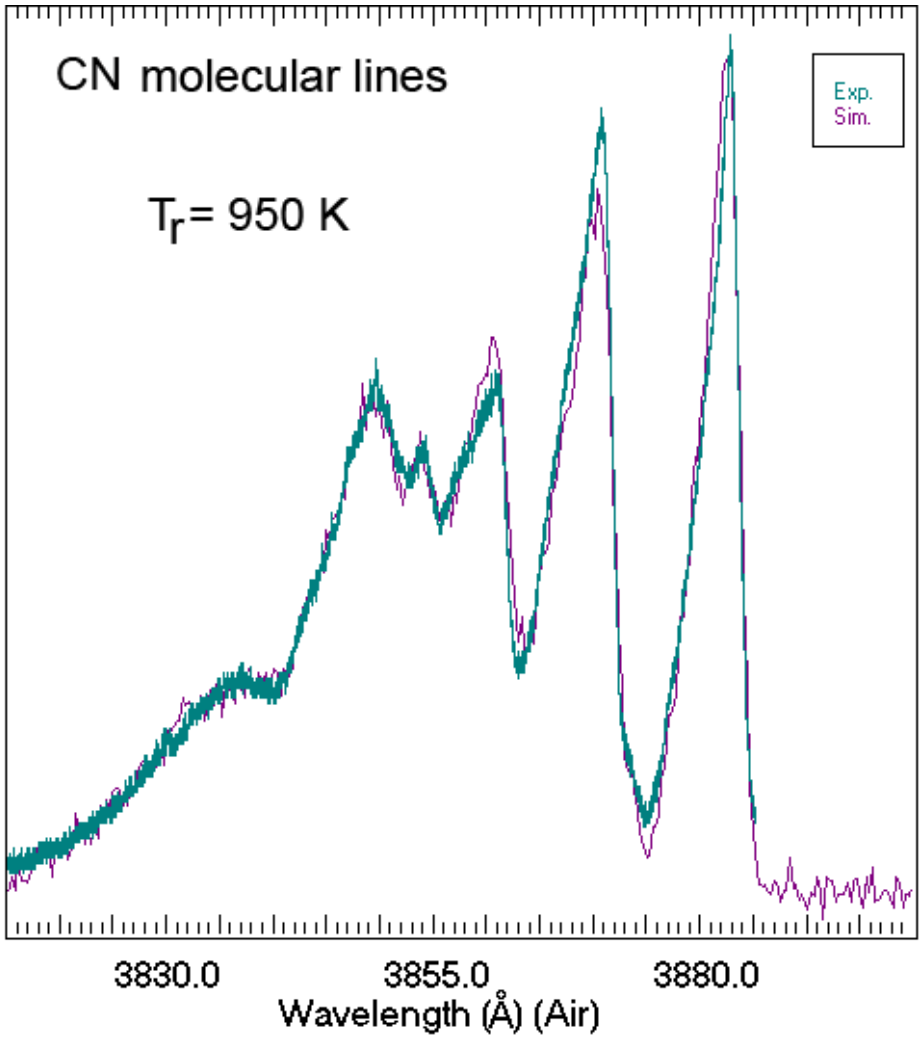

Figure 5.19: The best-fit of CN (violet) molecular line in the range 380-388.5 nm.

Estimation on the rotational temperature with a help of N_2^+ spectral line is

T_{Ti-thd}=433°K	T_{Ti-thd}=443°K	T_{Ti-thd}=423°K
3000-3500 °K	2800-3000 °K	2700-3000 °K

Table 5.3: Vibrational temperature of the barrier torch discharge (different precursor temperature) Q_{He}=700sccm, $Q_{He+Ti-thd}$=100sccm.

not possible in the case of using precursor Ti-thd (see paragraph 4.3), because appearance of CN (violet) molecular lines coincides with the N_2^+ molecular lines. Also lines Ti I (388.02 and 388.289 nm) do not allow to fit N_2^+ molecular lines of barrier discharge even without using precursor. Ti I (388.02 nm) is very intensive line and Ti I (388.289 nm) is abnormally wide line, so I suppose that for observation of these lines just trace amount of Ti in the plasma zone is needed. The source of Ti could be a nozzle, because during deposition with precursor, thin films are created in the inner of the nozzle.

The vibrational temperature of the discharge with Ti-thd precursor has been determined in similar manner like in case of the discharge without precursor, i. e. for the N_2 lines using Equation (4.3). The obtained vibrational temperature are tabulated in Table 5.3 for different precursor temperatures. The flow rate does not influence the vibrational temperature, which changes with flow rate in the range of about 50 K; it corresponds roughly to error of the measurements $\sim 12\%$.

C_2 - molecular lines emission

The C_2 molecules possess seven known triplet and six known singlet electronic states giving rise to nine band system, which lies across the vacuum ultraviolet, the visible and the infrared spectral regions [144]. The strongest and most easily excited of these band systems is the **Swan system** that lies between 420 - 770 nm [145].

In a re-assessment and systematization of the energy level scheme and nomenclature for the C_2 molecule, [144] we assign the notation ($d^3\Pi_g - a^3\Pi_u$) for

the Swan system instead of the previously used notations ($A^3\Pi_g - X^3\Pi_u$) and ($A^3\Pi_g - X^{`3}\Pi_u$). Potential curves for the C_2 system are shown in Figure 5.20 [146].

The Swan band system is an important spectroscopic feature of many different types of sources ([147], [148] etc). It is the same as CN molecules observed in the emission spectra from the heads of comets [149] and in the absorption spectra of R - and N - type stars [150].

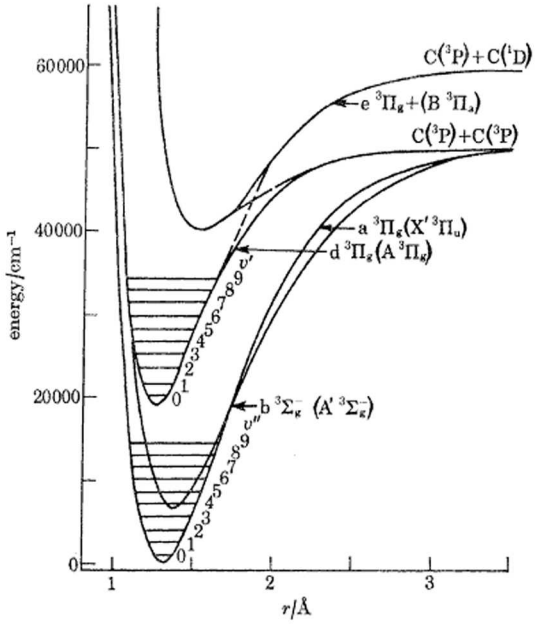

Figure 5.20: Potential curves for the C_2 Swan system ($d^3\Pi_g a^3\Pi_u$) appropriate to Klein - Dunham potentials [151]. New [144] and old (in brackets) notation is indicated for each electronic state.

5.2 Thin films properties

5.2.1 ZnO thin films

Optimal deposition conditions

In the paper [A 2.6.] optimal parameters of ZnO:Al thin films deposition barrier single torch discharge are presented[7].

We had to determine the optimal parameters of the deposition process for successful deposition of thin films. In Figures 5.21 - 5.24 we demonstrate selected results. In case of ZnO thin films, we need to have polycrystal (see the paragraph Crystal structure of ZnO this films), i. e. not amorphous structure to observe conductivity of these films. Properties of ZnO films depend on the temperature of precursor, flow rate of working gases, etc.

The dependence of the deposition rate on the temperature of the precursor vapours in case of ZnO films is shown in Figure 5.21. The dependence features a maximum at around 110 °C

As we noted, the temperature of the precursor determines the quantity of the chemical elements first in the plasma zone and next in the film. For creating the right stoichiometric and conductive ZnO structure, it is important to keep the ratio of the deposition area on the substrate and the quantity of precursor vapours constant. The deposition area is the place of the contact between the plasma jet and the substrate. Dependence of the deposition rate on the N_2 gas (which carries the precursor) flow rate can be seen in Figure 5.22. The flow rate of the gas determines the time spent by the precursor particles in the plasma and in the downstream (afterglow) zone. In the plasma zone the excitation and other

[7]In this experiment I carry out the deposition, made the measurements of conductivity by Van der Pauw method and evaluated the results.

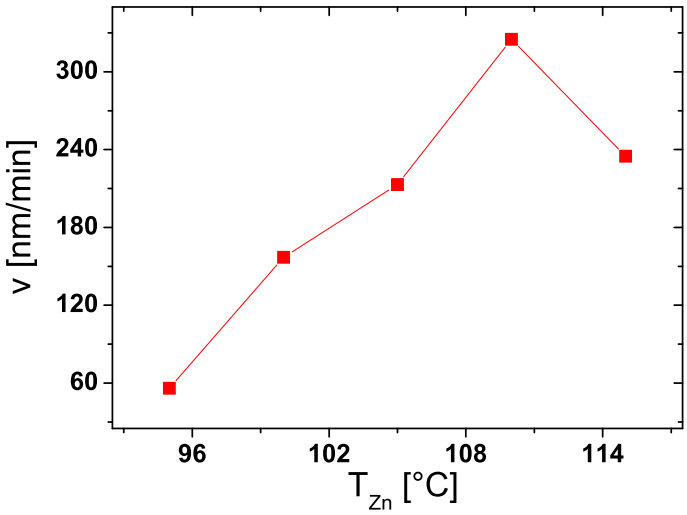

Figure 5.21: Dependence of the deposition rate of the ZnO thin films on the temperature $T_{Zn}$of the vapours of the growth precursor ($Q_{N_2/He}$ = 400/400 sccm, distance nozzle-substrate d = 6 mm), cc.

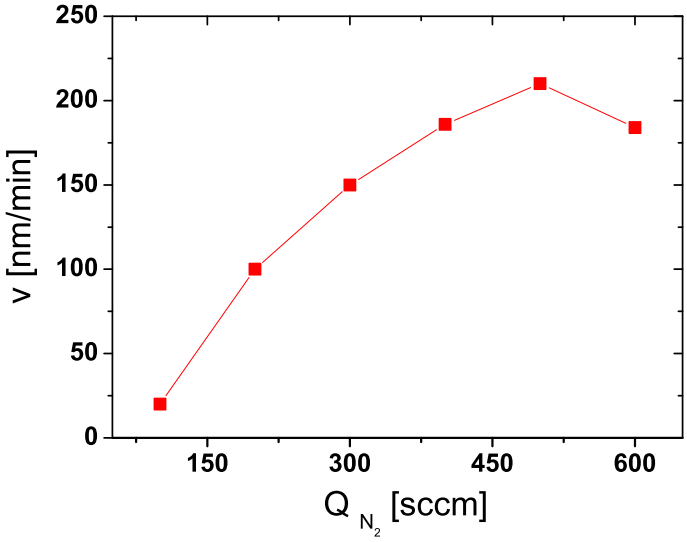

Figure 5.22: Dependence of the deposition rate of the ZnO thin films on the N_2 flow rate T_{Zn}= 105°C, d = 6 mm, deposition time 5 min.

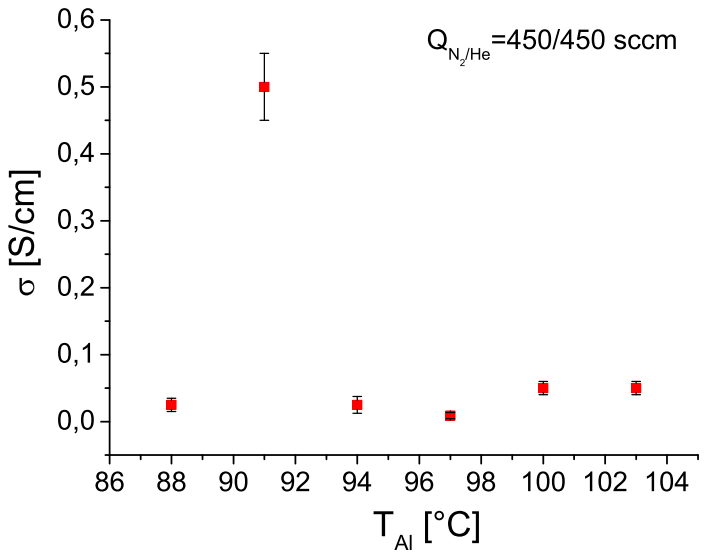

Figure 5.23: Dependence of the conductivity σ on the temperature of the accessory precursor (T_{Zn}= 105°C, d = 6 mm, deposition time 3 min).

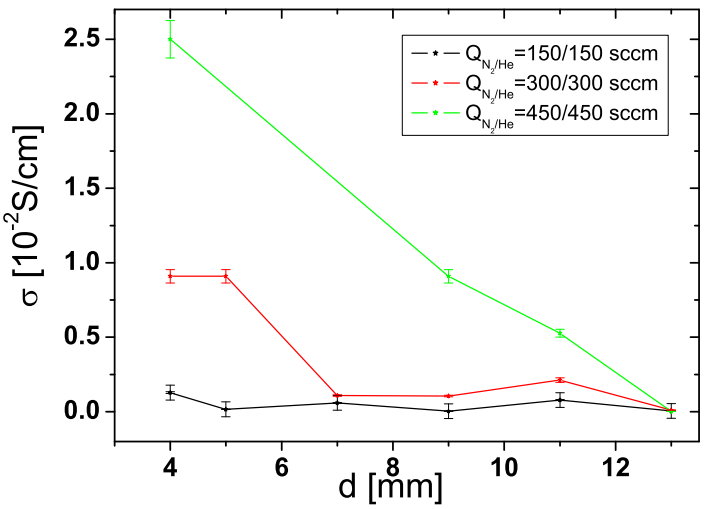

Figure 5.24: Dependence of the conductivity σ on the distance between nozzle outlet and the substrate (T_{Zn}= 105°C, T_{Al}= 91°C, deposition time 3 min).

TCO films	Doping elements
SnO_2	Sb, F, As, Nb, Ta
In_2O_3	Sn, Ge, Mo, F, Ti, Zr, Hf, Nb, Ta, W, Te
ZnO	Al, Ga, B, In, Y, Sc, F, V, Si, Ge, Ti, Zr, Hf
CdO	In, Sn
ZnO - Sn_2	Zn_2SnO_4, $ZnSnO_3$
ZnO - In_2O_3	$Zn_2In_2O_5$, $Zn_3In_2O_6$
In_2O_3 - SnO_2	$In_4Sn_3O_{12}$
CdO - SnO_2	Cd_2SnO_4, $CdSnO_3$
CdO - In_2O_3	$CdIn_2O_4$
$MgIn_2O_4$ $GaInO_3$, $(GaIn)_2O_3$	 Sn, Ge
$CdSb_2O_6$	Y
ZnO - In_2O_3 - SnO_3	$Zn_2In_2O_5$ - $In_4Sn_3O_{12}$
CdO - In_2O_3 - SnO_2 ZnO - CdO - In_2O_3 - SnO_3	 $CdIn_2O_4$ - Cd_2SnO_4

Table 5.4: TCO semiconductors for creating the transparent electrodes.

volume processes can occur. In afterglow zone the particles become inactivated. It is evident that there must exist an optimal flow rate: in case of very low flow rate the particles become inactivated before landing on the substrate, in case of too high flow rate the particles do not have enough time to become excited. Indeed, we see in Figure 5.22 a maximum of the deposition rate at Q_{N_2} around 460 sccm. Similar qualitative explanation holds also for dependence in Figure 5.21.

We can improve conductivity of thin films by doping with other elements. The doping elements can be seen in the Table 5.4. In our case, we have used Al-doping. Using the Van der Pauw four-point method (paragraph 2.2.3.) [133] we have performed measurements of the conductivity of the deposited ZnO:Al thin films in dependence on the deposition conditions (precursor temperature, distance from the plasma jet to the substrate, gas flow rate etc.). The goal was to achieve the maximum conductivity of the deposited ZnO:Al layer. The temperature of the

container with the accessory precursor (Al-acetylacetonate) was used to change the quantity (flow rate) of the accessory precursors in the plasma zone and hence to affect the conductivity of the deposited ZnO films as shown in Figure 5.23. The peak of the film conductivity at the accessory precursor temperature 91°C can be seen in Figure 5.23. We have repeatedly obtained almost the same comparatively high conductivity around 0.5 S/cm at the same conditions but, unfortunately, not always. The reasoning for the dependence with a maximum is similar as explained above.

Distance between nozzle outlets and the substrate (Figure 5.24) affected the length of the downstream (afterglow) zone, i. e. the path, which active particles should pass within the limited time. If this distance is too short the temperature of the substrate increases and thermal damages of the substrate could be observed. If this distance is too long the particles have enough time to become deactivated. Also, increasing the plasma zone length too much could stop burning of the discharge.

Morphology of the ZnO thin film

Morphology of thin films can be regarded as a characteristic of the thin film structure[8]. By studying morphology we determine e.g. the size of thin film patterns - grains or so-called roughness or waveness (high/low frequency part of the variation of the film thickness over distance). One of the methods for studying the thin film morphology is the AFM described in section 3.2.1.

In Figures 5.25 - 5.28 the AFM records showing the morphology of the deposited ZnO thin films are presented. The roughness of the ZnO thin film is around 15nm. In these Figures we can see the strongly shaped grains. The grain

[8]In this experiment I carry out the deposition of thin films.

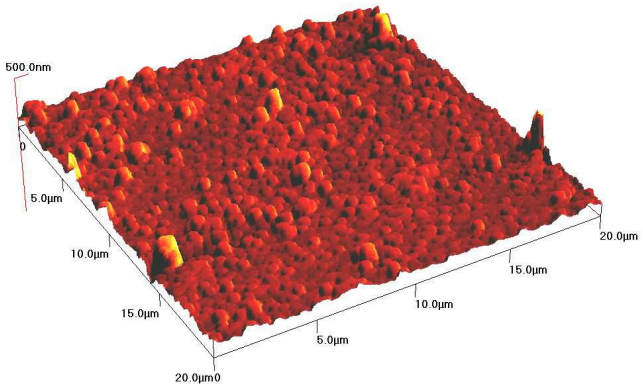

Figure 5.25: AFM record of ZnO thin film scanned area 20x20 μm.

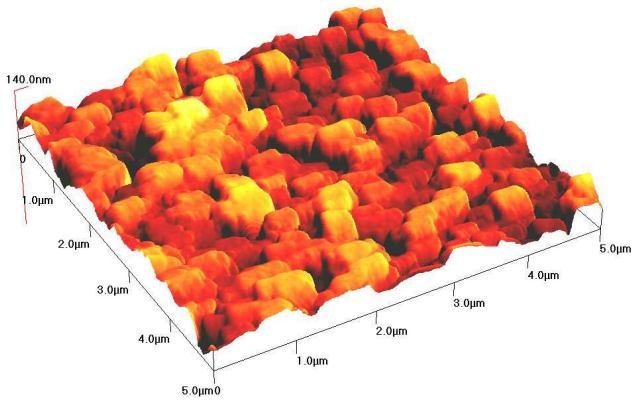

Figure 5.26: AFM record of ZnO thin film scanned area 5x5 μm.

size is around 400 nm. The same data could be visualized by software in two different views: 2D and 3D.

Unfortunately we could not affect the grain size using deposition conditions yet. In case of low-pressure plasma jet deposition the size of the grains has been successfully affected by the working pressure. Since our equipment functions only at atmospheric pressure, we could not use this parameter for layer morphology

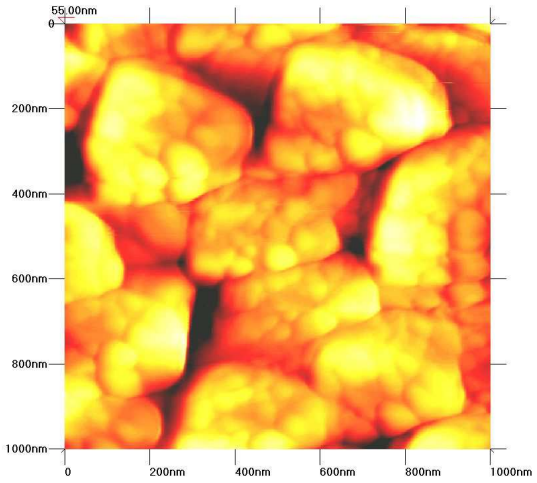

Figure 5.27: AFM record of ZnO thin film scanned area 1x1 μm.

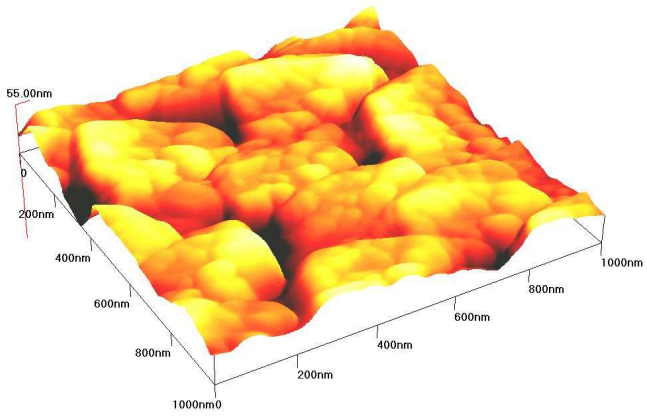

Figure 5.28: AFM record of ZnO thin film scanned area 1x1 μm.

optimization.

Crystal structure of ZnO thin films

The samples deposited on quartz glass and kapton were investigated by XRD in Bragg-Brentano (BB) geometry, see Figure 5.29 [A 2.2.][9]. The sloped part of the top line on the left in Figure 5.29 is due to very thin amorphous substrate (ZnO

[9]In this experiment I carry out the deposition of thin films.

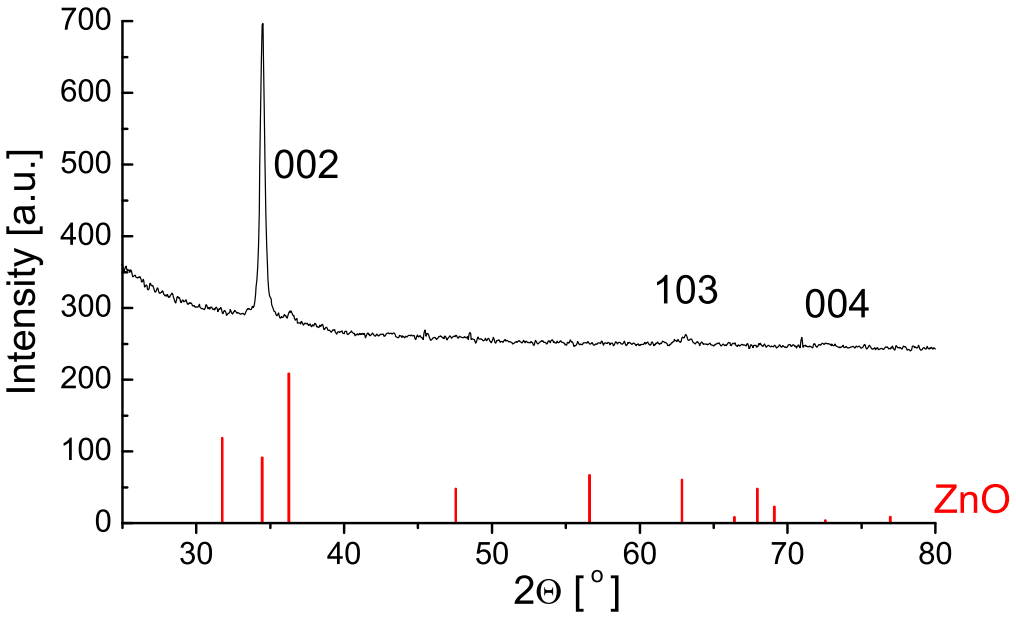

Figure 5.29: XRD patterns of ZnO thin films deposited on kapton foil (quartz glass substrate, T_{Zn}=105 °C, t=3 min).

layer on kapton foil), which results in a low signal-to-noise ratio of the method: the XRD signal from the layer is burden with unwanted background from the plastic substrate. It can be seen from Figure 5.29 that hexagonal crystallites have preferred orientation with 'c' axis perpendicular to the substrate surface. This structure **002** (texture) is named "hairlike structure". This structure is normally created during warming or mechanical treatment, it is characteristic for hexagonal crystallites and is affected by plasma deposition.

5.2.2 TiO_2 thin films

Morphology of the TiO_2 thin films

Morphology of TiO_2 thin films can suggest the size of the thin films patterns (grains) and the roughness [A 2.6.]. The morphology of TiO_2 thin films has also been investigated with help of AFM method (paragraph 2.2.1.)[10]. In Figure 5.30 the discontinuities (voids) are observed. This can be explained by the fact that the precursor Titan-izopropoxide was in the liquid state placed in the containers with electronically controlled temperature (see paragraph 4.3.). During evaporation small drops of liquid titan-izopropoxide were probably transported into plasma zone. These drops could not be activated during short residence time in the plasma zone and have landed on the substrate without good adhesion with substrate.

This problem was later resolved using precursor (Ti-thd) in the solid state (Figures 5.32 and 5.33).

[10]In this experiment I carry out the deposition of thin films.

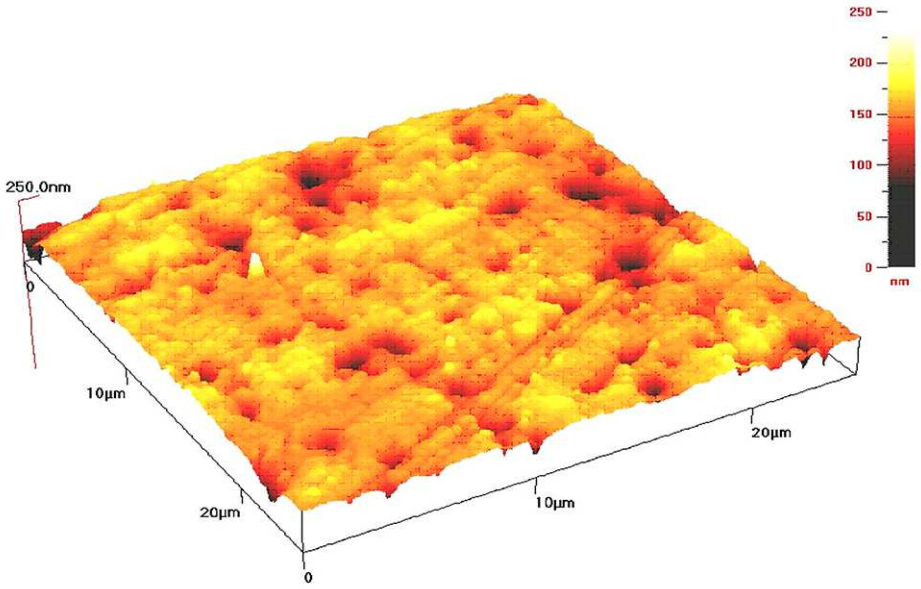

Figure 5.30: AFM image of TiO_2 thin film (precursor Ti-izopropoxide).

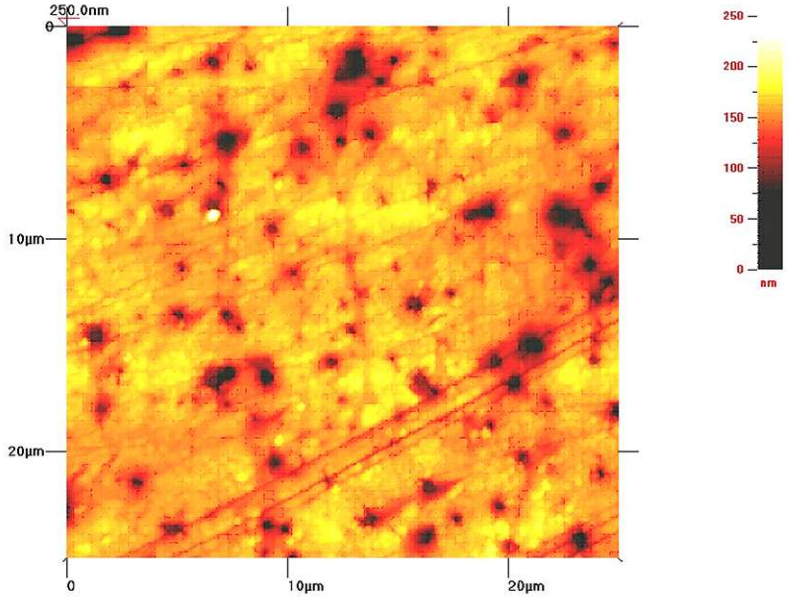

Figure 5.31: AFM image of TiO_2 thin film (precursor Ti-izopropoxide).

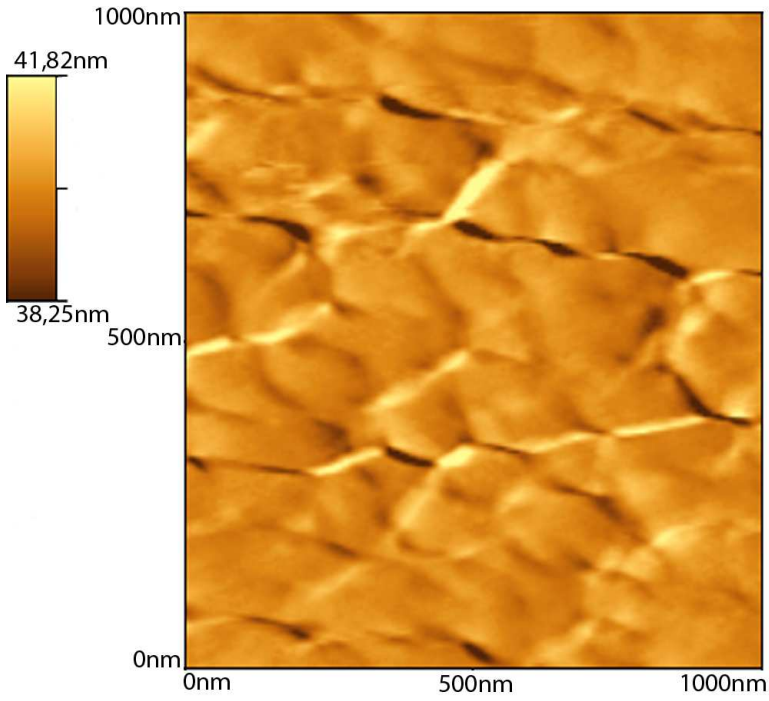

Figure 5.32: AFM image of TiO_2 thin film (precursor Ti-thd).

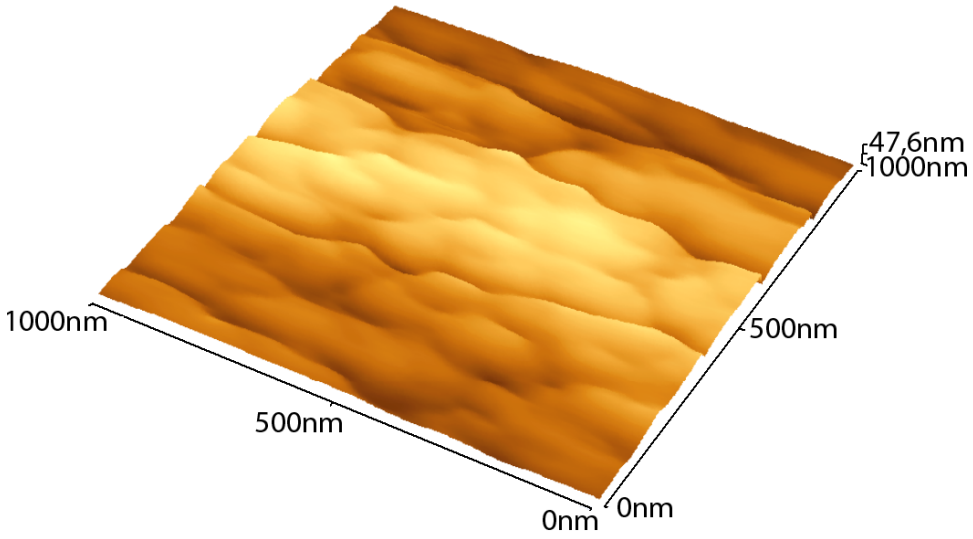

Figure 5.33: AFM image of TiO_2 thin film (precursor Ti-thd).

Crystal structure of TiO_2 thin films

In similar manner as with ZnO, the X-Ray Diffraction analysis was used[11]. For this analysis several samples of TiO_2 thin films were prepared with the same deposition conditions [A 2.3.]. Quartz glass was used as the substrate. The substrate was water-cooled during the deposition, i. e. the substrate temperature was kept at 25 °C during deposition.

Post-deposition annealing with temperature 300 - 550°C for 2 hours was applied. Post-deposition annealing at high temperature is required to produce the amorphous - Anatase transformation (see paragraph 2.1.1.). X-Ray Diffraction analysis showed that only the Anatase (see paragraph 5.2.2.) crystalline phase was present in all films deposited at room temperature. Moreover, with increasing the annealing temperature the amount of Anatase phase increased, see Figure 5.34. The sloped part of the XRD spectra at lower Bragg angles is the effect of the amorphous substrate. In other deposition methods, which we found in literature [152, 153, 154], mixtures of different TiO_2 phases or only the Rutile phase were found. In addition, while in the other titanium oxide deposition procedures the TiO_2 layers without annealing usually contain solely amorphous titanium dioxide, the deposition using barrier torch discharge yields substantial amount of Anatase phase already at room temperature. The width of the XRD peak contains information about size of the crystal. In case of our TiO_2 samples, it is relatively small crystal size, but this is only rough estimation.

To study relationship between the substrate cooling and the crystal structure, we performed another experiment. We used the same deposition conditions, but the substrate cooling was switched off. In Figure 5.35 we can see both Anatase and Rutile phases. It is clear that there are only traces of Rutile phase and the

[11] In this experiment I carry out the deposition of thin films.

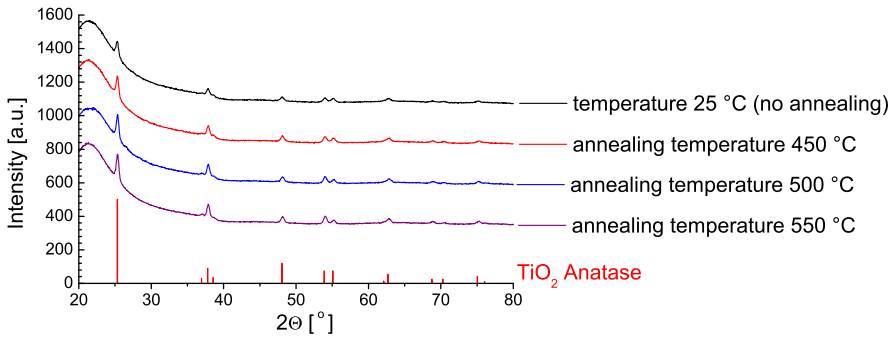

Figure 5.34: XRD patterns of TiO_2 thin films deposited on the quartz glass substrate using cooling system (precursor Ti-izopropoxide, temperature of the precursor 35 °C, deposition time 5 min).

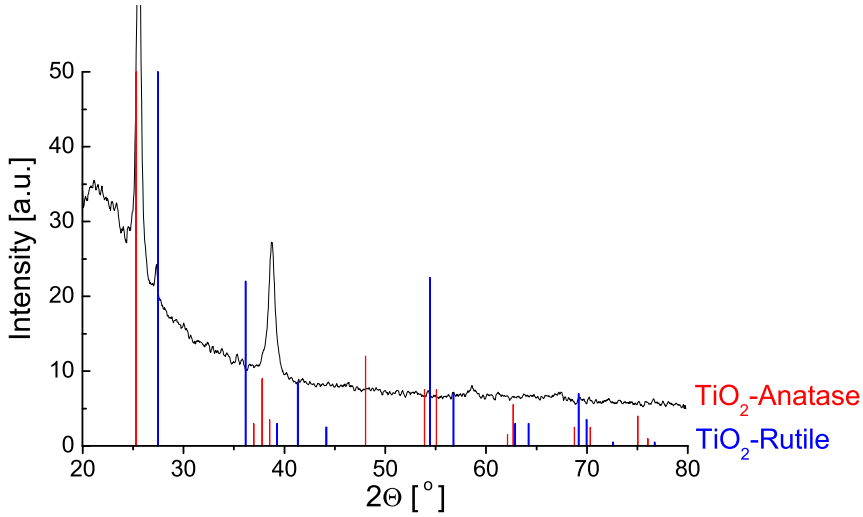

Figure 5.35: XRD patterns of TiO_2 thin films deposited on the quartz glass substrate without cooling system (precursor Ti-izopropoxide, temperature of the precursor 35 °C, deposition time 5 min).

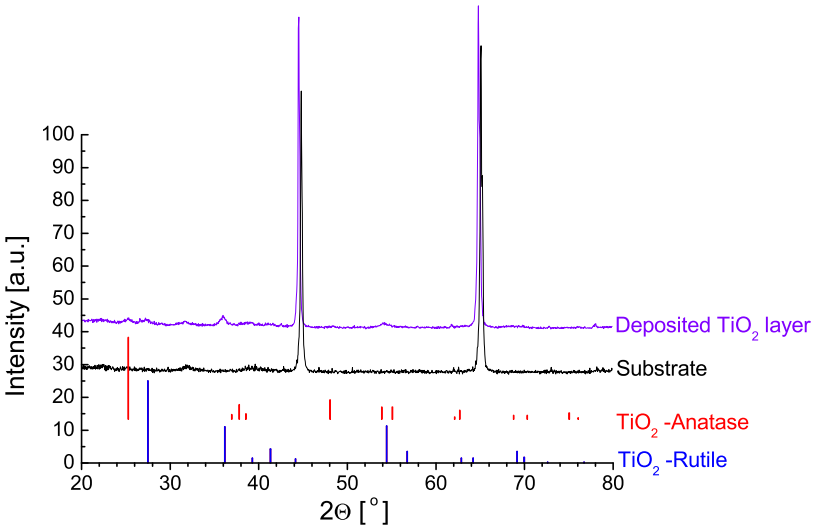

Figure 5.36: XRD patterns of TiO_2 thin films deposited on the stainless steel substrate without cooling system (precursor Ti-izopropoxide, temperature of the precursor 35 °C, deposition time 5 min).

majority of the film consists of Anatase phase. And the crystal size is smaller than in case of water-cooled substrate.

In the next step the TiO_2 thin films were deposited on stainless steel substrates. Also both phases were presented in the film, but only in trace amounts (Figure 5.36). This fact suggests majority of amorphous phase in the deposited TiO_2 film. The possible explanation is that the reaction of the plasma with the substrate is too fast that the crystal phase does not have enough time for creating.

Chapter 6

Conclusion

In my PhD thesis I attempted to present overview of the atmospheric pressure barrier torch discharge and its application. I tried to find answers to the following questions:

- How does the discharge start to burn?
- What happens during deposition?
- What plasma parameters we use?
- What molecules are created in the plasma zone?
- How can we affect thin films by deposition conditions?
- What structure (texture) do the deposited thin films have?
- What is the role of the certain type of substrate?

Emission spectroscopy and impedance measurement lead to comparable results: electron concentration n_e was in the range 10^{13}-10^{14} cm $^{-3}$. Possibility of He metastable existence was demonstrated with help of the video-camera diagnostic. N_2, C_2, CN molecules were identified in emission spectra. Ti, He, H atoms were identified as well. Formation of CN molecule from N_2 and Ti-izopropoxide indicated chemical reaction in plasma volume. Because of this heavy particles reaction plasma is not in thermal equilibrium. This conclusion is supported by the fact that it is not possible to create 100% fit of CN (violet) molecular line with a help of LIFBASE program.

Only one Ti and no TiO spectral lines were identified. Ti spectral lines were probably overlapped by N_2, N_2^+ or CN molecular lines. Main TiO molecular lines radiate in the IR region, which was not covered by our spectrometer.

Optimal deposition parameters were found for successful deposition of conductive ZnO and ZnO:Al thin films. The maximal achieved conductivity of the ZnO:Al was around 0.5 S/cm. The influence of deposition parameters on the electrical conductivity of the layers has not been sufficiently cleared yet. Consequently, further experiments are needed.

XRD analysis has shown that not only deposition conditions but also the type of the substrate play an important role in case of TiO_2 thin films. Conductive substrate accelerates the deposition rate and changes the kinetic of recombination processes on the substrate surface. Only Anatase phase was presented in TiO_2 films. In case of the ZnO thin films, XRD analysis showed 002 texture of these films.

AFM analysis helped us to detect discontinuities in the TiO_2 films and to successfully resolve this problem. AFM analysis showed strongly formed grains of ZnO thin films. Unfortunately we have not been able to affect the size of the grains in the barrier torch discharge yet.

Continuation of experimental work will take place in our laboratory. We plan for example to study the catalytic activity of TiO_2 and to attempt the deposition of BSTO films.

Appendix A

Publication list

A.1 Articles in refereed scientific journals with IF

1. **Chichina M.**, Churpita O., Hubička Z., Tichý M., Holdová M., Virostko P., **Investigation of Atmospheric Pressure Plasma-Jet System Used For Deposition of ZnO Thin Films**, Acta Physica Slovaca, 55 (5), 429-434, 2005. *See Appendix B.*

2. **Chichina M.**, Hubička Z., Churpita O., Tichý M., **Measurement of the parameters of atmospheric-pressure barrier-torch discharge**, Plasma Processes and Polymers, 501-506, 2005. *See Appendix B.*

3. **Chichina M.**, Tichý M., Kudrna P., Grinevich A., Churpita O., Hubička Z., Kment S., Olejníček J., **A study of barrier torch plasma jet system at atmospheric pressure**, Czech. J. Phys. Suppl. B, 56, B1212-B1217, 2006. *See Appendix B.*

A.2 Contributions in conference proceedings

1. **Chichina M.**, Tichý M., Hubička Z., Churpita O., Holdová M., Behnke J. F., Atmospheric Pressure Discharges and Their Applications, in WDS'04 Proceedings of contributed papers: Part II - Physics of Plasmas and Ionized Media, ed. by J. Šafránková, Matfyzpress, 310-315, 2004.

2. Hubička Z., Čada M., Churpita O., Virostko P., Adámek P., Šichova H., Šicha M., Jastrabik L., Tichý M., Holdová M., Olejníček J., **Chichina M.**, Low pressure and atmospheric pressure plasma-jet systems and their application for deposition of thin films, in E proceedings of the 12th International

Congress on Plasma Physics, ed. by T. Hutter, http://hal.ccsd.cnrs.fr/ccsd-00002042.

3. **Chichina M.**, Churpita O., Hubička Z., Tichý M., A Study of the Barrier Torch Discharge Applied for the Thin Film Deposition, in WDS'05 Proceedings of contributed papers: Part II - Physics of Plasmas and Ionized Media, ed. by J. Šafránková, Matfyzpress, 325-331, 2005.

4. Virostko, P., Hubička Z., Olejníček J., Čada M., Adámek P., Šícha M., Tichý M., **Chichina M.**, Study of the Low-Pressure RF Hollow Cathode Plasma Jet During Deposition of $Ba_xSr_{1+x}TiO_3$ Thin Films, Proc. 17th International Symposium on Plasma Chemistry, 491-492 abstract (2 pages) and full-paper (6 pages), 2005.

5. **Chichina M.**, Kudrna P., Tichý M., Grinevich A., Churpita O., Hubička Z., Kment S., Olejníček J., Measurements of the plasma parameters in RF torch discharge used for deposition of oxide thin films, in WDS'06 Proceedings of contributed papers: Part II - Physics of Plasmas and Ionized Media, ed. by J. Šafránková and J. Pavlu, Matfyzpress, 108-113, 2006.

6. **Chichina M.**, Churpita O., Hubička Z., Kment S., Tichý M., A study of ZnO and ZnO:Al thin films deposited by RF plasma jet at atmospheric pressure, in ICPP'06 Proceedings contributed papers CD, paper D120, CD - D120p.pdf, 1-4, 2006.

7. **Chichina M.**, Straňák V., Churpita O., Kment S., Hubička Z., Tichỳ M., Špatenka P., Deposition of Thin TiOx Layers Using Plasma Sources of Jet Types, Proc. 16th Symposium on Application Plasma Processes, 139-140, 2007.

A.3 Presentations on international conferences

1. **Chichina M.**, Behnke J. F., Hubička Z., Churpita O., Holdová M., Tichý M., Atmospheric Pressure Discharges and Their Applications, WDS '04, Prague, Czech Republic, June 15-18, 2004.

2. **Chichina M.**, Hubička Z., Churpita A., Tichý M., Behnke J. F., Measurement of the parameters of atmospheric-pressure barrier discharge, 16th International Vacuum Congress, Venice, Italy, June 28 - July 2, 2004.

3. **Chichina M.**, Churpita O., Hubička Z., Tichý M., A Study of the Barrier Torch Discharge Applied for the Thin Film Deposition, WDS'05, Prague, Czech Republic, June 7-10, 2005.

4. **Chichina M.**, Churpita O., Hubička Z., Tichý M., Holdová M., Virostko P., Investigation of Atmospheric Pressure Plasma-Jet System Used for Deposition of ZnO Thin Films, 15th Symposium on Applications of Plasma Processes and 3rd EU-Japan Joint Symposium on Plasma Processing, Podbanske, Slovakia, January 15 - 20, 2005.

5. **Chichina M.**, Churpita O., Hubička Z., Kment S., Tichý M., A study of ZnO and ZnO:Al thin films deposited by RF plasma jet at atmospheric pressure, 13th International Congress on Plasma Physics, Kiev, Ukraine, May 22-26, 2006.

6. **Chichina M.**, Churpita O., Hubička Z., Kment S., Tichý M., A Study of the Properties of ZnO Thin Films Deposited by RF Single Plasma Jet System at Atmospheric Pressure, WDS'06, Prague, Czech Republic, June 6-9, 2006.

7. **Chichina M.**, Tichý M., Kudrna P., Grinevich A., Churpita O., Hubička Z., Kment S., Olejníček J., A study of barrier torch plasma jet system at atmospheric pressure, 22nd Symposium on Plasma Physics and Technology, Prague, Czech Republic, June 26-29, 2006.

8. **Chichina M.**, Straňák V., Churpita O., Kment S., Hubička Z., Tichý M., Špatenka P., Deposition of Thin TiOx Layers Using Plasma Sources of Jet Types, 16th Symposium on Application Plasma Processes, Podbanske, Slovakia, January 20 - 25, 2007.

A.4 International cooperation

1. November - December 2003: Institute of Physics, Ernst Moritz Arndt University, Greifswald, Germany.

2. August 2006: Institute of Physics, Ernst Moritz Arndt University, Greifswald, Germany.

Appendix B

Attached publications

Acta Physica Slovaca, 55 (5), 429-434, 2005.

Investigation of Atmospheric Pressure Plasma-Jet System Used For Deposition of ZnO Thin Films

Chichina M., Tichý M.

Charles University in Prague, Faculty of Mathematics and Physics,
Department of Electronics and Vacuum Physics, V Holešovičkách 2,
180 00 Praha 8, Czech Republic

Churpita O., Hubička Z., Holdová M., Virostko P.

Institute of Physics, Division of Optics, Academy of Sciences of the Czech Republic,
Na slovance 2, 182 21 Prague 8, Czech Republic

Plasma Processes and Polymers, 501-506, 2005.

Measurement of the parameters of atmospheric-pressure barrier-torch discharge

Chichina M., Tichý M.

Charles University in Prague, Faculty of Mathematics and Physics,

Department of Electronics and Vacuum Physics, V Holešovičkách 2,

180 00 Praha 8, Czech Republic

Hubička Z., Churpita O.

Institute of Physics, Division of Optics, Academy of Sciences of the Czech Republic,

Na slovance 2, 182 21 Prague 8, Czech Republic

Czech. J. Phys. Suppl. B, 56, B1212-B1217, 2006

A study of barrier torch plasma jet system at atmospheric pressure

Chichina M., Tichý M., Kudrna P., Grinevich A.

Charles University in Prague, Faculty of Mathematics and Physics,
Department of Electronics and Vacuum Physics, V Holešovičkách 2,
180 00 Praha 8, Czech Republic

Churpita O., Hubička Z., Kment S., Olejníček J.

Institute of Physics, Division of Optics, Academy of Sciences of the Czech Republic,
Na slovance 2, 182 21 Prague 8, Czech Republic

Bibliography

[1] Temple-Boyer P., Rossi C., Saint-Etienne E., Scheid E., *J. Vac. Sci. Technol. A*, **16**, 1998.

[2] Babayan S. E., Jeong J. Y., Tu V. J., Park J., Selwyn G. S., Hicks R. F., *Plasma Sources Sci. Technol.*, **7**, 286-288, 1998.

[3] Chen Y., Bagnall D. M., Zhu Z., Sekiuchi T., Park K. T., Hiraga K., Yao T., Shen M. Y., Goto T., *J. Cryst. Growth*, **181**, 165, 1997.

[4] Macleod H.A., *Thin Film Optical Filters* (second ed.), Bristol, 1986.

[5] Moses A. J., *Optical Materials Properties*, Hughes Aircraft Company, 1971.

[6] Siemens W., *Poggendorfs Ann. Phys. Chem.*, **12**, 66-122, 1857.

[7] Kogelschatz U., *Plasma Chem. Plasma Process.*, **23**, 1-46, 2003.

[8] Thenard A., *Compt. Rend.,* **74**, 1280, 1872.

[9] Berthelot M., *Compt. Rend.*, **82**, 1360-6, 1876.

[10] Harries W. L., von Engel A., *Proc. Phys. Soc.*, **B 64**, 916-29, 1951.

[11] Harries W. L., von Engel A., *Proc. Royal Soc.* **A 222**, 490-508, 1954.

[12] El-Bakkal J. M., Loeb L. B. J., *Appl. Phys.*, **33**, 1567-77, 1962.

[13] Buss K., *Arch. Elektrotech.*, **26**, 261-5, 1932.

[14] Klemenc A., Hinterberger H., Hofer H. Z., *Elektrochem.*, **43**, 708-12, 1937.

[15] Suzuki M., Naito Y., *Proc. Jpn. Acad.*, **2**, 469-76, 1952.

[16] Gobrecht H., Meinhardt O., Hein F., *Ber. der Bunsenges. f. phys. Chem.*, **68**, 55-63, 1964.

[17] Bagirov M. A., Nuraliev N. E., Kurbanov M. A., *Sov. Phys.-Tech. Phys.*, **17**, 495-8, 1972.

[18] Kogelschatz U., *Plasma Sources Sci. Technol.*, **11**, 3A, A1-A6, 2002.

[19] Kogelschatz U., Eliasson B., Egli W., *J. Phys. IV (France)*, **7**, C4 47-66, 1997.

[20] Kogelschatz U., Eliasson B., Egli W., *Pure Appl. Chem.*, **71**, 1819-28, 1999.

[21] Wagner H. E., Brandenburg R., Kozlov K. V., Sonnenfeld A., Michel P., Behnke J. F., *Vacuum*, **71**, 417-36, 2003.

[22] Kogelschatz U., *Process Technologies for Water Treatment*, 87-120, 1998.

[23] Samoilovich V. G., Gibalov V. I., Kozlov K. V., Original Russian Edition, *Moscow State University*, 1989.

[24] Eliasson B., Kogelfschatz U., *IEEE Trans. Plasma Sci.*, **19**, 309-22, 1991.

[25] Boyers D. G., Tiller W. A., *Appl. Phys. Lett.*, **41**, 28-30, 1982.

[26] Breazeal W., Flynn K. M., Gwinn E. G., *Phys. Rev. E*, **52**, 1503-15, 1995.

[27] Radehaus C., Dohmen R., Willebrand H., Niedernostheide F. J., Phys. Rev. A, **42**, 7426-46, 1990.

[28] Ammelt E., Schweng D., Purwins H. G., *Phys. Lett. A*, **179**, 348-54, 1993.

[29] Brauer I., Punset C., Purwins H. G., Boeuf J. P., *J. Appl. Phys.*, **85**, 7569-72, 1999.

[30] Muller I., Punset C., Ammelt E., Purwins H. G., Boeuf J. P., *IEEE Trans. Plasma Sci.*, **27**, 20-1, 1999.

[31] Muller I., Ammelt E., Purwins H. G., *Phys. Rev. Lett.*, **82**, 3428-31, 1999.

[32] Kogoma M., Okazaki S., Tanaka K., Inomata T., *Proc. 6th Int. Symp. on High Pressure Low Temperature Plasma Chemistry (HAKONE VI)*, 83-87, 1998.

[33] Bartnikas R., *IEEE Trans. Electr. Insul.*, **6**, 63-75, 1971.

[34] Donohoe K. G., Wydeven T., *J. Appl. Polymer Sci.*, **23**, 2591-601, 1979.

[35] Massines F., Mayoux C., Messaoudi R., Rabehi A., Segur P., *Proc. 10th Int. Conf. on Gas Discharges and Their Applications*, **GD-92**, 730- 3, 1992.

[36] Massines F., Rabehi A., Decomps P., Gadri R. B., Segur P., Mayoux C., *J. Appl. Phys.*, **83**, 2950-7, 1998.

[37] Nikonov V., Bartnikas R., Wertheimer M. R. J., *Phys. D: Appl. Phys.*, **34**, 2979-86, 2001.

[38] Radu I., Bartnikas R., Wertheimer M. R., *J. Phys. D: Appl. Phys.*, **36**, 1284-91, 2003.

[39] Radu I., Bartnikas R., Czeremuszkin G., Wertheimer M. R., *IEEE Trans. Plasma Sci.* , **31**, 411-21, 2003.

[40] Salge J. J., *de Phys. IV* , **5**, C5 583-592, 1995.

[41] Kozlov K. V., Wagner H. E., Brandenburg R., Michel P., *J. Phys. D: Appl. Phys.*, **34**, 3164-76, 2001.

[42] Tepper J., Li P., Lindmayer M., *Proc. 14th Int. Conf on Gas Discharges and their Applications*, **1**, 175-8, 2002.

[43] Brandenburg R., Kozlov K. V., Morozov A. M., Wagner H. E., Michel P., *Proc. in 26th Int. Conf. on Phenomena in Ionized Gases (XXVI2003 ICPIG)*, 2003.

[44] Foest R., Adler F., Sigeneger F., Schmidt M., *Surf. Coat. Technol.*, **163-164**, 323-30, 2003.

[45] Akishev Yu. S., Dem'yanov A. V., Karal'nik V. B., Pan'kin M. V., Trushkin N. I., *Plasma Phys. Rep.*, **27**, 164-171, 2001.

[46] Golubovskii Yu. B., Maiorov V. A., Behnke J., Behnke J. F., J. *Phys. D: Appl. Phys.*, **35**, 751-61, 2002.

[47] Golubovskii Yu. B., Maiorov V. A., Behnke J., Behnke J. F., *J. Phys. D: Appl. Phys.*, **36**, 39-49, 2003.

[48] Golubovskii Yu. B., Maiorov V. A., Behnke J., Behnke J. F., *J. Phys. D: Appl. Phys.*, **36**, 975-81, 2003.

[49] Trunec D., Brablec A., St'astny F., Bucha J., *Contrib. Plasma Phys.*, **38**, 435-45, 1998.

[50] Trunec D., Brablec A., Buchta J., *J. Phys. D: Appl. Phys.*, **324**, 1697-9, 2001.

[51] Kogelschatz U., IEEE Trans. Plasma Sci., **30**, 1400-8, 2002.

[52] Kogelschatz U., *Contrib. Plasma Phys.*, **47**, 1-2, pp80-88, 2007.

[53] Tanaka M., Yagi S., Tabata N., *Trans. IEEE of Japan*, **98A**, 57-62, 1978.

[54] Hirth M., *Beitr. Plasmaphys.*, **21**, 1-27, 1981.

[55] Eliasson B., Hirth M., Kogelchatz U., *J. Phys. D: Applied Phys.*, **20**, 1421-37, 1987.

[56] Braun D., Kuchler U., Pietsch G., *J. Phys. D: Appl. Phys.*, **24**, 564-72, 1991.

[57] Drimal J., Gibalov V. I., Samoilovich V. G., *Czech. J. Phys. B*, **37**, 1248-55, 1987.

[58] Drimal J., Kozlov K. V., Gibalov V. I., Samoylovich V. G., *Czech. J. Phys. B*, **38**, 159- 65, 1988.

[59] Gibalov V. I., Drimal J., Wronski M., Samoilovich V. G., *Contrib. Plasma Phys.*, **31**, 89-99, 1991.

[60] Coogan J. J., Sappey A. D., *IEEE Trans. Plasma Sci.*, **24**, 91-2, 1996.

[61] Falkenstein Z., *J. Appl. Phys.*, **81**, 5975-9, 1997.

[62] Wendt R., Lange H., *J. Phys. D: Appl. Phys.*, **31**, 3368-72, 1998.

[63] Kozlov K. V., Wagner H. E., Brandenburg R., Michel P., *J. Phys. D: Appl. Phys.*, **34**, 3164-76, 2001.

[64] Fridman A., Chirkov A., Gustol A., *J. Phys. D: Appl. Phys.*, **38**, 1-24, 2005

[65] Alexeff I., Laroussi M., Kang W., Alikafesh A., *Proc. IEEE Int. Conf. Plasma Sci.,* 208, 1999.

[66] Okazaki S., Kogoma M., Uehara M., Kimura Y., *J. Phys. D: Appl. Phys.,* **26**, 889-892, 1993.

[67] Yokoyama T., Kogoma M., Moriwaki T., Okazaki S., *J. Phys. D: Appl. Phys.,* **23**, 1125-1128, 1990.

[68] Gherardi N., Gouda G., Gat E., Ricard A., Massines A., *Plasma Sources Sci. Technol.*, **9**, 340-346, 2000.

[69] Roth J. R., Laroussi M., Liu C., *Proc. 27th IEEE ICOPS*, 21, 1992.

[70] Kanazawa S., Kogoma M., Moriwaki T., Okazaki S., *J. Phys. D: Appl. Phys.,* **21**, 838-840, 1988.

[71] Roth J. R., *Industrial Plasma Engineering,* **1**, 453-463, 1995.

[72] Laroussi M., *Plasma Processes and Polymers*, **2**, 5, 391-400, 2005.

[73] Behnke J. F., Steffen H., Lange H., *Proc. 5th Int. Symp. on High Pressure Low Temperature Plasma Chemistry (HAKONE V)*, 133-137, 1996.

[74] Massines F., Gherardi N., Sommer F., *Plasmas and Polymers*, **5**, 151-172, 2000.

[75] Sonnenfeld A., Tun T. M., Zajickova M., Kozlov K. V., Wagner H. E., Behnke J. F., Hippler R., *Plasmas and Polymers*, **6**, 237, 2001.

[76] Behnke J.F., Steffen H., Sonnenfeld A., Foest R., Lebedev V., Hippler R., proc in *Hakone VIII*, 410-415, 2002.

[77] Gage R. M., *Arc Torch and Process*, United States Patent No., **US2858411**, 1961.

[78] Koretzky E., Kuo S. P., *Phys. Plasmas*, **5**, 10, 3774-3780, 1998.

[79] Boulos M., Fauhais P., Pfender E., *Thermal Plasmas Fundamentals and Applications*, **1**, 33-47 and 403-418, 1994.

[80] Zhukov M., *Thermal Plasma and New Material Technology*, **1**, 9-43, 1994.

[81] Massines F., Gadri R.B., Decomps P. , Rabehi A., Segur P., Mayoux C., *XXII. International Conference on Phenomena in Ionised Gases*, 306-315, 1995.

[82] Klages C.P., Hopfner K., Klake N., Thyen R., *Proc. in International Symposium on High Pressure Low Temperature Plasma Chemistry (Hakone VII)*, 429433, 2000.

[83] Barankova H., Bardos L., *Appl. Phys. Lett.*, **76**, 285-287, 2000.

[84] Park J., Henins I., Herrmann H.W., Selwyn G.S., *Appl. Phys.Lett.*, **76**, 288-290, 2000.

[85] Novak M., Sicha M., Kapicka V., Jastrabik L., Soukup L., Hubicka Z., et al., *J. Phys. IV France*, **7**, C4-331, 1997.

[86] Babayan S. E., Jeong J. Y., Tu V. J., Park J., Selwyn G. S., Hicks R., *Plasma Sources Sci. Technol.*, **7**, 286-288, 1998.

[87] Kapicka V., Klima M., Vaculik R., Brablec A., Slavicek P., Strecha M., Sicha M., *Czech.J. Phys.*, **49**, 1161-6, 1998.

[88] Kapicka V., Sicha M., Klima M., Hubicka Z., Tous J., Brablec A., Slavicek P., Behnke J. F., Tichy M., Vaculik R., *Plasma Sources Sci. Technol.*, **8**, 15-21, 1999.

[89] Breblec A., Kapicka V., Ondracek Z., Slavicek P., Strecha M., Sicha M., Stastny F., Vaculik R., *Czech. J. Phys.*, **49**, 329 - 34, 1999.

[90] Hubicka Z., Cada M., Sicha M., Churpita O., Pokorny P., Soukup L., Jastrabik L., *Plasma Sources Sci. Technol.*, **11**, 195-202, 2002.

[91] Klima M., Slavicek P., Zajickova L., Janca J., Kuzmin S., Sulovsky P., *Czechoslovak Journal of Physics*, **49**, 3, 1999.

[92] Churpita O., Hubicka Z., Cada M., Chvostova D., Soukup L., Jastrabyk L., Ptacek P., *Surface and Coatings Technology*, **174-175**, 1059-1063, 2003.

[93] Hippler R., Pfau S., Schmidt M., Schoenbach K. H., *Low Temperature Plasma Physics, Fundamental Aspects and Applications*, Berlin, 2001.

[94] Johnson E. O., Malter L., *Phys. Rev.*, **80**, 58, 1950.

[95] Sicha M., Tichy M., Hrachova V., David P., David T., Tous J., *Contrib. Plasma Phys.*, **34**, 51, 1994.

[96] Donohoe K. G., *PhD Thesis*, California Institute of Technology, Pasadena, CA, 1976.

[97] Cada M., Hubicka Z., Sicha M., Churpita O., Jastrabik L., Soukup L., Tichy M., *Surface and Coatings Technology*, **174-175**, 530-534, 2003.

[98] http://csep10.phys.utk.edu/astr162/lect/light/absorption.html

[99] Fantz U., *Plasma Sources Sci. Technol.*, **15**, S137-147, 2006.

[100] Chen F. F., Chang J. P., *Lecture Notes on Principles of Plasma Processing*, 2003

[101] Hippler R., Pfau S., Schmidt M., Schoenbach K. H., *Low Temperature Plasma Physics*, 2001.

[102] Buuron A. J. M., Otorbaev D. K., van de Sanden M. C. M., Schram D. C., *Rev. Sci. Instrum.*, **66**, 968-74, 1994.

[103] Booth J. P., Cunge G., Neuilly F., Sadeghi N., *Plasma Sources Sci. Technol.*, **7**, 423-30, 1998.

[104] http://hyperphysics.phy-astr.gsu.edu/hbase/atomic/stark.html

[105] Jasinski M., Czylkowski D., Zakrzewski Z., *Proc. XXVIIth ICPIG, Eindhoven, The Netherlands*, 18-25, 2005.

[106] Torres J., Jonkers J., van de Sanden M. J, van der Mullen J. J. A. M., Gamero A., Sola A., *J. Phys. D: Appl. Phys.*, **36**, L55-L59, 2003.

[107] Griem H. R., Kolb A. C., Shen K. Y., *Astrophys. J.*, **135**, 272, 1962.

[108] Griem H. R., *Spectral Line Broadening by Plasmas*, Academic Press New York, 316, 1974.

[109] Goktas H., Demir A., Hajiyev E., Turan R., Seyhan A., Oke G., *Int. Conf. Plasma*, 81, 2003.

[110] Gigosos M. A., Cardenoso V., *J. Phys. B: At. Mol. Opt. Phys.*, **29**, 4795-4838, 1996.

[111] Aglient Technologies, *The impedance measurement handbook. A guide to measurement technology and techniques*, 2002-2003.

[112] http://www.valdosta.edu/ tmanning/hon399/marios.htm

[113] www.azom.com/details.asp?ArticleID=1179

[114] http://www.reade.com/Products/Minerals-and-Ores/Rutile-powder-(TiO2).html

[115] www.specialchem4polymers.com/tc/Titanium-Dioxide/index.aspx?id=benefits-opacity

[116] Farrell K. A., *A Thesis for Degree of Master of Science*, Synthesis Effect on Grain Size and Phase Content in Anatase - Rutile TiO_2 system, 2001.

[117] http://www.ilo.org/public/english/protection/safework/cis/products/icsc/dtasht/_icsc03/icsc0338.htm

[118] Madelung O., Rosser U., Schulz M., Non-tetrahedrally bonded binary compounds II, **41D**, 1-7, 2000.

[119] http://www.reade.com/Products/Minerals-and-Ores/Anatase-powder-(TiO2).html

[120] Navrotsky A., Kleppa O. J., *J. Am. Ceram. Soc.*, **50**, 626, 1967.

[121] McColm I. J., *Ceramic Science for Materials Technologists*, 1983.

[122] Ahonen P., *A Thesis for Degree of Doctor of Science in Technologies*, Aerosol Production and Crystallization of Titanium Dioxide From Metal Alkoxide Droplets, 2001.

[123] Stall D. R., "JANAF Thermochemical Tables", *Joint Army-Navy-Air Force-ARPA-NASA Thermochemical Working Group*, 1996.

[124] www.azom.com/details.asp?ArticleID=2357

[125] http://en.wikipedia.org/wiki/Zinc_oxide

[126] http://www.akrochem.com/pdfs/Zinc/x-zno%20fpt-z.pdf

[127] Hong N. H., Sakai J., Brize V., *J. Phys.: Condens. Matter*, **19**, 036219, 2007.

[128] http://navbharat.co.in/clients.html

[129] Binning G., Quate C. F., Gerber Ch., *Phys. Rev. Letters*, **56**, 930-933, 1986.

[130] http://vpd.ms.northwestern.edu/teaching/AFM_MSc_190_lab.pdf

[131] http://en.wikipedia.org/wiki/X-ray_crystallography

[132] http://hyperphysics.phy-astr.gsu.edu/hbase/quantum/bragg.html

[133] Van der Pauw L. J., A method for measuring specific resistivity and Hall effect of discs of arbitrary shape, *Philips Res. Repts.*, **13**, 1-9, 1958.

[134] Brož J. et al., *Základy fyzikálních měření (Basics of the physical measurements)*, **II (B)**, 1974.

[135] Soukup L., Hubička Z., Churpita O., Čada M., Pokorný P., Zemek J.,Jurek K., Jastrabík L., *Surface and Coatings Technology*, **169-170** , 571-574, 2003.

[136] Sicha M., Hubicka Z., Soukup L., Jastrabik L., Cada M., Spatenka P., *Surface and Coatings Technology*, **148**, 199 -205, 2001.

[137] Šicha M., Hubička Z., Tichý M., Novák M., Soukup L., Jastrabík L., Behnke J. F., *Contrib. Plasma Phys.*, **36**, 605, 1996.

[138] Shi J. J., Deng X. T., Hall R., Punnett J. D., Kong M. G., *J. Appl. Phys.*, **94**, 6303, 2003.

[139] Butterbaugh J. W., Baston L. D., Sawin H. H., *J. Vac. Sci. Tech. A.*, **8**, 916, 1990.

[140] Kousal J., et al., *Czechoslovak Journal of Physics*, **52**, D571, 2002.

[141] Hubička Z., *PhD Thesis*, Charles University in Prague, 1998.

[142] Danylewych L., Nicholls R., *Proc. R. Soc. Lond.*, **360**, 557-573, 1978.

[143] Condon E. U., *Phys. Rev.*, **28**, 1182, 1926.

[144] Huber K. P., Herzberg G., *Constants of Diatomic Molecules*, 1979

[145] Tyte P. C., Jnnanen S. H., Nicholls R. W., *Identification Atlas of Molecular Spectra*, **5**, 1967.

[146] Danylewych L., Nicholls R., *Proc. R. Soc. Lond.*, **A 339**, 197-212, 1974.

[147] Gaydon A. G., *Dissociation Energies and Spectra of Diatomic Molucules*, 1953.

[148] Johnson R. C., Tawde N. R., *Proc. R. Soc. Lond. A*, **137**, 575-591, 1932.

[149] Richter N. B., *The Nature of Comets*, 1965.

[150] Swings P., Molecular Spectra in Cosmic Sources, *Astrophysics symposium*, 145-171, 1951.

[151] McCallum J. C., Nichols R. W., Jarmain W. R., Centra for Research in Experimental Space Science Spectroscopic Report N1, York University, 1978.

[152] Burns A., Hayes G. , Li W., Hirvonen J., Demaree JD., Shah SI.,*Materials Science and Engineering B*, **111 (2-3)**, 150-155, 2004.

[153] Tsyganov I., Maitz M. F., Wieser E., Prokert F., Richter E., Rogozin A., *Surface and Coatings Technology*, 174 -175, 591-596, 2003.

[154] Dai Z., Naramoto H., Narumi K., Yamaoto S., *J. Phys.: Condens. Matter*, **11**, 8511-8516, 1999.